

Modeling and Shaped Based Inversion for Frequency
Domain Ultrasonic Monitoring of Cancer Treatment

A Thesis Presented

by

Başak Ülker Karbeyaz

to

The Department of Electrical and Computer Engineering

in partial fulfillment of the requirements

for the degree of

Doctor of Philosophy

in

Electrical Engineering

in the field of

Fields, Waves and Optics

Northeastern University

Boston, Massachusetts

September 2005

© Copyright by Başak Ülker Karbeyaz

All Rights Reserved

NORTHEASTERN UNIVERSITY

Graduate School of Engineering

Thesis Title: Modeling and Shaped Based Inversion for Frequency Domain Ultrasonic Monitoring of Cancer Treatment.

Author: Başak Ülker Karbeyaz.

Department: Electrical and Computer Engineering.

Approved for Thesis Requirements of the Doctor of Philosophy Degree

Thesis Advisor: Prof. Eric L. Miller

Date

Thesis Reader: Prof. Robin Cleveland

Date

Thesis Reader: Prof. Ronald A. Roy

Date

Thesis Reader: Louis Poulo

Date

Department Chair: Prof. Stephen McKnight

Date

Director of the Graduate School

Date

NORTHEASTERN UNIVERSITY

Graduate School of Engineering

Thesis Title: Modeling and Shaped Based Inversion for Frequency Domain Ultrasonic Monitoring of Cancer Treatment.

Author: Başak Ülker Karbeyaz.

Department: Electrical and Computer Engineering.

Approved for Thesis Requirements of the Doctor of Philosophy Degree

Thesis Advisor: Prof. Eric L. Miller	Date
Thesis Reader: Prof. Robin Cleveland	Date
Thesis Reader: Prof. Ronald A. Roy	Date
Thesis Reader: Louis Poulo	Date
Department Chair: Prof. Stephen McKnight	Date
Director of the Graduate School	Date
Copy Deposited in Library:	
Reference Librarian	Date

Abstract

High Intensity Focused Ultrasound (HIFU) is a cancer treatment technique where high frequency sound waves (ultrasound) are used to necrose the cancerous tissue. An important open issue is monitoring the progress of the treatment by non-invasive imaging techniques. In this work, we propose the use of ultrasound-based imaging techniques to characterize the geometric structure of the HIFU lesion.

The computational size of the relevant 3D ultrasound problem renders impractical the use of nonlinear methods. Thus we relied on a linearized model, the well-known first Born approximation, as the basis for determining both the perturbations in the three acoustic parameters and the background properties around which the linearization was performed. We demonstrated a novel method for rapidly constructing the Born kernels for commercial-type transducer based on a new semi-analytic expression for the impulse response of the cylindrical and spherical transducers. We introduced a fast semi-analytical method based on Stepanishen's formulation (J.Acoust.Soc.Am, V.49, 1971B, 1627-1638) to compute the acoustic field of these transducers in any physically realizable lossy homogeneous medium. We demonstrated over two orders of magnitude speedup compared to an optimized numerical routine and validated the accuracy of our method with laboratory measurements with a tissue phantom.

To obtain quantitatively accurate reconstructions of the HIFU anomaly, one could invert for the acoustic properties on a densely sampled grid of voxels. However, the computational size of the problem makes traditional pixel based

inversion methods impractical. Hence, we exploited the fact that the treatment results in ellipsoidal lesions in which sound speed and attenuation are altered from their nominal values. We discussed shape-based methods under which we need to estimate a small number of parameters to describe the geometry of the lesion. The details of this nonlinear inversion method are provided and its performance and robustness are demonstrated using both simulated and measured broadband ultrasound backscatter data. Results are provided from data collected using a commercial ultrasonic scanner, AN2300 of Analogic Corporation, Peabody, MA, and a tissue phantom containing a HIFU-like lesion. [This work is supported in part by CenSSIS (NSF Award No. EEC-9986821) and NSF Award No. 0208548.]

Acknowledgements

I am first and deeply grateful to my advisor, Prof. Eric L. Miller, for his guidance and support over the period we have worked together. His ideas and enthusiasm were the most valuable contributions to my thesis. I would also like to thank to my co-advisor Prof. Robin Cleveland from Boston University who helped me to fill the gaps in my ultrasound background. Without Prof. Cleveland's help and collaboration, the experimental part of this thesis would be incomplete. I want to express my gratitude to Prof. Yaman Yener for giving me the courage and opportunity to come to United States for my PhD study. I would like to acknowledge the financial support through CenSSIS under the Engineering Research Centers Program of the National Science Foundation. I also would like to thank to Prof. Philip Serafim for his excellent teaching that helped me to make peace with electromagnetic theory. I am grateful for technical assistance provided by Dr. Yuan Jing, Dr. Emmanuel Bossy and Dr. Charles Thomas in setting up the experiments. I also want to thank to my parents, who taught me the value of hard-work, for their endless love and support. My gratitude turns to my sister for her precious support and love. Finally, I will be always grateful to my husband who has endlessly supported me over all these years for his patience, love and ideas. His contribution to this dissertation is invaluable. This thesis is dedicated to him.

Contents

1	Introduction	1
1.1	Outline of the Thesis	15
2	Propagation of Ultrasound in Time Domain	16
2.1	Theory and Background	17
2.1.1	Jensen's Formulation	18
2.1.2	Calibration Process: Obtaining the v_{pe} signal	21
2.2	Scattering from a flat-plate	22
2.3	Scattering from a point target	25
2.4	Scattering from arbitrary shaped weak scatterers: Born Approx- imation	28
2.5	Experiments	29
2.6	Conclusion	33
3	Propagation of Ultrasound in the Frequency Domain	37
3.1	Derivation of the Scattered Field	38
3.1.1	Acoustic Wave Equation	39
3.1.2	A Model for k^2	40

3.1.3	Born Approximation	45
3.2	Derivation of the Incident Field	47
3.3	Derivation of the Received Signal	48
3.4	Derivation of the Spatial Transfer Function	50
3.4.1	On-axis case	51
3.4.2	Off-axis case	53
3.5	Wave Propagation Experiment	56
3.6	Conclusion	62
4	Cylindrically Concave Transducers	64
4.1	Theory: Spatial Impulse Response	65
4.2	Spatial Transfer Function for the Cylindrical Geometry	66
4.3	Integral Calculation	73
4.3.1	Case 1: Regions I and II $0 \leq \phi_{\mathbf{p}} \leq \phi_{\mathbf{t}}$	76
4.3.2	Case 2: Region III, $\phi_{\mathbf{t}} < \phi_{\mathbf{p}} \leq \pi - \phi_{\mathbf{t}}$	82
4.3.3	Case 3: Regions IV and V $(\pi - \phi_{\mathbf{t}}) \leq \phi_{\mathbf{p}} \leq \pi$	84
4.3.4	Case 4: On the z axis $r_p = 0$	89
4.3.5	Polynomial Approximation	89
4.4	Results	92
4.4.1	Numerical Integration	92
4.4.2	Experimental Comparison	93
4.4.3	Numerical Comparison	99
4.5	Conclusion	102
5	Shape Based Inversion	104
5.1	Mathematical Description and Background	105

5.1.1	Forward Model	105
5.1.2	Ellipsoid Modeling	108
5.1.3	Final Problem Statement	113
5.2	Inversion Approach	115
5.3	Inversion Examples and Results	117
5.3.1	Numerical Experiments and Results	118
5.3.2	Error Analysis	125
5.3.3	Laboratory Experiment and Results	127
5.3.4	Simulation Grid and the Choice of Region of Interest . .	134
5.3.5	Results	138
5.4	Conclusion	143
6	Conclusion and Future Work	146
6.1	Objectives and Specific Aims	146
6.2	Overview and Significance	147
6.3	Preliminary Studies: A shape-based approach to the tomographic Ultrasonic imaging problem	148
6.4	Future work: Design and Methods	150
A	Acoustic Field of the Cylindrically Concave Transducers	153
A.1	Case 1: Regions I and II $0 \leq \phi_{\mathbf{p}} \leq \phi_{\mathbf{t}}$	154
A.1.1	Region I: $\phi_{\mathbf{max}} < \tan\phi_{\mathbf{p}} \leq \phi_{\mathbf{t}}$	154
A.1.2	Region II: $\tan\phi_{\mathbf{p}} \leq \phi_{\mathbf{max}}$	155
A.2	Case 2: Region III, $\phi_{\mathbf{t}} < \phi_{\mathbf{p}} \leq \pi - \phi_{\mathbf{t}}$	156
A.3	Case 3: Regions IV and V $\pi - \phi_{\mathbf{t}} \leq \phi_{\mathbf{p}} \leq \pi$	157
A.3.1	Region IV: $\tan\phi_{\mathbf{p}} < \phi_{\mathbf{min}}$	157

A.3.2	Region V: $\tan\phi_{\mathbf{p}} \geq \phi_{\mathbf{min}}$	158
-------	--	-----

List of Tables

3.1	Nominal acoustic properties of the Agar Phantom	61
5.1	Lower and upper limits for the geometric parameters of the ellipsoid	120
5.2	Contrast and error values for the sound speed, attenuation and density	121
5.3	Lower and upper limits for the geometric parameters of the ellipsoid	142
5.4	Contrast and error values for the sound speed and attenuation .	143

List of Figures

1.1	Simplified block diagram of the signal flow. This figure is taken from the Users' Guide for Analogic AN2300 Ultrasound Engine, with the permission of Louis Poulo.	3
1.2	The HIFU lesion formed at 1.1 MHz in a polyacrylamide gel based phantom.	7
2.1	Schematic showing the transducer/scatterer arrangement.	19
2.2	(a) Reference pulse-echo from a large thick acrylic plate placed in the geometric focal plane of a 3.5 MHz spherically focused transducer. (b) Amplitude spectrum of pulse-echo.	31
2.3	Comparison of the flat-plate pulse-echo (Fig. (2.2)(a), normalized and filtered), differentiated flat-plate pulse-echo (Fig. (2.2)(a), normalized and doubly differentiated with respect to time) and a pulse-echo from the tip of an optical fiber placed at the geometric spherical focal point of a 3.5 MHz transducer.	32

2.4	(a) Amplitude envelope of the pulse-echo field of 3.5 MHz transducer as measured by scanning an optical probe laterally at an axial distance equal to the focal length. (b) Amplitude envelope of the simulated pulse-echo field using Eq. (10c) and differentiated signal from Fig. (2.3).	34
2.5	(a) Amplitude envelope of the pulse-echo field of 3.5 MHz transducer as measured by scanning an optical probe laterally at an axial distance $z=53.8$ mm. (b) Amplitude envelope of the simulated pulse-echo field using Eq. (10c) and differentiated signal from Fig. (2.3)	35
3.1	Transmitter, receiver, and the scatterer location vectors.	49
3.2	Geometry of the problem.(On-axis case)	52
3.3	Geometry of the problem.(Off-axis case)	53
3.4	Data acquisition system and the water tank in Boston University.	57
3.5	Experimental setup with the transducers and the phantom.	58
3.6	Predicted and measured waveforms after propagating through a tissue mimicking phantom	59
3.7	Beam plots of the predicted and measured waveforms.	60
4.1	The geometry of the transducer and the coordinate system.	67
4.2	(a) The oscillations of the real part of the kernel in Eq.(4.5) at 5 MHz for $P(0,10 \text{ mm},0)$ (b) The oscillations of the real part of the kernel in Eq.(4.5) at 5 MHz for $P(59 \text{ mm},8 \text{ mm},0)$	69
4.3	Schematic showing the segmentation for ϕ_p	70
4.4	The limit functions with monotonic decreasing ϕ dependency.	77

4.5	The limiting functions with monotonic increasing ϕ dependency.	82
4.6	(a)Amplitude envelope of the simulated acoustic field on y axis using the equations derived in Section 4.3 (b)Amplitude envelope of the simulated acoustic field on y axis using Eq.(4.55) (c) Amplitude envelope of the measured ultrasound field of a 3.5 MHz transducer.	96
4.7	(a)Amplitude envelope of the simulated acoustic field on z axis using the equations derived in Section 4.3 (b)Amplitude envelope of the simulated acoustic field on z axis using Eq.(4.55) (c) Amplitude envelope of the measured ultrasound field of a 3.5 MHz transducer.	97
4.8	(a)Amplitude envelope of the simulated acoustic field on the $x - z$ plane using the equations derived in Section 4.3 (b)Amplitude envelope of the simulated acoustic field on the $x - z$ plane using Eq.(4.55) (c) Amplitude envelope of the measured ultrasound field of a 3.5 MHz transducer.	98
4.9	(a)Amplitude envelope of the simulated acoustic field on the $x - y$ plane using the equations derived in Section 4.3 (b)Amplitude envelope of the simulated acoustic field on the $x - y$ plane using Eq.(4.55) (c) Amplitude envelope of the measured ultrasound field of a 3.5 MHz transducer.	100
4.10	(a)Amplitude envelope of the simulated acoustic field on the $x - y$ plane for lossy medium using the equations derived in Section 4.3 (b)Amplitude envelope of the simulated acoustic field for lossy medium on the $x - y$ plane using Eq.(4.55)	101

5.1	Decision function $A(x)$ and its derivative	111
5.2	The expected shapes are drawn with black lines on top of the approximated ellipsoids. The contrasts of the ellipsoids are shown with the color scales. As predicted from Fig. (5.1) the contrast values gradually decay to zero.	114
5.3	Experimental Setup	118
5.4	Case 1: Inversion for similarly sized and shaped ellipsoids. . . .	122
5.5	Case 2: Inversion for concentric and overlapping ellipsoids. . . .	123
5.6	Case 3: Inversion for significantly different ellipsoids.	124
5.7	Common initial value for the simulations	126
5.8	Distribution of volumetric and contrast errors	127
5.9	Linear array transducer	128
5.10	Schematic of the locations of the transducers on the transducer array	129
5.11	Laboratory Experiment Settings	130
5.12	The real and the enhanced images of the BSA phantom.	132
5.13	A sample image of the BSA phantom with Analogic Engine ultrasound scanner (B-mode pre-scan converted).	133
5.14	The data corresponding to the envelope of the signal from the 64 th line of the image.	133
5.15	Region of Interest in 3D	136
5.16	Region of Interest in 2D	137
5.17	Initial true ellipsoid distribution from different view angles . . .	139
5.18	True ellipsoid distribution from different view angles	140
5.19	Experimental inversion result	141

Introduction

Ultrasound imaging, also known as ultrasound scanning or sonography, is a widespread noninvasive imaging modality using high frequency sound waves. It is a low-cost real time diagnostic tool to monitor the abnormalities in the soft tissues of the human body. With the proper setup of the ultrasound scanner, the cross-sectional images of the internal organs, such as heart, liver, pancreas, kidneys, and bladder can be obtained. In the medical area sonography is successfully used for diagnostic and therapeutic applications such as: assessment of fetus health, non-invasive detection and disintegration of kidney stones, and diagnosis of osteoporosis.

The major advantage of ultrasound compared to the other imaging techniques is the real-time imaging capability. It can show movement of internal tissues and organs and, combined with the image processing tools, enables physicians to monitor the blood flow in the body [1]. However compared to the other tomographic techniques such as X-ray Computed Tomography and Magnetic Resonance Imaging, ultrasound images have poor spatial resolution [1, 2]. Images are qualitative, do not give information about the physical nature of the targets and are distorted by spatially varying transducer field. An increasing

number of researchers are working to develop new ultrasound imaging techniques and transducer types to overcome this problem [1, 3–6].

Conventional diagnostic ultrasound scanners operate in pulse-echo mode which is similar to the operation of a radar. The imaging process is initiated when the ultrasound transducer, a piezoelectric element, is excited with a voltage spike. The transducer then emits a pressure wave in the form of longitudinal mechanical vibration [7].

The acoustic wave propagating in the tissue gets reflected at the interfaces between different acoustic impedances. Some of the reflected wave (echo) returns to the transducer and is converted to an electrical signal.

The range of the echo signal is determined by the elapsed time, dt , from the transducer emission to the arrival of the echo by assuming an average velocity of sound in tissue:

$$\text{Range} = V_{\text{tissue}} \frac{dt}{2} \quad (1.1)$$

where ($V_{\text{tissue}} = 1540\text{m/s}$) [7].

The strength of the pulse-echo mainly depends on two parameters: The characteristic acoustic impedance across the interface, which is the product of the mass density of the medium and the velocity of the ultrasound in that medium, and the angle of incidence of the pressure wave at the tissue interface [7, 8].

The strength of the received echoes are usually displayed as increased brightness in the display screen which is the B-mode (B for Brightness). The highly reflecting bone surfaces would appear bright, and fluids that contain no scatterers are dark.

Instrumentation for B-mode Imaging: The transmit and the receive

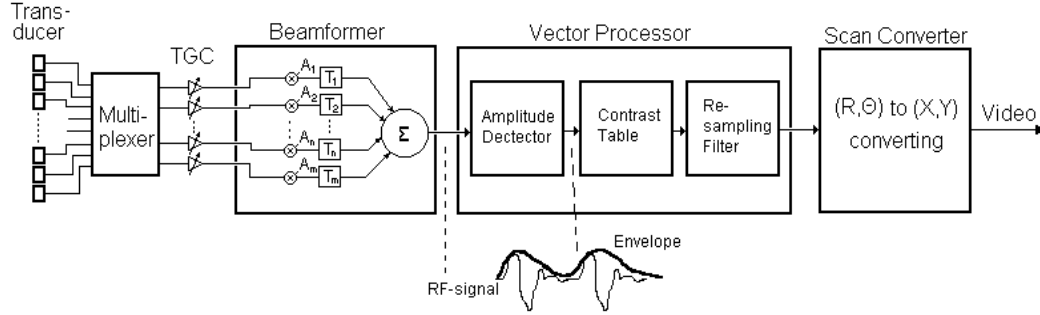


Figure 1.1: Simplified block diagram of the signal flow. This figure is taken from the Users' Guide for Analogic AN2300 Ultrasound Engine, with the permission of Louis Poulo.

process used to create the ultrasound beam is described as beamformation. Figure 1.1 shows the block diagram of the beamformation steps required for B-mode imaging. The actual implementations vary among manufacturers and the figure shows the implementation for AN2300 of Analogic Corporation [9].

The beamforming stage for AN2300 can be described with five modules: On the left side, there is a transducer with up to 192 elements connected to a multiplexer which connects 64 elements to the Time Gain Compensation (TGC) state. Next the TGC signal is fed into the digital beamformer which sums the 64 channel into a single RF beam. The vector processor converts the RF-signal to an intensity signal and as the last stage, the scan converter converts the single scanlines (beams) into a X/Y pixel based picture [9]. The details of these blocks for a general ultrasound imaging system are described below:

TGC stage: The dynamic range of the echoes vary as much as 50dB due to the acoustic impedance mismatch across tissue interfaces and the signal attenuation within the tissue. To avoid losing information it is necessary to be able to display such a range of signal amplitudes. TGC stage supply the gain required

to compensate for these losses caused by the propagation of ultrasound in the tissue [8].

Beamformer stage: The transmitted and received signals passing from the array elements can be individually delayed in time. This step is implemented electronically to steer and focus each of the sequence of acoustic pulses through the plane or volume to be imaged.

The Huygens principle states that a wavefront can be decomposed into a number of point sources, each being the center of an expanding spherical wave [10]. In other words, any wavefront can be constructed from point sources. This is the principle used to focus and steer the ultrasound beam to the desired location in space. The signals that are sent to and received from the elements of the aperture can be given individual time-delays to create the desired wavefront.

The beam steering can be achieved by either element selection or using a phased array. Element selection is a low cost beam steering approach which involves steering of the beam by selecting the center element. In this approach one does not really change the orientation of the beam but rather change the location of the origin. The beam will shift to a new location as the center of the active element group is shifted to a new location. The beam steering can be also be achieved by phased arrays using the appropriate time delays.

Vector Processing: After the beamformer stage, the received signals are passed through several signal processing stages. The output of the beamformer stage is a wide band RF signal. The signal is usually filtered to clean the out-of-band noise contributions. A wide band image processing algorithm can also be employed to reduce the impact of speckles. An envelope detection is implemented in this stage to obtain the amplitude information [8].

Scan Converter: The image data is obtained on a polar coordinate grid for commercial scanners and it is necessary to convert this image to one of the standard TV image formats for easier viewing and recording. This stage is known as the Scan Converter. The major function of the Scan conversion is interpolation from a polar grid to a video pixel region.

As a summary, a typical ultrasound system uses a transducer made up of a number of piezoelectric elements to transmit a sound pulse into the tissue. Normally the same transducer is used to receive the reflected sound from the scatterers within the body. This process is done in a sequential manner, steering the emitted sound beam in turns along the lines in the region to be imaged.

The use of ultrasound for diagnostic purposes requires a strict limit to be set on the applied power density (about 0.1 Watt/cm^2) [11]. When used with a higher intensity, a focused ultrasound beam can damage the tissue and create lesions. Today, this destructive phenomenon is successfully used as a cancer treatment technique known as High Intensity Focused Ultrasound (HIFU) therapy [12].

High Intensity Focused Ultrasound: The observations on the destructive ability of the high intensity ultrasound date back to the time of Paul Langevin. During his tests with quartz plate transducers, he observed the death of small fish which exposed to the beam of ultrasound. He also reported the pain felt in one's hand when immersed in a water tank insonated by high intensity ultrasound [13].

The idea of using ultrasound for therapeutic purposes is not new. The earliest therapeutic ultrasound experiment on biological tissues was performed by Lynn and Putnam (1942) where they necrosed brain tissue in animals using ultrasound waves. This experiment was carried out even before the use of ultrasound as a

diagnostic tool. However, due to the lack of efficient imaging techniques to guide the therapy, it was not until 1960's that it found a place in medical treatment world.

Today, there is an intensive research activity in HIFU field to understand the physics behind the tissue necrosis and lesion formation. Currently, the most understood mechanisms are the sharp temperature increase linked to the absorption of ultrasound waves and cavitation, which is the formation of collapsing bubbles.

HIFU uses focused ultrasound waves to raise the temperature of the target tissue to approximately 60 degrees Celsius in two to three seconds, creating an ellipsoidal lesion of order 0.2 to 2000mm³ in volume [12, 14]. The dimensions depend on the operating frequency, geometry and exposure time of the HIFU transducer. As an example ter Haar GR et al. reported that, at 1.7 MHz the lesions created in ex vivo beef liver are of ellipsoidal shape, with the long axis parallel to the ultrasound beam with dimensions 1.5 mm to 15 mm [15]. This phenomenon, also called as focused ultrasound surgery (FUS), is depicted in Fig. (1.2). (The figure is obtained from the supplemental video material given in [16].)

There is a significant amount of clinical experience for cancer treatment with HIFU applications. The majority of the clinical trials are the treatment of the prostate cancer and Benign Prostatic Hyperplasia (BHP) [17–22]. HIFU is becoming an accepted therapeutic tool for prostate cancer in Europe, where a long term follow-up data, including over 2000 patients, are reported in 2002 by Chaussy et al. [23, 24]. China is currently leading the HIFU related clinical applications, mainly in the ablation of liver tumors, where China based Chongqing



Figure 1.2: The HIFU lesion formed at 1.1 MHz in a polyacrylamide gel based phantom.

Hifu Co. Ltd's HIFU therapeutic system is utilized [25]. Other promising uses of HIFU are the ablation of the localized breast tumors, and treatment of the kidney, pancreatic and bladder cancers [24]. Between December 1997 to October 2001, 1038 patients with solid tumors had been treated in China [26].

HIFU Lesion Imaging: The basic limitation of HIFU treatment is the difficulty of accurately targeting the region to be treated. In current practice, it is necessary to couple the application with noninvasive monitoring methods to guide the therapy.

The most effective imaging modality to monitor the HIFU lesions is the Magnetic Resonance Imaging (MRI), which can monitor time-dependent temperature elevation [27–29]. However, it requires MRI compatible HIFU equipment and is a relatively high cost procedure.

Being inexpensive and commonly used in prostate imaging, B-scan ultrasound appears to be a good candidate to replace MRI. However, it has been experimentally shown that the lesions does not yield a significant change in the speckle pattern of a standard B-scan gray scale image, while limited information can be extracted using data processing techniques [30]. These techniques are based on signal energy [31], the non-linear properties of the microbubbles in the lesion [32] and non-linear compounding [33].

Recent studies have shown that HIFU applications increase the stiffness of the target area -up to ten times than the healthy tissue- making the lesions detectable by imaging techniques that depict mechanical properties of the tissue [34–36]. However this approach suffers from a possible non-uniqueness in the inversion process [37].

We believe the imaging methods aimed to monitor the changes in the sound speed and attenuation are the most promising modalities to replace MRI. It has been reported that HIFU treatments affect both the sound speed and the attenuation values of the tissue while forming lesions [38–43]. The change in sound speed is less than 20 m/s (about 1%) and peaks at temperatures between 50°-70° and then decreases with the further increase in the temperature. In most cases the change is reported to be reversible. On the other hand the attenuation coefficient significantly increases within the values ranging from 80% to 700% and the change is irreversible [44].

The reversible characteristic of the sound speed makes the methods aimed to monitor only the change in this parameter rather impractical. Recently Pernot et al. [45] presented a very impressive *in vitro* result, where they estimate the changes in the temperature from the sound speed measurements. However, the

lesion will not be visible once the tissue cools down.

The change in the attenuation is irreversible, hence the imaging methods based on capturing the changes in the attenuation are more robust. Since the attenuation in the necrosed tissue is much higher than that of a healthy tissue, the tissue behind the HIFU lesion would appear slightly darker in standard B-scan images. Processing the B-scan data Baker and Bamber [46] and Annad and Kaczkowski [47] detected the changes in the ultrasound images behind the lesion.

Although the common ultrasound wave propagation models depend on the changes in the density of tissue, the link between density and HIFU lesions has not yet been established.

Imaging methods that give the quantitative information about the changes in the all three acoustic properties -attenuation, sound speed and density- should dramatically improve lesion detection.

Inversion Methods: In this dissertation we propose an inversion method to determine the spatial distribution of the sound speed, attenuation and density of the HIFU lesions which uses the standard ultrasound scanners and HIFU transducers.

Processing the data in this manner, reconstructing the acoustic parameters from ultrasound measurements, is known as an inverse problem. Reconstruction problems have a wide range of applications in different disciplines including acoustics. During the last few decades there has been an avalanche of publications on different aspects of the inverse problems. No attempt will be made to present a comprehensive bibliography but the reader is referred to [48–53] for the principal publications in this area.

The motive behind the presented inversion problem is to develop quantitative, fully three dimensional ultrasonic imaging methods to determine the spatial structure of the HIFU lesion. The traditional approach to this problem is to try to reconstruct the voxelated versions of the sound speed, density and absorption images. What complicates this approach is the nominal wavelength of the acoustic fields in tissue (0.3mm) coupled with the physical size of the region of interest of the HIFU lesion (20mm), which implies that up to a one billion voxels might be needed to describe the problem accurately.

Our approach to the problem is based on the specification of the parameters describing the shape of the parameters. We assume the shape of the perturbations are known ellipsoids- but the locations, sizes and orientations are unknown. This method has been addressed in other fields and successfully used in tomographic imaging problems [54–56]. To completely characterize the changes in one acoustic variable, we only need the location of the center, the lengths of the three axes of the ellipsoid, three angles that orient the ellipsoid in space and the contrast of the parameter. Thus rather than the millions of voxels defining each of the three unknown acoustic parameters, we have only $3 \times 10 = 30$ quantities to estimate from the measured data.

Forward Model: Extracting the quantitative information requires the use of a well calibrated physical model directly within the processing algorithms. In this study we examine in detail the acoustic wave behavior in human tissue and present the equations that describe the propagation of ultrasound in a lossy, dispersive medium.

A key to the implementation of the ultrasound propagation models is the

specification of the radiated field generated by the commercially available ultrasound transducers. Ultrasound measurements coupled with a computational physical model of the ultrasonic transducer can be used to determine the spatial maps of the attenuation, sound speed and density. The distribution of these mechanical properties can be used to complement the images formed with traditional ultrasound data acquisition techniques that are based on delay and sum beamforming.

Conventional ultrasound transducers used for medical diagnosis purposes are generally the 1D array type transducers which consist of rectangular apertures placed on either a flat or curved surface. Typically 1D arrays with 32 or more elements that have natural focus in the elevation plane (either by curvature in the element or by use of a lens) are used with electronic focusing along the lateral dimension. Ideally, each element of the array can be excited individually to obtain non-beam formed data. This allows us to collect full tomographic data where single transmitter is used to probe the tissue and the response is measured by the full array or collection of elements of the array. Moreover, this type of tomographic imaging would lead to innovative applications where the array system can be optimized to classify certain targets based on the shape information [57, 58]. To utilize the array transducers for applications beyond traditional beam focusing and steering, it is necessary to have a precise knowledge of the radiated fields generated by the cylindrically curved transducers. Once this field is known, it can be applied to simulate the free diffraction field of the linear arrays.

A number of different methods have been proposed to compute the ultrasonic transient fields. The spatial impulse response (SIR) approach provides

an effective method to predict the sound field of uniformly excited ultrasound transducers. A through literature review of the applications of this method to simulate the pressure fields of the arbitrarily shaped transducers is given in [59].

The impulse response of an ultrasound transducer is defined as the response to a velocity impulse on the radiating surface of the transducer [60–62]. In the time domain the SIR is convolved with the time derivative of the normal particle velocity or the electromechanical response of the transducer to obtain the sound pressure. For frequency domain applications, the simulated field is described by the Fourier Transform of the spatial impulse response, that is the spatial transfer function.

The frequency domain representation of the SIR for ultrasonic transducers is trivial to state and the time domain response can be obtained via inverse Fourier transform. However, the frequency domain representation of the response presents a task that is too computationally demanding to compute in a straightforward manner. For most of the cases the integral operator does not have a closed form solution and has a highly oscillatory kernel. On the other hand, time domain solutions are not sufficient to describe the behavior in tissue like, frequency dependent lossy media. Due to this limitation, in general frequency domain methods are preferred.

A number of powerful *numerical* methods are available to predict the spatial transfer function of the linear arrays for lossless homogenous media. Wu and Stepinski [59] proposed an efficient time domain method to compute the SIR for linear arrays with cylindrically concave elements. In their method each element is divided into a row of narrow strips which can be considered as planar rectangular transducers whose exact SIRs are available. However, two type of integrals,

the convolution and the summation over all the thin strips, should be effectively done for each element. Moreover, their time-domain solution cannot be used to simulate the behavior of the field in an attenuating medium. Frequency dependent attenuation has a significant impact on ultrasound propagation in human body and cannot be ignored. A time domain method which has applications for attenuating media is the method proposed by Piwakowski and Sbai [63]. In their method, the **d**iscrete **r**epresentation **a**rray **m**odelling (DREAM) procedure is used to calculate the field radiated from arbitrary structured transducer arrays. Their formulation can be applied to predict the acoustic fields in a power law type attenuating medium. They presented the solution for the case where the absorption increases linearly as a function of frequency. However to generalize this method, the velocity dispersion should be introduced and the relation for the complex wave number that guarantees a causal solution should be known.

We seek a more flexible frequency domain method which can predict the spatial response of a cylindrically radiator in any physically realizable lossy medium. As discussed previously the expression for SIR for the frequency domain applications is difficult to evaluate in stable and efficient manner. The high frequency content of the oscillatory kernel is typically handled with high sampling rates which result in an unacceptable computation time.

Our approach to the problem is significantly different from the existing methods in the sense that we propose an analytical solution to the problem. The method we propose in this dissertation complements the methods in the literature such that, with a new rapid integral formulation, the spatial transfer response for cylindrical radiators for any type of lossy homogenous media is obtained almost immediately and has a closed form expression. We follow the

approach of a relevant time domain work of Theumann et al. with the inspiration of Arditi et al. [60, 64]. Theumann et al. worked with concave cylindrical transducers and reduced the surface integral of the impulse response into a single integral for which numerical methods are employed to obtain the result. The philosophy of our approach is similar to that, but we propose an analytical solution to the problem. The line integral kernels are expanded as a truncated series of Legendre polynomials which could be integrated exactly term by term. The resulting response is represented as summation of a few number of Bessel functions.

Although, our main interest lies in the simulating the forward field from clinically used phased array transducer, our initial efforts were concentrated on the modeling of the forward field from spherically focused transducer in a lossy medium [65]. The computations for this case is easier therefore allowed us to focus on matching the computation model to the experimental data.

Objective of the Study: The aim in this study is to develop three dimensional ultrasonic imaging methods to determine the spatial changes in all three acoustic properties -attenuation, sound speed and density- of the HIFU lesion. For this purpose:

- A well calibrated physical model describing the propagation and scattering of ultrasound in human tissue should be developed. The effect of the changes in the acoustic properties -sound speed, attenuation and density- on the acoustic wave behavior should be described with the model.
- The forward model should be validated with experiments using clinically used ultrasound transducers.

- Image reconstruction algorithms should be developed to observe the changes in the sound speed, attenuation and density in HIFU lesions and the algorithm should be tested with experimental measurements.

1.1 Outline of the Thesis

In this work after a short introduction on HIFU and existing lesion imaging techniques (Chapter 1), a time domain model describing the propagation and scattering of ultrasound in a homogeneous medium is given (Chapter 2). The propagation of ultrasound waves in a dispersive, lossy medium is discussed in Chapter 3 and a compact linear relation between the measured backscatter data and the medium parameters (sound speed, attenuation and density) is presented. In Chapter 4 a new method to compute the forward field from cylindrically concave transducers is discussed. In Chapter 5 the inverse problem (obtaining the shape of the HIFU lesion from ultrasonic measurements) is introduced and the reconstructions with simulated and measured backscatter data are presented. The thesis is concluded in Chapter 6 and the work that remains to be done in this area is discussed.

Propagation of Ultrasound in Time Domain

Pulse-echo ultrasound imaging is a widespread non-invasive imaging modality using acoustic waves. Although it is safe, widely available, easy to use, portable, and provides real-time imaging, the resulting images are subjective and relative, depend on the properties of the transducer used, and distorted by spatially varying transducer field.

The physical basis for the problem of interest in this chapter is to calculate the acoustic field scattered by a localized inhomogeneity embedded in a homogeneous background. We consider the case of the received signal for a monostatic pulse-echo configuration although it is straightforward to generalize our results to bi-static geometries.

In pulse-echo ultrasound imaging a single transducer is used to both transmit an acoustic pulse and receive acoustic echoes. An electromechanical transfer function is associated with the transducer for both the transmit process (converting the electrical excitation into an acoustic disturbance) and the receive process (converting the acoustic disturbance into an electrical signal). To characterize

the emitted and received acoustic pulse and to accomplish transducer calibration, the electromechanical response of the transducer must be determined.

In this chapter we present a time domain model which describes the propagation and scattering of ultrasound in homogeneous medium, under the assumption of weak scattering. We provide a framework for calibration which consistently integrates much of the previous literature in this area. We examine in detail the case of a spherically focused transducer and prove that the electromechanical response can also be measured by the use of a point target as well as a plate reflector. We show both theoretically and experimentally that the scattered signal from a plate and point target are related by double differentiation in time. In particular, we bring to attention to a possible misinterpretation of data taken from a flat-plate when applied to scattering from a point target.

The chapter is organized as follows. The following section defines the inhomogeneous wave equation and explains the linearity assumptions made to obtain a solvable equation. It also introduces the concept of calibration and gives the necessary background to the reader. In Sections 2.2 and 2.3 the scattering of sound from flat-plates and point targets is discussed. Section 2.4 combines the ideas introduced in the previous sections and discusses the scattering of sound in the framework of calibration and underlies the overlook in the literature. The comparison of predicted and measured pressure fields are given in Section 2.5. The chapter is concluded in Section 2.6.

2.1 Theory and Background

In this section we discuss the theory of scattering of sound and the relation between the electromechanical impulse response of a transducer and the measured

back scattered signal from specific obstacles.

In his cited work Jensen [66] provided a computationally compact and useful method for simulating the scattered field from arbitrary shaped weak scatterers. For completeness of the dissertation the formulas and derivations in [66] will be summarized here.

2.1.1 Jensen's Formulation

Let V' be an inhomogeneity embedded in a homogeneous fluid medium of constant sound speed c_o and density ρ_o . The linear wave equation for acoustic pressure $p(r, t)$ in time domain can be defined as [67]:

$$\nabla^2 p(r, t) - \frac{1}{c_o^2} \frac{\partial^2 p(r, t)}{\partial t^2} = \frac{-2\Delta c(r)}{c_o^3} \frac{\partial^2 p(r, t)}{\partial t^2} + \left(\frac{1}{\rho_o} \nabla(\Delta \rho(r)) - \frac{\Delta \rho(r)}{\rho_o^2} \nabla(\Delta \rho) \right) \cdot \nabla p(r, t) \quad (2.1)$$

where

- p is the acoustic pressure and depends on space, r , and time, t .
- Δc and $\Delta \rho$ are the space dependent perturbations from the mean values c_o and ρ_o :

$$\rho(r) = \rho_o + \Delta \rho(r)$$

$$c(r) = c_o + \Delta c(r)$$

The terms on the right hand side of Eq.(2.1) are the scattering terms (scattering function) that vanish for a homogeneous medium. The scattered field is calculated by integrating all the spherical waves emanating from the scattering region V' using the time dependent Green's function for unbounded space. Using r and r' for source and scatterer (observation point) coordinates (Fig. (2.1))

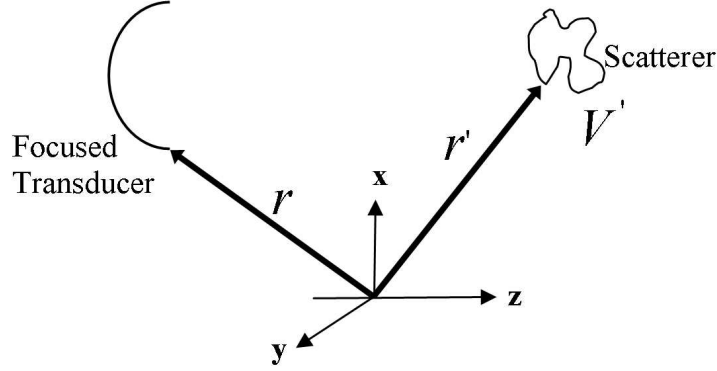


Figure 2.1: Schematic showing the transducer/scatterer arrangement.

and ignoring the second order term in the scattering function the scattered field can be calculated as [68]:

$$\begin{aligned}
 p_s(r, t) = & \int_{V'} \int_T \left[\frac{-2\Delta c(r')}{c_o^3} \frac{\partial^2 p(r', t')}{\partial t^2} \right] G(r, r', t, t') dt' d^3 r' \\
 & + \int_{V'} \int_T \left[\frac{1}{\rho_o} \nabla(\Delta \rho(r', t')) \cdot \nabla \underbrace{p(r', t')}_{p_s(r, t') + p_i(r, t')} \right] G(r, r', t, t') dt' d^3 r' \quad (2.2)
 \end{aligned}$$

where $G(r, r', t, t')$ is the Green's function for the Helmholtz equation in a homogeneous medium. In an unbounded three dimensional medium $G(r, r', t, t')$ is given by

$$G(r, r', t, t') = \frac{\delta(t - t' - |r - r'|/c_o)}{4\pi|r - r'|} \quad (2.3)$$

The pressure field inside the scattering region V' can be defined as $p(r, t') = p_s(r, t') + p_i(r, t')$ where $p_i(r, t')$ is the incident pressure field.

At first glance it might appear as if Eq.(2.2) is the solution we seek for the scattered field, but we have written the integral equation for p_s in terms of the *unknown* total field. Eq.(2.2) is the Fredholm integral of the second kind and

cannot be solved directly. The use of numerical methods, such as Finite Element Method or Method of Moments are required to obtain a solution. To simplify the equation, Born-Neumann approximation of the first kind is invoked. The contrast of the scatterer is assumed to be weak, and total field inside the scattering region is approximated with the incident field [68, 69], $p(r, t') \cong p_i(r, t')$.

Using the definition of the incident field and the spatial impulse response of the transducer given in [60] and applying Born-Neumann expansion of the first kind, Jensen [66] showed that it is possible to write Eq.(2.2) in a closed form expression.

$$p_s(r, t) = v_{pe}(t) *_t \int_{V'} f_m(r') \times h_{pe}(r, r', t) d^3 r' \quad (2.4)$$

where

$$\begin{aligned} v_{pe}(t) &= \frac{\rho_o}{2} E_m(t) *_t \frac{\partial v(t)}{\partial t} \\ f_m(r') &= \frac{\Delta \rho(r')}{\rho_o} - \frac{2 \Delta c(r')}{c_o} \\ h_{pe}(r, r', t) &= \frac{1}{c_o^2} \frac{\partial^2 H_{pe}(r, r', t)}{\partial t^2} \end{aligned}$$

Here v_{pe} is the pulse echo wavelet which includes the transducer excitation and the electromechanical impulse response, $E_m(t)$, during transmission and reception of the pulse; f_m is the scattering function and stands for the inhomogeneities in the medium; and h_{pe} is the modified pulse echo impulse response that relates the transducer geometry to the spatial length of the scattered field. H_{pe} is the pulse-echo spatial impulse response obtained by $H_{pe} = h(r, r', t) *_r h(r', r, t)$. Here h is the impulse response of the transducer which is calculated according to [60]. The reader is referred to [66] for the full derivation of Eq.(2.4).

In case of a point scatterer f_m is a Dirac impulse and Eq.(2.4) reduces to:

$$p_s(r, t) = \frac{1}{c_o^2} \frac{\partial^2 v_{pe}(t)}{\partial t^2} *_{r'} h(r, r', t) *_{r'} h(r, r', t) \quad (2.5)$$

To characterize the scattered field the pulse echo v_{pe} should be accurately determined. In the next section the details of the calibration process, obtaining the v_{pe} signal, is explained.

2.1.2 Calibration Process: Obtaining the v_{pe} signal

The common practice to calibrate a transducer is to place a large flat-plate in the focal plane of a focusing transducer ([70–72]). A waveform measured under these conditions, can, in principle, be used to aid in the removal or compensation of transducer response and field effects on the measurement of tissue properties ([70–73]).

Following the notation in ([66]) the model for the scattering process, Eq.(2.2), can also be summarized by the following equation:

$$v_o(t) = v_i(t) *_t e_T(t) *_t h_T(r, t) *_t s(r, t) *_t h_R(r, t) *_t e_R(t) \quad (2.6)$$

where $v_i(t)$ is the excitation voltage, $e_T(t)$ is the electromechanical response that is the ratio of the derivative of the normal particle velocity with respect to time relative to the transmit voltage, $h_T(r, t)$ is the transmit spatial impulse response, $h_R(r, t)$ is the receive spatial impulse response of the transducer located at position vector r , $s(r, t)$ is a scattering term located at r which accounts for perturbations or inhomogeneities in the medium that give rise to the scattered signal, $v_o(t)$ is the output voltage from the transducer, $e_R(t)$ is the receive voltage to force electromechanical response, and $*_t$ is convolution with respect to time.

We define the round-trip pulse-echo electromechanical impulse response of the transducer, $e_{pe}(t)$ as:

$$e_{pe}(t) = v_i(t) *_t e_T(t) *_t e_R(t) \quad (2.7)$$

For the case where $v_i(t)$ is a very short electrical impulse (e.g., less than about $1/10^{th}$ of the characteristic period of the transducer) e_{pe} will be proportional to $e_T *_t e_R$ which is the true electromechanical impulse response of the transducer. Equation (2.6) can now be written as

$$v_o(t) = e_{pe}(t) *_t h_T(r, t) *_t s(r, t) *_t h_R(r, t) \quad (2.8)$$

where the remaining terms account for propagation and scattering. If one assumes that the absorption of the medium (e.g. de-ionized and de-gassed water in the low megahertz frequencies) is negligible then analytical expressions exist for h_T and h_R for a spherically focused transducer ([60, 74]). The scattering term $s(r, t)$ depends on the target.

In this study we will discuss scattering from three different obstacles: a flat-plate, a point target and an arbitrary shaped weak scatterer. The first two cases will be presented for calibration and the third for imaging applications that require such calibration.

2.2 Scattering from a flat-plate

In this section, we discuss the conditions under which the focal plane reflection from a flat-plate is a valid approximation of the electromechanical impulse

response.

When the flat-plate is an ideal acoustic mirror, and placed at a distance z from the transmitter, perpendicular to the beam axis, the receiver can be considered as the mirror image of the transducer. Hence in pulse-echo imaging of an acoustic mirror, the problem is the same as that of two identical transducers separated by a distance $2z$, as shown by Rhyne (1977), and Chen et al. (1994) for both nonfocusing and focusing transducers.

In 1977 Rhyne derived a “radiation coupling” function for nonfocusing transducers where he calculated the reflection from a flat-plate. This result is the same as the problem of finding diffraction loss, D_F , between two identical transducers at a distance $2z$ ([75, 76]). In both cases, this loss represents the reduction in amplitude and change in phase when only a portion of a transmitted beam is intercepted by a receiving transducer.

For a focusing aperture, Chen et al.([77]) showed that for the mirror placed in the focal plane, the diffraction loss in the frequency domain is equal to

$$D_F(z = 2F, f) = -\{1 - \exp(jG_p)[J_0(G_p) - jJ_1(G_p)]\} \quad (2.9a)$$

where the pressure focal gain is

$$G_p = \frac{\pi f a^2}{c_o F} \quad (2.9b)$$

in which f is frequency, c_o is the speed of sound in water, a is the aperture radius, and F is the focal length. Chen et al. ([71]) found that this expression has only a weak dependency of frequency. If the argument parameter G_p is large, an asymptotic expression for Bessel functions of large arguments (Eq. 9.2.1 of

[78]), can be used to approximate Eq.(2.9a) by

$$D_F(z = 2F, f) \approx -\left\{1 - \sqrt{\frac{2}{\pi G_p}} \exp\left(\frac{j\pi}{4}\right)\right\} = -\left\{1 - \frac{1}{\sqrt{\pi G_p}} - \frac{j}{\sqrt{\pi G_p}}\right\} \quad (2.10)$$

When $G_p \geq 16$ the error of either the real or imaginary part of Eq.(2.10) compared to Eq.(2.9a) is less than 0.042. Because the terms involving the square root are small, the main contribution comes from the real part of Eq.(2.10). Both Eq.(2.9a) and Eq.(2.10) vary extremely slowly with frequency over a transducer bandwidth (e.g. 90% fractional bandwidth), so to a good approximation, the frequency can be set equal to transducer center frequency, $f = f_c$. Physically the result of this small loss can be interpreted in terms of ray theory as a cone of energy focused onto a plate and reflected back, almost but not quite perfectly, along the same cone to the aperture of the transducer.

To use the transfer function defined in Eq.(2.10) in Eq.(2.7), we must account for propagation delays to and from the plate and for the case where the plate is not an ideal reflector. Then we can carry out an inverse Fourier transform to obtain the time domain response. Given that a non-ideal mirror has a plane wave pressure reflection coefficient,

$$R_F = \frac{Z_2 - Z_1}{Z_2 + Z_1} \quad (2.11)$$

where Z_2 is the specific acoustic impedance of the reflector and Z_1 , the characteristic impedance of the fluid, then the three rightmost terms of Eq.(2.8)

correspond to the following inverse Fourier transform:

$$\begin{aligned} h_T(r, t) *_{t} s(r, t) *_{t} h_R(r, t) &= \text{Real}\{\mathfrak{S}^{-1}[D_F(r, f_c)R_F \exp(-j2\pi f(2F)/c_o)]\} \\ &= R_F [\sqrt{1/(\pi G_p)} - 1] \delta(t - t_{2F}) \end{aligned} \quad (2.12)$$

From Eq.(2.12) we can see that the acoustic propagation and scattering from plate at the focus of a transducer (that is, $h_T(r, t) *_{t} s(r, t) *_{t} h_R(r, t)$) is a scaled impulse response delayed in time by $t_{2F} = 2F/c_o$. Under these conditions, the output voltage is an amplitude scaled delayed replica of the system response e_{pe} ,

$$v_o(t) \approx R_F [\sqrt{1/(\pi G_p)} - 1] e_{pe}(t - 2F/c_o) \quad (2.13)$$

The round trip reference signal e_{pe} can be determined from the measured output voltage signal, $v_o(t)$, and the scaling constant from Eq.(2.13).

2.3 Scattering from a point target

Often it is necessary to determine scattering from an ideal point scatterer rather than a flat-plate. As an example, determining the spatial impulse response (h_T and h_R) experimentally requires the use of a point scatterer. Moreover, randomly positioned point scatterers form the basis of simulation models for speckle and phantom-like objects that can be created from organized patterns of point scatterers with assigned weighting [79]. In this section, we show how the reflection from a point scatterer can be determined from a flat-plate response.

The starting point for a model of an ideal point scatterer is that of a *rigid* (incompressible) sphere with a diameter much smaller than a wavelength, density

$\rho \gg \rho_o$, and compressibility $\kappa \ll \kappa_o$, where $c = 1/\sqrt{\rho\kappa}$ and $c_o = 1/\sqrt{\rho_o\kappa_o}$. The scattering for this sphere known to be proportional to $-k^2$ ([10]), where $k = \omega/c_o$, and a geometrical factor A . Since the inverse Fourier transform theory of $j\omega$ is $\partial/\partial t$, $-k^2$ corresponds to the transform $(1/c_o^2)\partial^2/\partial t^2$. For this type of target at the origin,

$$s(r, t) = \frac{A}{c_o^2} \frac{\partial^2}{\partial t^2} *_t \delta(t - |r|/c_o) \quad (2.14a)$$

where A is a time-independent quantity that is given by (Eq.8.2.19, [10])

$$A = \frac{a^3}{3} \left(1 - \frac{3}{2} \cos\theta\right) \quad (2.14b)$$

where a is the radius of the scatterer and θ is the scattering angle. For direct backscatter $\theta = \pi$ and A has the value

$$A = \frac{5a^3}{6}. \quad (2.14c)$$

Real transducers have a finite aperture and collect signals over a range of angles, however, for $160 < \theta < 200$, which is appropriate for most ultrasound imaging scenarios, the variation in A over the surface of the transducer is less than 5% and the use of Eq.(2.14c) is appropriate. If this target is placed at the focal point, then each of the spatial impulse responses in Eq.(2.6) reduces to an impulse function centered at $|r|/c_o$ [74],

$$h_T(r, t) = h_R(r, t) = \ell \delta(t - |r|/c_o) \quad (2.15a)$$

where ([60], Eq. 7)

$$\ell = F \left[1 - \left(1 - \frac{a^2}{F^2} \right)^{1/2} \right] \quad (2.15b)$$

Putting these results into Eq.(2.6) for a small spherical target at the focal point, we find

$$v_o(t) = \frac{A\ell^2}{c_o^2} \frac{\partial^2 e_{pe}(t - 2|r|/c_o)}{\partial t^2} \quad (2.15c)$$

therefore, the reflected signal from a point target will have the same shape as the doubly differentiated reference waveform, $e_{pe}(t)$ with the respect to time.

Although we derived this in terms of a rigid sphere target we note that other targets smaller than a wavelength have a similar functional dependency in the backscattered direction ($\theta = \pi$) towards the transducer at distances greater than a few wavelengths ([80, 81]). In particular, Nassiri and Hill [82] have shown that back scatter from a disc is similar to that of a sphere, differing only in the constant A . Both the sub-wavelength sphere and disc are practical realizations of an ideal point target as viewed at moderate to large distances. Because of the practical difficulties involved in realizing a point target, it may be difficult to determine the constant A . An alternative approach to calibration described by Hunt et al. [74] is to redefine the electromechanical response based on a point target. Their electromechanical response would be the equivalent of e_{pe} convolved with s for a point target from Eq.(2.6) and would include a double differentiation with time. However, if A is not known it is not possible to apply the calibration to the problem of quantitative imaging.

2.4 Scattering from arbitrary shaped weak scatterers: Born Approximation

In the previous two sections we showed that the electromechanical impulse response of a transducer can be measured using either a plate or a point target. Once this reference signal is known, it can be applied to simulate the backscattered field from arbitrary shaped targets through the Born approximation ([66]). Equation 2.4(Equation (44) of ([66])) can be rearranged according to Eq.(2.7):

$$v_o(r, t) = e_{pe}(t) *_t [s(r') *_r \frac{\partial^2 H_{pe}(r', r, t)}{\partial t^2}] \quad (2.16)$$

in which r is the vector to a characteristic position of the transducer and r' represents a vector to a point within the scatterer (Fig. (2.1)) and, as defined by Jensen ([66]),

$$H_{pe}(r', r, t) = h(r', r, t) *_t h(r, r', t) \quad (2.17)$$

is equivalent to $h_T *_t h_R$ in our Eq. (1). More explicitly, Eq.(2.16) is

$$\begin{aligned} v_o(r, t) &= e_{pe}(t) *_t \left[\int_{V'} \left[\frac{\Delta\rho(r')}{\rho_o} - \frac{2\Delta c(r')}{c_o} \right] \frac{1}{c_o^2} \frac{\partial^2 H_{pe}(r', r, t)}{\partial t^2} d^3 r' \right] \\ &= \frac{1}{c_o^2} \frac{\partial^2 e_{pe}(t)}{\partial t^2} *_t \left[\int_{V'} \left[\frac{\Delta\rho(r')}{\rho_o} - \frac{2\Delta c(r')}{c_o} \right] H_{pe}(r', r, t) d^3 r' \right] \end{aligned} \quad (2.18)$$

where $\Delta\rho$ and Δc are the perturbations in density and sound speed with respect to background and V' is the scattering region.

In the case of a point scatterer Eq.(2.18) reduces to:

$$v_o(r, t) = \left[\frac{\Delta\rho(r')}{\rho_o} - \frac{2\Delta c(r')}{c_o} \right] \frac{1}{c_o^2} \frac{\partial^2 e_{pe}(t)}{\partial t^2} *_t h(r', r, t) *_t h(r, r', t) \quad (2.19)$$

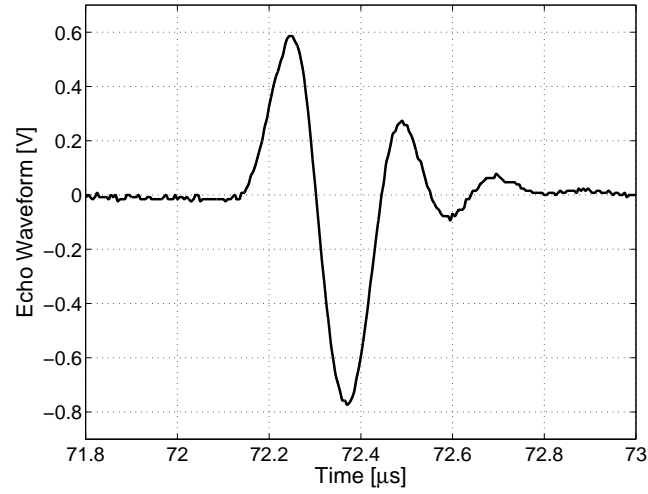
which is consistent with Eq.(2.5) (Jensen's Eq. (50)). Specifically in the case of a *point scatterer* placed at the focal point Eq.(2.19) reduces to the form of Eq.(2.15c). This observation reveals a potential area of confusion with respect to the results in [66], in which Eq.(2.19) is taken to be the response to a *flat-plate* at the focal plane. More correctly, as indicated by the results in the previous two sections of this paper, this flat-plate response is obtained by removing the double time derivative.

In this work the overall outcome of the Born approximation derived by Jensen ([66]) is unchanged. However, we have used the twice time derivative of the plate response in our simulations. The method of finding $e_{pe}(t)$ described in Sections 2.2 and 2.3 can be applied directly to the more general case of scattering through the Born approximation as given by Eq.(2.18).

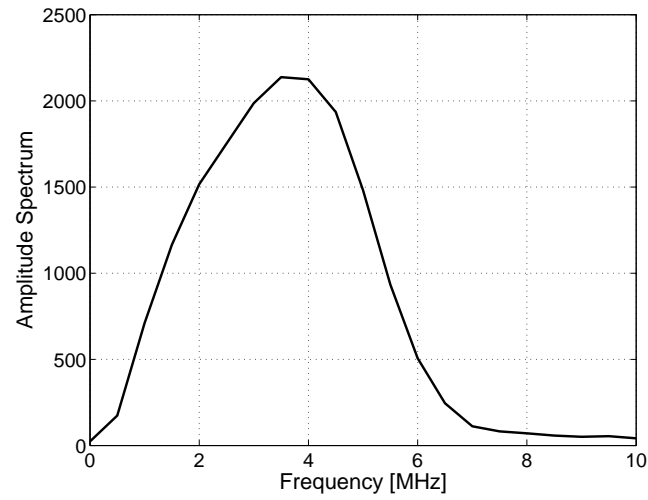
2.5 Experiments

We carried out experiments to verify the fact that the scattered signal from a plate and a small scatterer are related by double differentiation in time. We used a spherically focused ultrasonic transducer, 3.5 MHz, 50.8 mm focal length, 12.8 mm radius (Model V380, Panametrics, Waltham, MA). This strongly focusing transducer (F number 2 and $G_p=24$) was placed in a water tank (0.8 m x 0.8 m x 1.5 m) that was filled with de-ionized de-gassed water at approximately 21°C. The transducer was operated in pulse-echo mode using a pulse-receiver (UA 5052, Panametrics, Waltham, MA). The pulser-receiver excited the transducer with a short excitation signal that approximated a delta function and the received echo was acquired on digital scope (LC 334a, LeCroy,

Chestnut Ridge, NY) and transferred to a computer for later analysis. We investigated the reflections from two targets. The first was a 12.5 mm thick flat acrylic plate acoustic mirror. The second target was from the cleaved end of an optical fiber 110 microns in diameter point scatterer. Figure 2.2(a) shows the reflected pulse measured from the front surface of the acrylic plate, $v_o(t)$. This is the scaled pulse-echo impulse response, $e_{pe}(t)$, according to Eq.(2.12). Here $G_p=24$, so the diffraction correction factor is 0.885 and the reflection coefficient at the water-acrylic interface is $R_F=0.348$. Figure 2.3 compares three normalized waveforms 1) the signal measured from the plate 2) the signal measured from the optical fiber and 3) the doubly differentiated e_{pe} waveform obtained from Eq.(2.8) (note this equation gives a sign inversion). We see that carrying out the double-differentiation is crucial to obtaining good agreement between predictions based on the impulse response of the transducer (e_{pe}) and the received signal from a point scatterer. Without this operation neither the leading negative half-cycle nor the details of the ringdown are captured correctly. This result shows that the time-domain calibration function that is determined from a flat-plate can be used to predict the waveform from a point scatterer at the focus. Once this reference signal is known, it can be applied to simulate the free diffraction field of the transducer or backscattering from other scattering targets. We used Eq.(2.6) with the point scatterer characteristic, Eq.(2.13), and the round trip spatial impulse response (Arditi et al.,1981) with 2 GHz sampling frequency in time, to simulate the echoes scattered from a small point-like target. To confirm our predictions, the optical fiber was mechanically scanned through the tank and echo waveforms recorded at each location. Figure 2.4 shows the measured and predicted contour maps of the amplitude envelope of



(a)



(b)

Figure 2.2: (a) Reference pulse-echo from a large thick acrylic plate placed in the geometric focal plane of a 3.5 MHz spherically focused transducer. (b) Amplitude spectrum of pulse-echo.

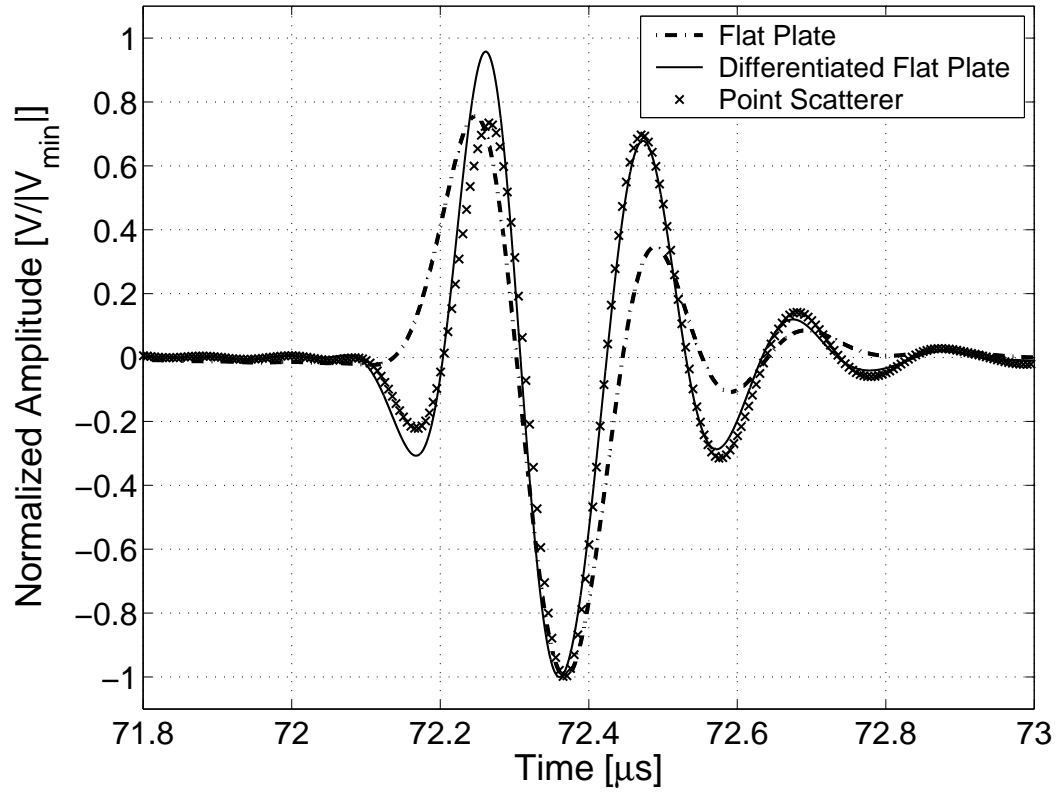
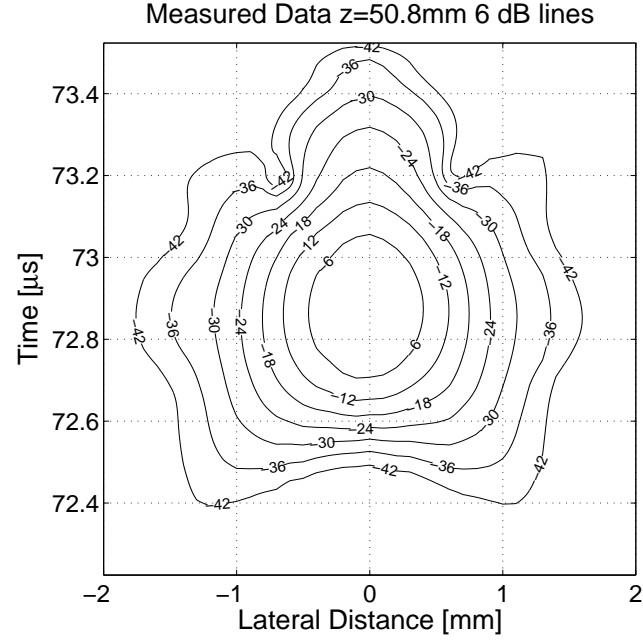


Figure 2.3: Comparison of the flat-plate pulse-echo (Fig. (2.2)(a), normalized and filtered), differentiated flat-plate pulse-echo (Fig. (2.2)(a), normalized and doubly differentiated with respect to time) and a pulse-echo from the tip of an optical fiber placed at the geometric spherical focal point of a 3.5 MHz transducer.

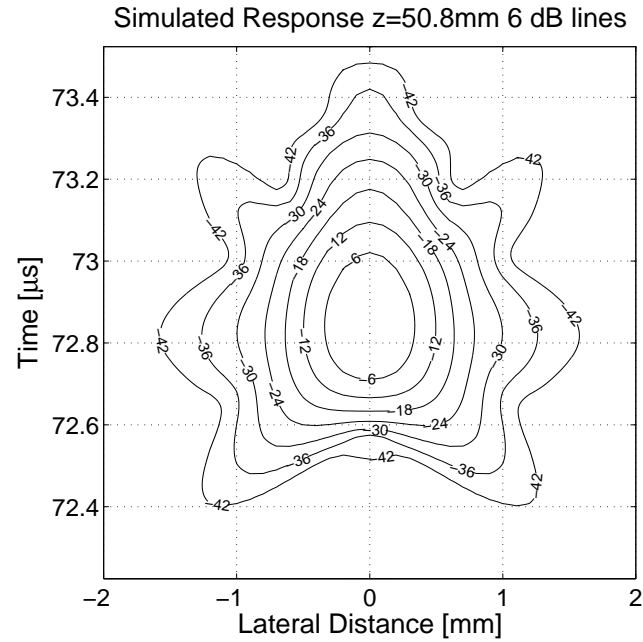
the scattered fields for the case where the fiber was placed in the focal plane and translated perpendicular to the acoustic beam axis. Figure 2.5 is a similar scan but at an axial distance of 53.8 mm (about 3 mm or 10 wavelengths behind of the focus). In both cases, there is a close agreement between the measured and predicted scattered field. The slight differences are attributable to imperfections in both the transducer as an ideal piston source, as determined by extensive hydrophone measurements, and the cleaved optical fiber as an isolated ideal point target. The source transducer was found to have a mildly distorted, asymmetric transmitted field when compared to simulations based on an ideal uniformly weighted piston source. Pulse-echo simulations based on the point target waveform at the focal point gave slightly better agreement with measurements than those shown here; however, we believe this result to be a consequence of the imperfect realization of an ideal spherical scatterer by the cleaved optical fiber which had its own unique response characteristic, as shown in Fig. (2.3). These comparisons confirm that the plate-derived calibration waveform can be used to predict the response of a scatterer anywhere in the field of the transducer.

2.6 Conclusion

We have shown, both theoretically and experimentally, that the pulse-echo impulse response of a spherically focused transducer can be measured using either a flat-plate or a point scatterer. The reflected waveforms in each case are not identical but rather related by an operation of double differentiation. Because of the difficulty of determining the precise geometry of practical realizations of sub-wavelength point targets and, consequently, the calibration constant A , a reflection from a flat-plate is recommended for determination of the reference

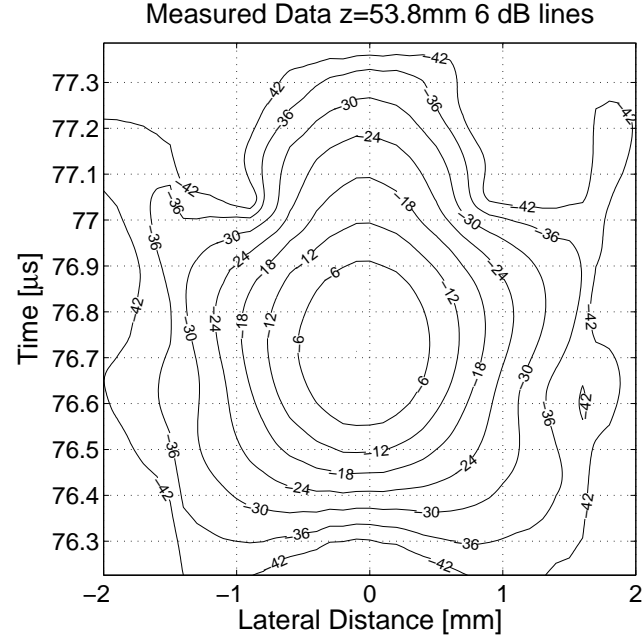


(a)

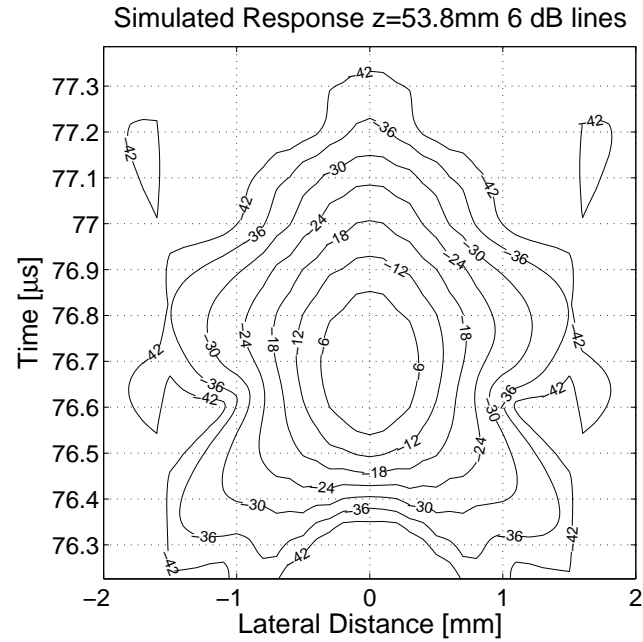


(b)

Figure 2.4: (a) Amplitude envelope of the pulse-echo field of 3.5 MHz transducer as measured by scanning an optical probe laterally at an axial distance equal to the focal length. (b) Amplitude envelope of the simulated pulse-echo field using Eq. (10c) and differentiated signal from Fig. (2.3).



(a)



(b)

Figure 2.5: (a) Amplitude envelope of the pulse-echo field of 3.5 MHz transducer as measured by scanning an optical probe laterally at an axial distance $z=53.8$ mm. (b) Amplitude envelope of the simulated pulse-echo field using Eq. (10c) and differentiated signal from Fig. (2.3)

pulse. For values of focal gain greater than or equal to 16, the error in the approximation (Eq.(2.10)), is less than five percent.

The formulation in Eq.(2.6) and the relation between the flat-plate and point target echoes can be used to resolve differences among various calibration methods in the literature ([66, 70, 71, 74, 83, 84]) each of which can be used self-consistently but may be in conflict with other methods. For example, Hunt et al. [74] obtained a reference waveform from a point scatterer but their formulation for the scatterer does not include the double differentiation of Eq.(2.15c). Their waveform is used consistently to simulate speckle as a summation of random point scatterers.

The time domain Born approximation of Jensen ([66]) in Eq.(2.18) includes the double differentiation and shows that the echo signal from an inhomogeneous medium can be obtained by convolving the point-scattered waveform with the medium properties in agreement with Eq.'s (2.6) and (2.14a). If one wishes to use the signal measured from a flat-plate for this Born model, it is necessary to differentiate the reference signal twice with respect to time first. The wording in Jensen ([66]) could be misinterpreted to mean that the flat-plate signal was already differentiated.

In summary, the commonly used reference waveform from a flat-plate target in the focal plane of a strongly focusing transducer ($G_p \geq 16$) is appropriate to determine $e_{pe}(t)$ without distortion. This reference signal is useful for transducer calibration and diffraction correction ([71, 72, 85, 86]). However, the waveform must be used with care for other scattering targets.

In the next chapter the ideas that have been developed in this section will be applied to the frequency domain.

Propagation of Ultrasound in the Frequency Domain

Propagation of ultrasound can accurately be predicted for a non-attenuating medium e.g. water by using the methods derived in the previous chapter. In Chapter 2 we presented a time domain model which describes the propagation and scattering of ultrasound in a homogeneous medium. However, the behavior of the field cannot be characterized for a lossy, attenuating medium.

Since the human tissue shows a dispersive ultrasound absorption, the frequency dependent attenuation plays a prominent role in ultrasound imaging applications. For most materials including biological tissues, the frequency dependency of attenuation is characterized by a power-law relation: $\alpha(\omega) = \alpha_o|\omega|^y$, where α_o and y ($0 < y < 2$) are the material-dependent parameters. For quantitative ultrasound imaging, it is important to understand how the pressure field behaves in such media. The apparent approach would be to carry the time domain models of Chapter 2 to the frequency domain and provide a mathematical derivation of the acoustic Born model for a power law attenuating medium.

In this chapter, we first study the propagation of ultrasound waves in a

homogeneous, lossy medium. Next, we use the derived theory to obtain solutions in the presence of weak inhomogeneities via Born approximation. We present a compact linear relation between the measured backscatter data and the medium parameters (sound speed, attenuation and density). We validate the proposed model with experimental data.

This chapter is organized as follows. The first section defines the inhomogeneous wave equation in frequency domain, characterizes the background and the scattering wave numbers and introduces the assumptions to obtain a linear solvable equation. Section 3.2 presents the derivation of the incident field for commercial spherical ultrasound transducers. Section 3.3 discusses the calculation of the measured backscatter signal in frequency domain and introduces a compact relation between the medium parameters and the measured field. In section 3.4 the spatial transfer function for spherically focused transducers is formulated and a fast semi-analytical method is introduced to calculate the response. The comparison of predicted and measured pressure fields for spherical transducers is given in Section 3.5. The chapter is concluded in Section 3.6.

3.1 Derivation of the Scattered Field

In this section we introduce the linear time and frequency domain wave equations which describes the propagation of ultrasound in a homogeneous medium. We start with the equations derived in the previous chapter and extend them for lossy, power law attenuating media.

The time domain equations derived in the previous chapter fails to characterize the behavior of the acoustic field in a lossy, attenuating medium. Hence, we derive the scattered field from an acoustic inhomogeneity of density, sound

speed and attenuation for a lossy medium and give brief details of the assumptions made to linearize the scattering problem.

3.1.1 Acoustic Wave Equation

For a fluid medium with space dependent sound speed and density, the linear wave equation is defined as [81],(page 432):

$$\nabla \cdot \left(\frac{1}{\rho(r)} \nabla p(r, t) \right) - \frac{1}{\rho(r)c(r)^2} \frac{\partial^2 p(r, t)}{\partial t^2} = 0 \quad (3.1)$$

where r is a point in 3-space and t is the time variable. $p(r, t)$ is the pressure at r and t , $\rho(r)$ is the density and $c(r)$ is the speed of sound. After algebraic manipulations this equation can be written as:

$$\nabla^2 p(r, t) - \nabla p(r, t) \cdot \nabla \ln \rho(r) - \frac{1}{c(r)^2} \frac{\partial^2 p(r, t)}{\partial t^2} = 0 \quad (3.2)$$

The frequency domain wave equation is obtained by taking the Fourier transform of the field with respect to the time at each position r . In this study the representation form of the time harmonic relations is chosen as $e^{j\omega t}$. Specifically the instantaneous fields are related to their complex time harmonic forms by $p(r, t) = \text{Re}[p(r)e^{j\omega t}]$. With this definition the linear wave equation in frequency domain is defined as:

$$\nabla^2 p(r, \omega) - \nabla \ln \rho(r) \cdot \nabla p(r, \omega) + k^2(r, \omega)p(r, \omega) = 0 \quad (3.3)$$

where ω is the angular frequency, $p(r, \omega)$ is the pressure at r and ω and $k^2(r, \omega)$ is the squared wavenumber at frequency ω and location r .

For a source distribution $q(r, \omega)$ located at r with frequency ω , the right hand side of Eq.(3.3) is replaced by $q(r, \omega)$:

$$\nabla^2 p(r, \omega) - \nabla \ln \rho(r) \cdot \nabla p(r, \omega) + k^2(r, \omega)p(r, \omega) = q(r, \omega) \quad (3.4)$$

3.1.2 A Model for k^2

A key issue to model the wave behavior in frequency domain is the specification of $k^2(r, \omega)$. In non-attenuating media, $k(r, \omega)$ is a real-valued quantity equal to $\omega/c(r)$. For a dispersive attenuating medium, a frequency dependent imaginary component is introduced. The form of $k(r, \omega)$ to be used in that case is:

$$k = \frac{\omega}{c(r, \omega)} - j\alpha(r, \omega) \quad (3.5)$$

where $c(r, \omega)$ is the dispersive speed of sound and $\alpha(r, \omega)$ is the frequency dependent attenuation coefficient.

Under the Born approximation, the scatterer is viewed as a small perturbation to a homogenous background model, and the scattered field is expressed linearly in terms of this perturbation. Hence we should linearize the problem and define the changes in the three acoustic parameters, as a perturbation to the known homogenous background.

Perturbation in Sound Speed and Attenuation

The first step to linearize the problem is to define the perturbations for the sound speed and attenuation.

We assume the dispersive propagation velocity varies slightly from its mean

background value so that, it can be represented in the following form:

$$c(r, \omega) = c_b(r, \omega) + c_p(r, \omega) \quad (3.6a)$$

We linearize the above expression and for each component define dispersion as perturbation to a slowly varying space dependent part:

$$c(r, \omega) = c_b(r) + c_{bd}(r, \omega) + c_p(r) + c_{pd}(r, \omega) \quad (3.6b)$$

where $c_b(r)$ is the slowly varying space dependent background speed, $c_p(r)$ is the scatterer -perturbation- sound speed, $c_{bd}(r, \omega)$ and $c_{pd}(r, \omega)$ are the background and perturbation dispersions respectively. If we normalize Eq.(3.6b) by a characteristic sound speed c_o , which can be an average over space and frequency, we obtain:

$$\frac{c(r, \omega)}{c_o} = \frac{c_b(r)}{c_o} + \frac{c_{bd}(r, \omega)}{c_o} + \frac{c_p(r)}{c_o} + \frac{c_{pd}(r, \omega)}{c_o} \quad (3.7)$$

We assume weak spatial dependency for $c_b(r)$ and identify $c_b(r)/c_o$ as being the order of unity that is $c_b(r)/c_o = O(1)$. Moreover we define:

$c_{bd}(r, \omega)/c_o = O(\varepsilon)$	Background dispersion is small. The typical value is 0.01.
$c_p(r)/c_o = O(\mu)$	Spatial variation is also small but different than the size of dispersion. The typical value is 0.1.
$c_{pd}(r, \omega)/c_o = O(\mu\varepsilon)$	This term accounts for perturbation dispersion and spatial variation will be smaller than the other two terms.

Repeating the same procedure for attenuation takes a little more thought. The frequency dependency of attenuation will be represented with a power law relation, which is appropriate for the tissue, hence the linearization employed in

Eq.(3.6b) cannot be applied. In other words, attenuation is inherently dispersive. Hence, the terms like $c_b(r)$ or $c_p(r)$ will not appear in the derivation.

We again assume that the attenuation varies slightly from its mean value so that:

$$\alpha(r, \omega) = \alpha_b(r, \omega) + \alpha_p(r, \omega) \quad (3.8)$$

The form of attenuation for power law dependency is:

$$\alpha_b(r, \omega) = \alpha_{bo} \left(\frac{\omega}{\omega_o} \right)^n \quad (3.9a)$$

$$\alpha_p(r, \omega) = \alpha_{po}(r) \left(\frac{\omega}{\omega_o} \right)^n \quad (3.9b)$$

where α_{bo} is constant background attenuation and $\alpha_{po}(r)$ is space dependent perturbation value. For tissue like material the exponent is defined as: $0 < n < 2$. With this form Eq.(3.8) can be written as:

$$\alpha(r, \omega) = \alpha_{bo} \left(\frac{\omega}{\omega_o} \right)^n + \alpha_{po}(r) \left(\frac{\omega}{\omega_o} \right)^n \quad (3.10)$$

We substitute the sound speed and attenuation in Eq.(3.5) with their linearized expressions (Eq.(3.7) and Eq.(3.8)), and ignore the space and frequency dependency for simplicity of the notation, to obtain:

$$k = \frac{\omega}{c_b + c_{bd} + c_p + c_{pd}} - j(\alpha_b + \alpha_p) \quad (3.11a)$$

We will work with this form of k and neglect the second order terms along the

way.

$$k = \frac{\omega}{c_b} \left(1 + \frac{c_{bd}}{c_b} + \frac{c_p}{c_b} + \frac{c_{pd}}{c_b}\right)^{-1} - j(\alpha_b + \alpha_p) \quad (3.11b)$$

$$= \frac{\omega}{c_b} \left(1 - \frac{c_{bd}}{c_b} - \frac{c_p}{c_b} - \cancel{O(\mu\varepsilon)}^0\right) - j(\alpha_b + \alpha_p) \quad (3.11c)$$

We take the square of the both sides of Eq.(3.11c) and neglect the small dispersion terms:

$$\begin{aligned} k^2 &= \left(\frac{\omega}{c_b}\right)^2 \left(1 - \frac{c_{bd}}{c_b} - \frac{c_p}{c_b}\right)^2 - j \left(\frac{2\omega}{c_b}\right) \left(1 - \frac{c_{bd}}{c_b} - \frac{c_p}{c_b}\right) (\alpha_b + \alpha_p) - j(\alpha_b + \alpha_p)^2 \\ &= k_{br}^2 \left[1 - 2\frac{c_p}{c_b} - j2\left(1 - \frac{c_p}{c_b}\right) \frac{(\alpha_b + \alpha_p)}{\underline{\underline{k_{br}}}} - j \frac{(\alpha_b + \alpha_p)^2}{\underline{\underline{k_{br}^2}}} \right] \end{aligned} \quad (3.12)$$

where $k_{br} = \omega/c_b$.

If we assume α_b/k_{br} and α_p/k_{br} are small then the terms with double underlining are second order. If we rearrange the terms in Eq.(3.12) and introduce the space and frequency dependency:

$$k^2 \approx \frac{\omega^2}{c_b(r)^2} - j \frac{2\omega\alpha_b(r, \omega)}{c_b(r)} - c_p(r) \left[\frac{2\omega^2}{c_b(r)^3} \right] - \alpha_p(r, \omega) \left[j \frac{2\omega}{c_b(r)} \right] \quad (3.13)$$

As described above, we assume weak spatial dependency for $c_b(r)$ and identify $c_b(r)/c_o$ as being the order of unity, that is $c_b(r) \simeq c_o \simeq c_b$.

We can decompose k^2 into a background $k_b^2(\omega)$ and a perturbation term $k_s^2(\omega, r)$ where $k_s^2(\omega, r)$ is a *linear* function of scattering parameters. That is we write:

$$k_b^2(\omega) = \frac{\omega^2}{c_b^2} - j \frac{2\omega\alpha_b(\omega)}{c_b} \quad (3.14a)$$

$$k_s^2(r, \omega) = c_p(r) \left[-\frac{2\omega^2}{c_b^3} \right] + \alpha_p(r, \omega) \left[-j \frac{2\omega}{c_b} \right] \quad (3.14b)$$

Perturbation in Density

In the previous part we showed that k^2 term can be decomposed into background and perturbation terms under the assumption that, the propagation velocity and the attenuation vary slightly from their mean values. We now take our assumptions one step further and assume the density varies slightly from its mean value as well.

We define $\rho(r) = \rho_b + \rho_p(r)$ where ρ_b is the constant, space independent, background density and $\rho_p(r)$ is the perturbation density, so that:

$$\nabla \ln \rho(r) = \nabla \ln(\rho_b + \rho_p(r)) = \nabla \ln(\rho_b(1 + \frac{\rho_p(r)}{\rho_b})) = \nabla \ln(\rho_b) + \nabla \ln(1 + \frac{\rho_p(r)}{\rho_b})$$

Define $\sigma = \ln(\rho(r)) = \sigma_b + \sigma_p(r, \omega)$ then we can rewrite the wave equation (Eq.(3.4)) in terms of σ as:

$$\nabla^2 p(r, \omega) - \nabla \sigma_p(r) \cdot \nabla p(r, \omega) + k^2(r, \omega) p(r, \omega) = q(r, \omega) \quad (3.15)$$

where

$$\sigma_p(r) = \ln(1 + \frac{\rho_p(r)}{\rho_b}) \quad (3.16a)$$

and for $\rho_p(r)/\rho_b \ll 1$

$$\nabla \sigma_p(r) \approx \frac{\nabla \rho_p(r)}{\rho_b} \quad (3.16b)$$

We now decompose $k^2(r, \omega)$ into $k_b^2(\omega)$ and $k_s^2(r, \omega)$ and reorganize (Eq.(3.15)) as:

$$\nabla^2 p(r, \omega) + k_b^2(\omega)p(r, \omega) = q(r, \omega) + \nabla \sigma_p(r) \cdot \nabla p(r, \omega) - k_s^2(r, \omega)p(r, \omega) \quad (3.17)$$

Equation Eq.(3.17) is the form of the wave equation that will be used in this study.

3.1.3 Born Approximation

The scalar Helmholtz equation (Eq.(3.17)) cannot be solved directly for the scattered field but a solution can be written in terms of the Green's function [10]. The Green's function for this case, $G(r, r', \omega)$, is defined as the solution to the background problem for a δ source located at position r'

$$\nabla^2 G(r, r', \omega) + k_b^2 G(r, r', \omega) = -\delta(r - r') \quad (3.18)$$

For the 3D case it is well known that

$$G(r, r', \omega) = \frac{\exp\{-jk_b|r - r'|\}}{4\pi|r - r'|}$$

where $k_b = \sqrt{k_{b,R}^2 - jk_{b,I}^2}$ is implicitly a function of frequency and for which the sign of the imaginary part is chosen to ensure that the Green's function decays as exponentially.

Based on the linearity of the scattering problem, we can use the Green's function to obtain p as the solution to the Lippman-Schwinger integral equation:

$$\begin{aligned}
p(r, \omega) &= - \int_{V'} G(r, r', \omega) q(r', \omega) d^3 r' \\
&- \int_{V'} G(r, r', \omega) (-k_s^2(r', \omega) + \nabla \sigma_p(r') \cdot \nabla) p(r', \omega) d^3 r' \quad (3.19)
\end{aligned}$$

To simplify matters, we define the incident pressure field $p_b(r, \omega)$ as the first term on the right hand side of (Eq.(3.19)). The Born approximation is invoked by replacing p with p_b in the second term on the right hand side of (Eq.(3.19)). Assuming the incident field is known and defining the scattered field as $p_s = p - p_b$ yields the Born model of interest in this work:

$$p_s(r, \omega) = + \int_{V'} G(r, r', \omega) k_s^2(r', \omega) p_b(r', \omega) d^3 r' - \int_{V'} G(r, r', \omega) \nabla \sigma_p(r') \cdot \nabla p_b(r', \omega) d^3 r'. \quad (3.20)$$

The first term at the right hand side of the equation accounts for the perturbations of the sound speed and the attenuation and is a linear function of these quantities. On the other hand the second term, accounting for the density perturbation, has a gradient term. To simplify the second term on the right hand side of Eq.(3.20) the Green's theorem will be used. For simplicity r and ω dependencies are dropped. By using the vector identities we can write:

$$\nabla \cdot (\sigma_p G \nabla p_b) = G \nabla p_b \cdot \nabla \sigma_p + \sigma_p \nabla p_b \cdot \nabla G + G \sigma_p \nabla^2 p_b \quad (3.21)$$

Therefore the second term on the right hand side of (Eq.(3.20)) can be written

as:

$$\int_{V'} G \nabla \sigma_p \cdot \nabla p_b \, d^3 r' = \int_{V'} \nabla \cdot (\sigma_p G \nabla p_b) d^3 r' - \int_{V'} \sigma_p \nabla p_b \cdot \nabla G d^3 r' - \int_{V'} G \sigma_p \nabla^2 p_b d^3 r' \quad (3.22)$$

By Green's theorem:

$$\int_{V'} G \nabla \sigma_p \cdot \nabla p_b \, d^3 r' = \int_{\partial V'} \sigma_p G \nabla p_b \cdot \hat{n} \, d^2 r' - \int_{V'} \sigma_p \nabla p_b \cdot \nabla G d^3 r' - \int_{\partial V'} G \sigma_p [\hat{n} \cdot \nabla p_b] d^2 r' \quad (3.23)$$

The left hand side of Eq.(3.23) is a volume integral where integrand is a function of the gradient of the density perturbation. The right hand side of the equation involves one volume and two surface integrals, all of which are the linear functions of density. With the assumption of no scatterers on the boundary ($\sigma_p|_{\partial V'} = 0$) the surface integrals vanish. As a result, the scattered field is expressed as a linear function of the all the perturbation values:

$$p_s(r, \omega) = \int_{V'} \{G(r, r', \omega) k_s^2(r', \omega) p_b(r', \omega) + \sigma_p(r') \nabla p_b(r', \omega) \cdot \nabla G(r, r', \omega)\} d^3 r'. \quad (3.24)$$

3.2 Derivation of the Incident Field

The correct characterization of the incident field p_b generated by commercially available transducers is crucial for the solution of Eq.(3.24).

The incident field is generated by the transducer assuming no other sources exist in the medium. For a focused transducer located at r_s with surface area

S, the incident field is calculated with [60, 66, 87]:

$$p_b(\omega, r, k_b, r_s) = \int_S G(r, r_s, r_t, k_b, \omega) \rho_b v(\omega) d^2 r_t \quad (3.25)$$

where r_t represents the vector traversing the transducer surface, and $v(\omega)$ is the Fourier transform of the particle velocity normal to the transducer surface.

Adapting the notation of the previous chapter, this equation can be written as:

$$v_b(\omega, r, k_b, r_s) = e_T(\omega) \int_S G(r, r_s, r_t, k_b, \omega) d^2 r_t \quad (3.26)$$

where v_b is the measured voltage, and $e_T(\omega)$ is the Fourier transform of the transmit electromechanical response of the transducer.

3.3 Derivation of the Received Signal

Having derived the major equations we now calculate the received signal for a bi-static pulse-echo configuration [66]. The schematic showing the transmitter, receiver, and the scatterer locations is given in Fig. (3.1).

We rewrite Eq.(3.20) and incident field p_b in terms of the vectors defined in Fig. (3.1):

$$\begin{aligned} p_s(r_{to} + r_t, \omega) &= \int_{V'} G(r_{to} + r_t, r', \omega) (k_s^2(r', \omega) p_b(r', r_{so}, \omega) d^3 r' \\ &\quad - \int_{V'} \nabla \sigma_p(r') \cdot \nabla p_b(r', r_{so}, \omega) d^3 r' \end{aligned} \quad (3.27)$$

$$p_b(r', r_{so}, \omega) = e_T(\omega) \int_S \frac{e^{-jk|r' - (r_s + r_{so})|}}{4\pi|r' - (r_s + r_{so})|} d^2 r_s \quad (3.28)$$

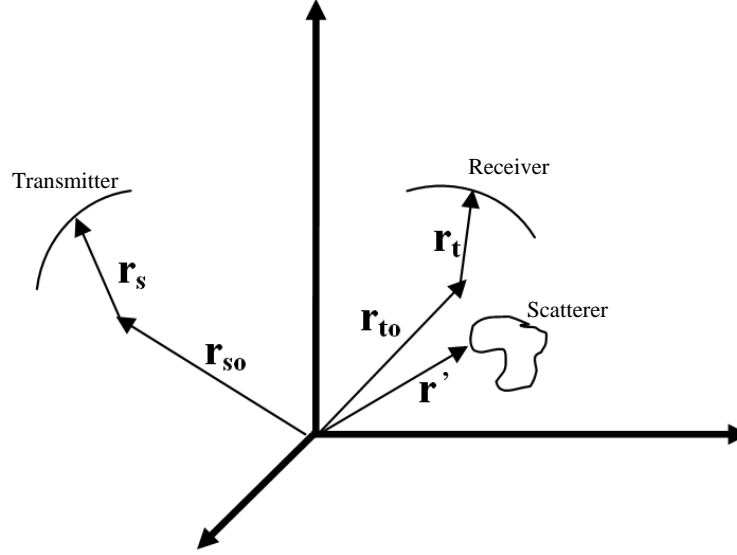


Figure 3.1: Transmitter, receiver, and the scatterer location vectors.

The integral in Eq.(3.28) is the spatial transfer function and it relates the transducer geometry to the acoustic field [60, 83]. By means of this function we can write

$$p_b(r', r_{so}, \omega) = e_T(\omega) H(r', r_{so}, \omega) \quad (3.29)$$

The received signal is the product of the scattered pressure field integrated over the receiver transducer surface and the electromechanical response of the receiver ($e_R(\omega)$).

$$v_o(r_{to}, \omega) = e_R(\omega) \int_S p_s(r_{to} + r_t, \omega) d^2 r_t \quad (3.30)$$

Using this definition and integrating Eq.(3.27) with respect to r_t one readily

obtains:

$$\begin{aligned} v_o(r_{to}, \omega) = & e_T(\omega)e_R(\omega) \int_{V'} H(r_{to}, r', \omega) k_s^2(r', \omega) H(r', r_{so}, \omega) d^3 r' \\ & - e_T(\omega)e_R(\omega) \int_{V'} H(r_{to}, r', \omega) \nabla \sigma_p(r') \cdot \nabla H(r', r_{so}, \omega) d^3 r' \end{aligned} \quad (3.31)$$

Finally using the Green's theorem (Eq.(3.21)-Eq.(3.24))

$$\begin{aligned} v_o(r_{to}, \omega) = & e_{pe} \int_{V'} k_s^2(r', \omega) H(r_{to}, r', \omega) H(r', r_{so}, \omega) d^3 r' \\ & + e_{pe} \int_{V'} \sigma_p(r') \nabla H(r_{to}, r', \omega) \cdot \nabla H(r', r_{so}, \omega) d^3 r' \end{aligned} \quad (3.32)$$

The primary characteristic of Eq.(3.32), is that it provides a linear relation between the real measured backscatter data and the medium parameters.

3.4 Derivation of the Spatial Transfer Function

Key to the implementation of the Born Model is the specification of the spatial transfer function (H) of the commercially available transducers.

This section gives a detailed derivation of the semi-analytic expression for the spatial transfer function of the spherically curved resonators in frequency domain. The time domain formulation of Arditi et al. [60] will be applied to frequency domain with the help of [87]. According to the definition of the spatial transfer function we can write:

$$H(r, \omega) = \int_S G(r, r_t, \omega) dS \quad (3.33)$$

where S corresponds to the transducer surface, r_t is the vector to a point within

the transducer, r is the observation point and G is the Green's function.

The Green's function in 3D for an unbounded media is known to be:

$$G(r, r_t, \omega) = \frac{e^{-jk|r-r_t|}}{4\pi|r-r_t|} \quad (3.34)$$

where k is the *space invariant* wave number.

A conventional approach might be to calculate this integral using numerical integration techniques. For this type of problems numerical methods are not attractive since the integral is highly oscillatory in r_t .

The beauty of Arditi et al.'s time domain approach is converting the 2D surface integral into a 1D line integral for which a closed form analytical solution can be obtained. In frequency domain analytical solution does not exist but it is convenient to apply numerical integration techniques to the resulting line integral [87].

In our study we will use a different approach and project the integrand onto the polynomial space and calculate the integral analytically.

3.4.1 On-axis case

To evaluate Eq.(3.33) Arditi defined three parameters ρ' , ϕ' and $d\beta$ which are shown in Fig. (3.2). R is the focal length of the transducer and O represents the center of curvature. Following his approach and applying the Cosine theorem on OPdS triangle one obtains:

$$H(r_s, \omega) = \frac{1}{4\pi} \int_S \frac{e^{-jkr'}}{r'} dS \quad (3.35a)$$

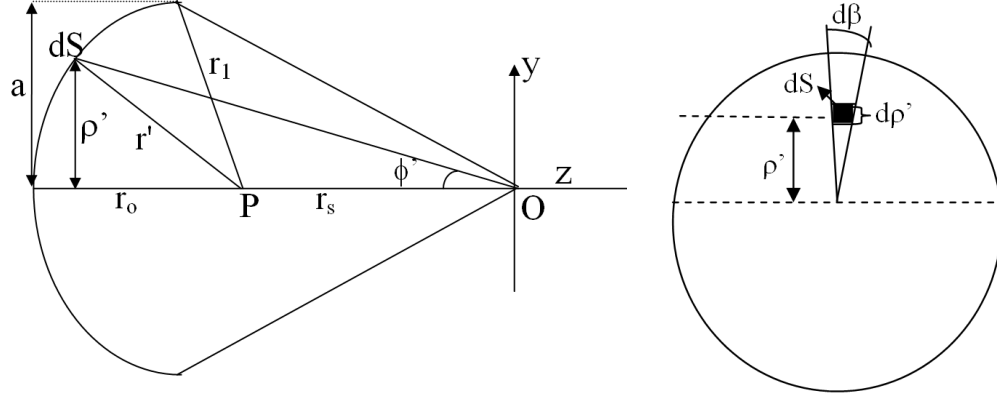


Figure 3.2: Geometry of the problem.(On-axis case)

where

$$dS = \frac{\rho' d\rho'}{\cos\phi'} d\beta = \frac{R}{|r_s|} r' dr' d\beta \quad (3.35b)$$

The limits for β and r' are given in [60]

$$H(r_s, \omega) = \frac{1}{4\pi} \int_0^{2\pi} \int_{r_i}^{r_j} \frac{e^{-jkr'}}{r'} \frac{R}{|r_s|} r' dr' d\beta \quad (3.35b)$$

The final form of the function can be written as:

$$H(r_s, \omega) = \frac{R}{2|r_s|(-jk)} \{e^{-jkr_j} - e^{-jkr_i}\} \quad (3.36)$$

for $z < 0$	for $z > 0$
$r_i = R - r_s$	$r_i = \sqrt{a^2 + (R - d + r_s)^2}$
$r_j = \sqrt{a^2 + (R - d + r_s)^2}$	$r_j = R + r_s$

where

$$d = R(1 - (1 - \frac{a^2}{R^2})^{\frac{1}{2}})$$

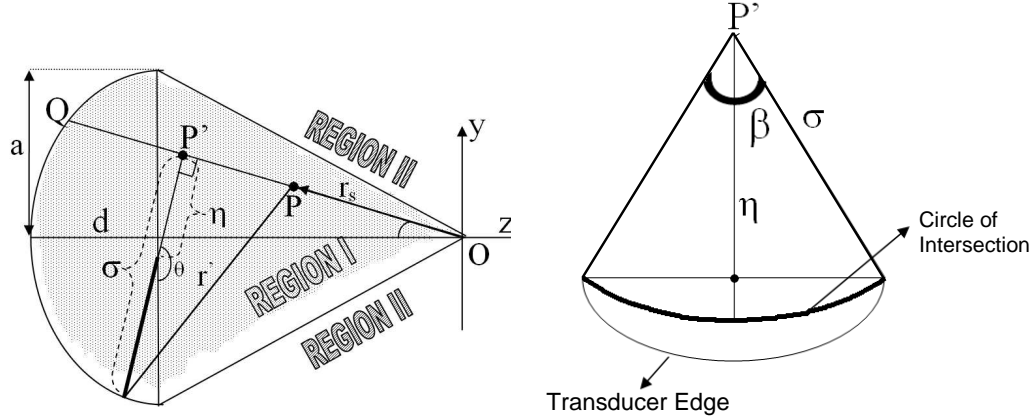


Figure 3.3: Geometry of the problem.(Off-axis case)

is the depth of the concave source, and a is the radius of the circular boundary of the transducer defined in Fig. (3.2).

3.4.2 Off-axis case

To express the transfer function for the off-axis case, the half space in front of the transducer is divided into two regions. Region I corresponds to the points inside the cone subtended by the circular boundary of the transducer and its center of curvature. Region II is defined as the rest of the points in front of the source. The off axis solution can be written as a summation of two responses: $H(r_s, \omega) = H_1(r_s, \omega) + H_2(r_s, \omega)$ where H_2 has the same expression for Region I and II. The geometry associated with this case is given in Fig. (3.3) Here r_s represents the position of the measurement point P.

Region1

As explained before the transfer function is expressed as a summation of two terms (H_1 and H_2). To explain the reason behind this segmentation we will

express the underlying physics in time domain. In time domain, the first part represented by (H_1) is the measured response before the first arrival of the signal from the closest edge of the transducer. In other words, if the axial symmetry around the line OPQ is considered, the on-axis derivation can be applied. In the time interval between the arrivals from the edges, the axial symmetry no longer exists which will be represented by H_2 . Mathematically speaking, H_1 has the same expression as the on-axis case.

Following the same approach as the on-axis derivation for frequency domain, one may write the expression for H_1 as:

$$H_1(r_s, \omega) = \frac{R}{2|r_s|(-jk)} \{e^{-jkr_j} - e^{-jkr_i}\} \quad (3.37)$$

for $z < 0$	for $z > 0$
$r_i = R - r_s $ $r_j = \sqrt{(a - \sqrt{r_{sx}^2 + r_{sy}^2})^2 + M}$ $M = (R - d + r_{sz})^2$	$r_i = \sqrt{(a + \sqrt{r_{sx}^2 + r_{sy}^2})^2 + M}$ $r_j = R + r_s $

where

$$r_s = r_{sx}\hat{\mathbf{x}} + r_{sy}\hat{\mathbf{y}} + r_{sz}\hat{\mathbf{z}}.$$

H_2 has the same expression for both regions and will be defined in the next part.

Region2

For this region there is no axial symmetry and in the time domain, all the contribution to the transfer function comes from the response between the arrivals from the edges of the transducers. In the frequency domain this idea can be expressed as follows:

From the definition of the impulse response one has:

$$H_2(r_s, \omega) = \frac{1}{4\pi} \int_{r_1}^{r_2} \int_0^{\beta(r')} \frac{e^{-jkr'}}{r'} \frac{R}{r_s} r' d\beta dr' \quad (3.38a)$$

$$H_2(r_s, \omega) = \frac{R}{4\pi r_s} \int_{r_1}^{r_2} e^{-jkr'} \beta(r_s, r') dr' \quad (3.38b)$$

where

$$\begin{aligned} r_1 &= ((a - r_y)^2 + (R - d + r_z)^2)^{1/2} \\ r_2 &= ((a + r_y)^2 + (R - d + r_z)^2)^{1/2} \end{aligned}$$

In this region $\beta(r_s, r')$ is no longer a constant, which was 2π on the axis, but subtends the arc length of points on the radiator equidistant from P. This angle and the arc it subtends is shown in Fig. (3.3). The $\beta(r_s, r')$ can be determined from the intersection of the spherical transducer with a sphere of radius r' centered at P and defined as:

$$\begin{aligned} \beta(r_s, r') &= 2\cos^{-1} \left(\frac{\eta(r')}{\sigma(r')} \right) \\ \eta(r') &= R \left\{ \frac{1 - \frac{d}{R}}{\sin\theta} + \frac{1}{\tan\theta} \left(\frac{R^2 + |r_s|^2 - (r')^2}{2|r_s|R} \right) \right\} \\ \sigma(r') &= R \left\{ 1 - \left(\frac{R^2 + |r_s|^2 - (r')^2}{2|r_s|R} \right)^2 \right\}^{\frac{1}{2}} \end{aligned}$$

Equation (3.38b) can not be solved analytically but our observations revealed that β is smooth in the $[r_1, r_2]$ interval and can be approximated by up to 10th

order polynomials with 1.2% error bound. Specifically:

$$\beta(r_s, r') = \sum_{m=0}^{m=10} a_m (r')^m; \quad (3.39a)$$

$$H_2(r_s, \omega) = \frac{R}{4\pi r_s} \sum_{m=0}^{m=10} a_m \int_{r_1}^{r_2} e^{-jkr'} (r')^m dr' \quad (3.39b)$$

With this approximation $H_2(r_s, \omega)$ can be solved analytically.

At the Focus

The response at the focus of the transducer can be found by taking the Fourier transform of the time domain impulse response. The impulse response at the focus of the transducer is [60](eq. 12)

$$h(0, t) = d\delta(t - R/c) \quad (3.40)$$

taking the Fourier transform:

$$H(0, \omega) = d \exp\{-j\omega R/c\} = d \exp\{-jkR\} \quad (3.41)$$

3.5 Wave Propagation Experiment

A wave propagation experiment is performed to validate the Born model and the spatial transfer function formulation of the spherically focused transducer. The data acquisition system used in this experiment is located at Physical Acoustics Laboratory at Boston University. The picture of the system with the water tank

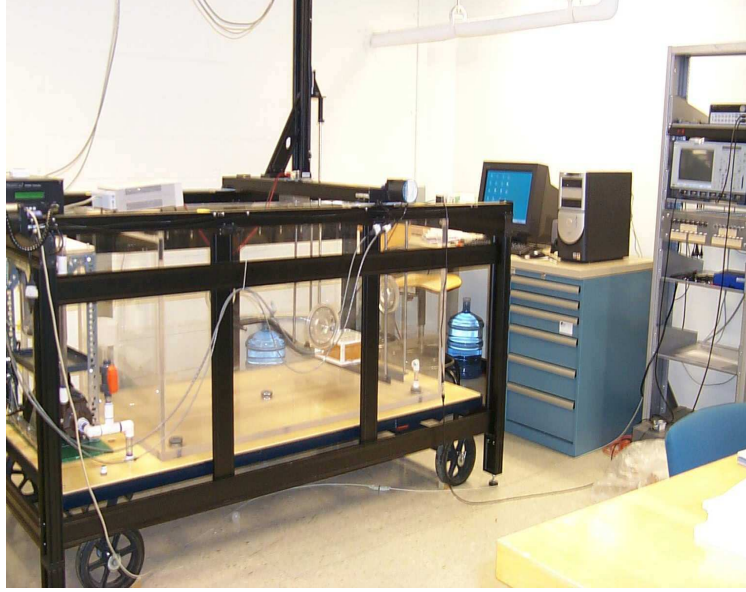


Figure 3.4: Data acquisition system and the water tank in Boston University.

is given in Fig. (3.4). For this experiment Panametrics V380 PZT transducer with 3.5 MHz nominal frequency, 50.8 mm focal length, and 12.8 mm radius is used as the transmitter probe. This strongly focusing transducer (F number 2 and $G_p=24$) was placed in the water tank ($0.8 \text{ m} \times 0.8 \text{ m} \times 1.5 \text{ m}$) that was filled with de-ionized de-gassed water at approximately 21°C . The transducer was operated in transmit mode using a pulser-receiver (UA 5052, Panametrics, Waltham, MA). The pulser-receiver excited the transducer with a short excitation signal that approximated a delta function and the received echo was measured by PVDF Hydrophone with 0.1 mm radius. The data observed on digital scope (LC 334a, LeCroy, Chestnut Ridge, NY) and transferred to a computer for later analysis. The wave propagation through a 80 mm long cylindrical tissue mimicking agar phantom with power law attenuation is measured. Figure 3.5 shows the experimental setup with the agar phantom and the transducers. The nominal properties of the tissue mimicking phantom is given in Table 3.1 with

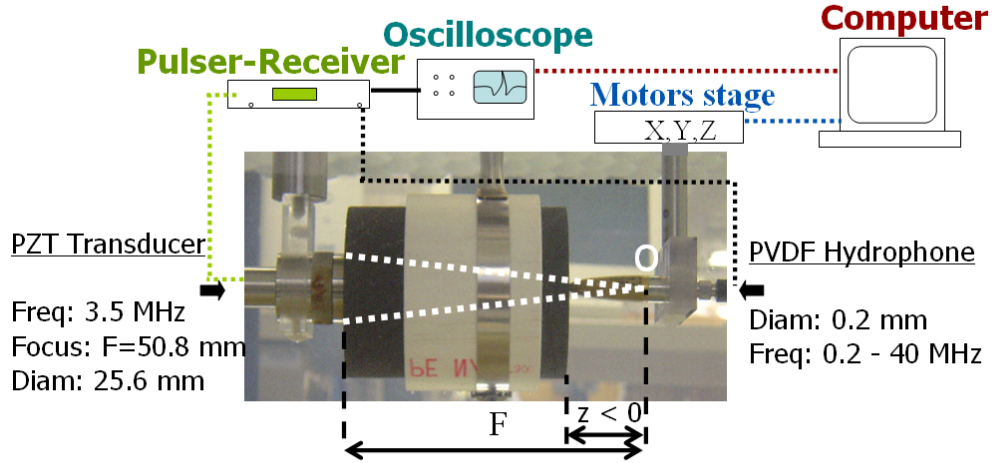


Figure 3.5: Experimental setup with the transducers and the phantom.

the real tissue properties for comparison.

To simulate the pressure fields, the electromechanical response of the transducer, $e_T(\omega)$, should be obtained. For this purpose, a wave propagation experiment was performed in water. The response at the focus of the spherical transducer is measured with the PVDF hydrophone. Next, Eq.(3.29) is used with a simplified Wiener filter and the Fourier transform of the measured water data at the focal point ($p_f(\omega)$):

$$e_T(\omega) = \frac{p_f(\omega)H_f^*(\omega)}{|H_f(\omega)|^2 + q} \quad (3.42)$$

where $H_f(\omega)$ is the spatial transfer function at the focus, and q is the inverse of the signal to noise ratio, and it was chosen to be $0.01\max(|H_f(\omega)|^2)$ based on the data measured at the focus.

Figure 3.6(a) shows the measured and predicted incident field for an off axis measurement ($x=-1.2$ mm, $y=-0.8$ mm) where the receiver hydrophone is placed

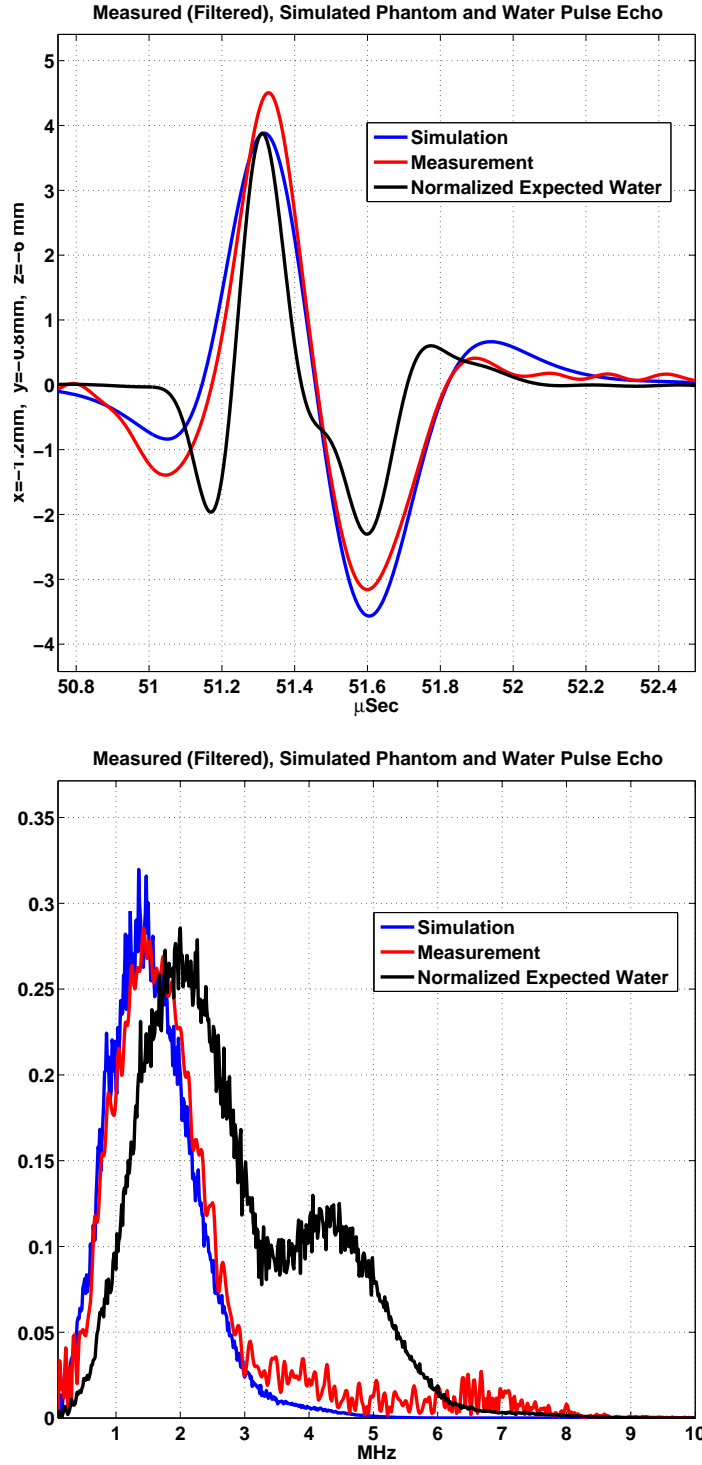


Figure 3.6: Predicted and measured waveforms after propagating through a tissue mimicking phantom

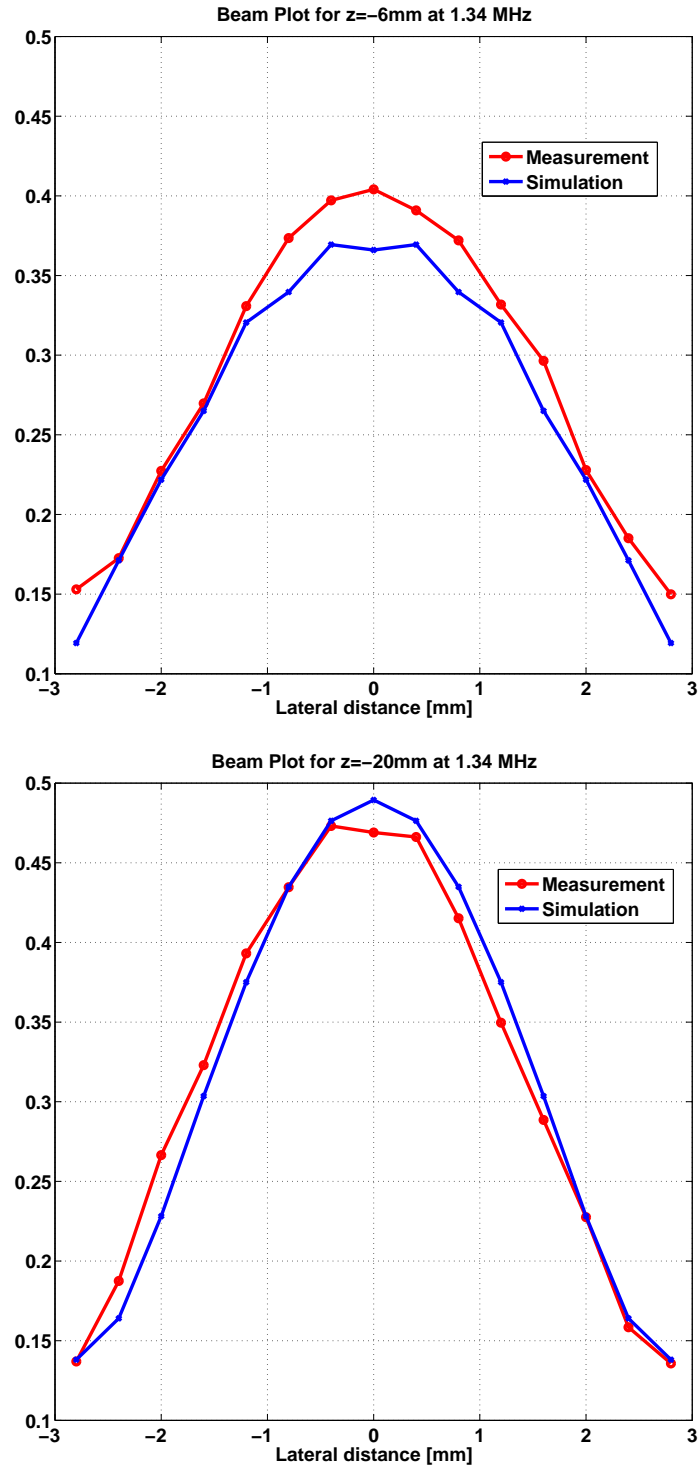


Figure 3.7: Beam plots of the predicted and measured waveforms.

Table 3.1: Nominal acoustic properties of the Agar Phantom

Property	Agar Phantom	Human Tissue
Density (kg/m ³)	1045	1000-1100
Sound Speed (m/s)	1551	1450-1640
Attenuation (Np/m/MHz)	10.17	4-17

at $z=-6\text{mm}$ (see Fig. (3.5)) about 6 mm or 20 wavelengths behind the focus. The transducer-receiver axial distance is 44.8 mm. Figure 3.6(b) shows the same comparison in the frequency domain. To simulate the measured waveforms the equations derived in the previous section for spatial transfer function of the spherical transducer are used with the k_b model derived in Section 3.1. Using the approximate nominal values for the tissue mimicking phantom we were able to get a very good agreement between the model and the experimental data. The frequency dependency of attenuation is found with an optimization routine and is characterized by a power of 1.2. Specifically the parameters used in the simulations are:

$$k_b^2(\omega) = \frac{\omega^2}{c_b^2} - j \frac{2\omega\alpha_b(\omega)}{c_b} \quad (3.43a)$$

where

$$c_b = 1545\text{m/s} \quad (3.43b)$$

$$\rho_b = 1045\text{m/s} \quad (3.43c)$$

$$\alpha_b = 54\left(\frac{\omega}{\omega_o}\right)^{1.2}\text{Np/m} \quad (3.43d)$$

where ω_o is the mean angular frequency ($2\pi 3.5\text{MHz}$) and 54 is obtained by: $12(3.5)^{1.2}$ hence for the attenuation instead of the nominal value, 10.17, we used 12 and for sound speed we used 1545 m/s.

We also studied the effect of absorption on wave propagation and demonstrated that the effect of attenuation cannot be ignored for tissue. The same experiment is simulated using a wave number corresponding to lossless water. The signals that would be measured in this case are plotted in Fig. (3.6)(a)-(b) and significantly different from those measured and modeled from lossy tissue phantom. The normalization constant used for water was 8.6.

For further validation of our model, we placed the PVDF hydrophone at $z=-6\text{mm}$ and $z=-20\text{mm}$ and mechanically moved the receiver perpendicular to the acoustic beam axis between -3mm and 3mm . We compared the maximums of the absolute values of the frequency responses at 1.34 MHz. This particular frequency is chosen from 3.6(b) where the signals reach their peak values. Figure 3.7(a) and (b) shows the comparison for $z=-6\text{mm}$ and $z=-20\text{mm}$ respectively. We again have a very good agreement between the measurements and the simulations.

3.6 Conclusion

In this chapter we concentrated on the development and validation of the frequency domain Born model for medical ultrasound imaging applications.

There are no direct methods for solving the problem of wave propagation in inhomogeneous medium. We therefore linearized our problem and defined the inhomogeneities in the acoustic properties as perturbations to a homogenous, lossy background model. The scattered acoustic wave is expressed linearly in

terms of the perturbations in sound speed, attenuation and density. Since our ultimate interest lies in imaging the human tissue, the frequency dependency of attenuation is characterized by a power-law relation.

We demonstrated a fast method to solve the incident field of spherically curved radiators. The approach we proposed to obtain the spatial transfer function greatly improved the computation time of the Born kernel. To calculate the incident field of the transducer at 225 observation points and 674 frequency values takes only 29 seconds with Matlab 6.5.0 on Pentium 4 machine with 3GHz processor, and 1GByte memory.

We performed a validation experiment where we measured the wave propagation through a tissue mimicking agar phantom with power law attenuation. We simulated the measured field using the dispersive background wave number from Section 3.1 and equations from Section 3.2 and 3.4 that we derived for the spherically focused radiators. The precise match between the measured and simulated data support the validity of the methods developed in this dissertation. We also observed the effect of absorption on ultrasound propagation. Specifically, we showed the signals that would propagate in lossless water are significantly different from those measured from lossy tissue mimicking phantom.

The next step will be the application of these methods to the inverse problem area. The derived compact linear relation between the measured backscatter data and the medium parameters will provide a basis for inversion.

To apply inversion algorithms to clinically obtained data, we would first need a method to compute the pressure field of the clinically used phased arrays. The experience we gained with focused transducers will help us simulate the forward field from phased array transducers that will be presented in the next chapter.

Cylindrically Concave Transducers

Conventional ultrasound transducers used for medical diagnosis purposes are generally of linear array type, consisting of linearly aligned rectangular apertures with cylindrically curved surfaces which are focused in one direction. Typically 1D arrays that have natural focus in the elevation plane are used with electronic focusing along the lateral dimension for beam forming applications. Ideally, each element of the array can be excited individually to obtain non-beam formed data. This type of applications allows us to collect full tomographic data where single transmitter is used to probe the tissue and the response is measured by the collection of the elements of the array. However, to utilize the array transducers for applications beyond traditional beam focusing and steering, it is necessary to have a precise knowledge of the radiated fields generated by the cylindrically curved transducers.

In this chapter we introduce a fast semi-analytical frequency domain method to compute the acoustic field of cylindrically concave transducers in a homogeneous medium by using the spatial impulse response approach. The method

we propose complements the methods in the literature such that, with a new rapid integral formulation, the pressure field due to cylindrical radiators for any type of lossy or lossless media is obtained almost immediately and has a closed form solution expressed with Bessel functions. The speed performance of the semi-analytic technique is compared to an optimized numerical routine and the method is validated with laboratory measurements.

This chapter is organized as follows. Section 4.1, briefly outlines the SIR method and gives the equations that describe the pressure field produced by time-harmonic excitations. In Section 4.2, we derive the integrals to compute the spatial transfer function of the cylindrical radiators. In Section 4.3, we introduce a semi-analytical method to compute those integrals. In Section 4.4, we compare our method with numerical integration techniques and present a comparison of predicted and measured pressure fields.

4.1 Theory: Spatial Impulse Response

For a homogenous fluid medium with a constant sound speed and density, the acoustic field at frequency ω and position \vec{r}_p is calculated with the use of the velocity potential $\Phi(\vec{r}_p, \omega)$ and imposing the appropriate boundary conditions [61, 88]. For a uniform excitation, where the normal particle velocity v_o on the transducer surface is space invariant, i.e. $v_o(\omega, \vec{r}_t) = v_o(\omega)$ where \vec{r}_t is the vector traversing the transducer surface, the velocity potential can be expressed as:

$$\Phi(\vec{r}_p, \omega) = v_o(\omega) \int_S \frac{e^{-jk|\vec{r}_p - \vec{r}_t|}}{2\pi|\vec{r}_p - \vec{r}_t|} dS \quad (4.1a)$$

$$= v_o(\omega) \int_S \frac{e^{-jkr}}{2\pi r} dS = v_o(\omega) H(\vec{r}_p, k) \quad (4.1b)$$

where k is the background wave number, r is the distance from the emitting surface element dS to the observation point P as shown in Fig. (4.1) and $H(\vec{r}_p, k)$ is the spatial transfer function of the transducer. In lossless dispersive media k is a real valued quantity equal to $\omega/c_o(\omega)$, where $c_o(\omega)$ is the speed of sound. For a lossy medium, an imaginary component is introduced,

$$k(\omega) = \frac{\omega}{c_o(\omega)} - j\alpha(\omega) \quad (4.2)$$

where $\alpha(\omega)$ is the frequency dependent attenuation coefficient.

The output voltage from the transducer at point \vec{r}_p is calculated from Eq.(4.1a) as:

$$v(\vec{r}_p, \omega) = j\omega\rho_o v_o(\omega) v_i(\omega) H(\vec{r}_p, k) \quad (4.3)$$

or

$$v(\vec{r}_p, \omega) = e_T(\omega) H(\vec{r}_p, k) \quad (4.4)$$

where ρ_o is the density, $v_i(\omega)$ is the Fourier transform of the driving signal of the transducer and $e_T(\omega)$ is the density scaled electromechanical transfer function.

4.2 Spatial Transfer Function for the Cylindrical Geometry

In this section the spatial transfer function of a concave rectangular transducer will be calculated. The source S is a truncated cylinder with lateral dimensions $l \times h$ and a radius R is given in Fig. (4.1). The focal point of the cylindrical radiator is the origin of the cylindrical coordinates system, and the center of

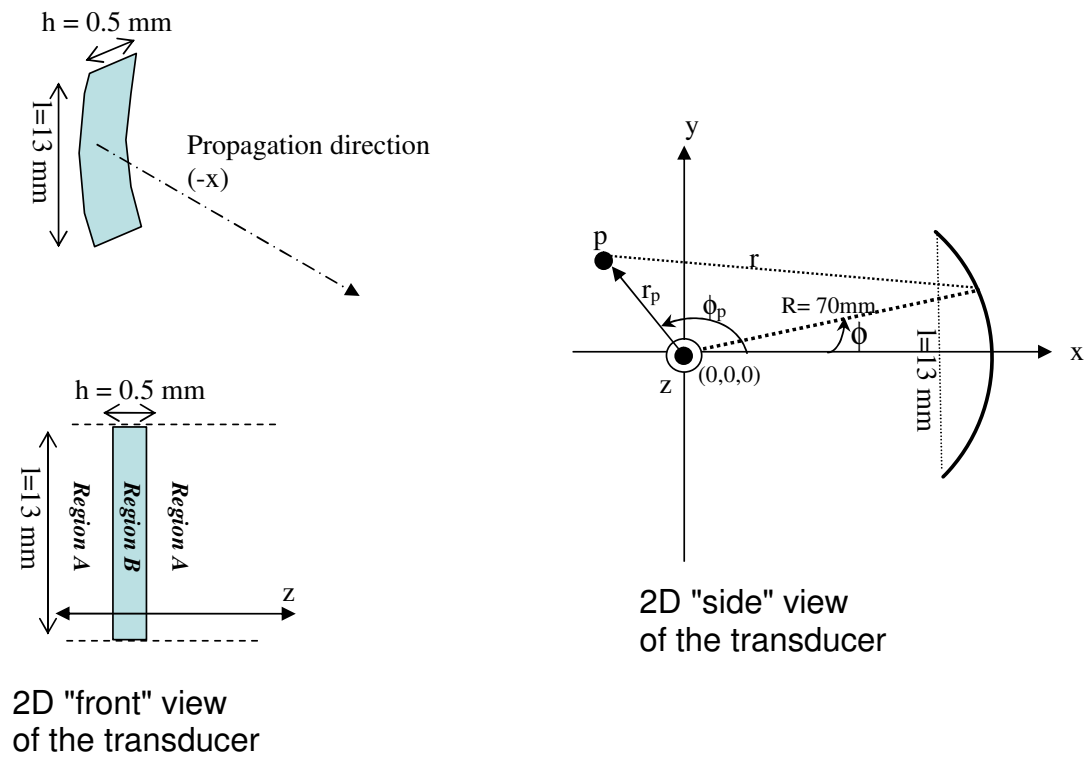
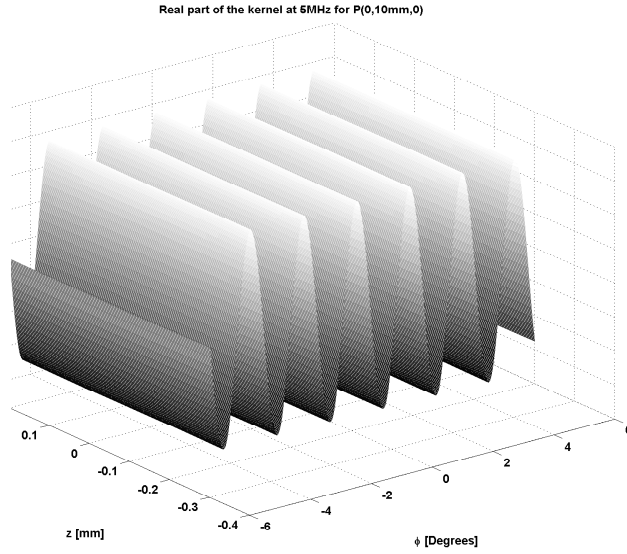


Figure 4.1: The geometry of the transducer and the coordinate system.

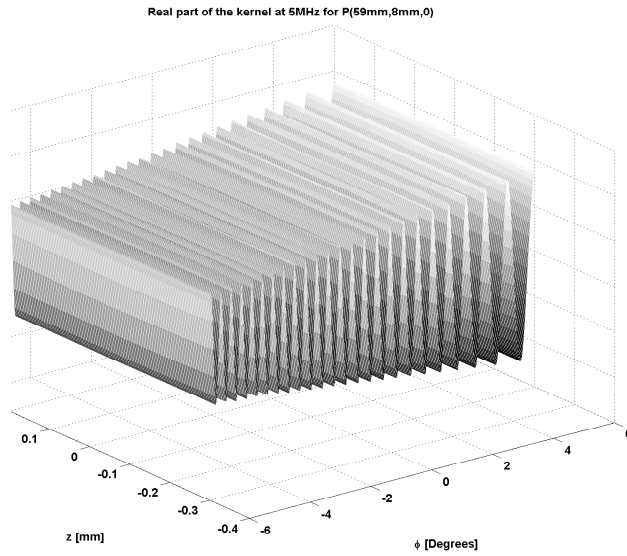
the element is at $(x = R, \phi = 0, z = 0)$ where the negative x direction is the propagation direction. r is the distance from the observation point $p(r_p, \phi_p, z_p)$ to a point on the transducer surface (R, ϕ, z) . The spatial transfer function for this geometry can be expressed as:

$$H(\vec{r}_p, k) = \int_S \frac{e^{-jkr}}{2\pi r} ds \quad (4.5)$$

where S is the radiator surface, and $ds = Rd\phi dz$. When the observation point is close the focal point, the kernel of Eq.(4.5) is a well behaved smooth function. But as the distance between the observation point and the focal point increases, the integral shows an oscillatory behavior. The behavior of the kernel at 5MHz for two observation points, one on the y axis and one close to the transducer is given in Fig. (4.2). The technique to solve this oscillatory integral can be summarized as follows: First a change of variable is employed to smooth the oscillations of the kernel. Specifically, the integral will be expressed in terms of the distance from the observation point to the points on the transducer. This transformation requires space be segmented. In detail, the integrals that would represent the points inside the transducer (Region B in Fig. (4.1)) should have a different expression than the exterior points (Region A in Fig. (4.1)). This transformation will result in elliptical type integrals in terms of the angle parameter. The next step will be to introduce smallness approximation for ϕ , which is appropriate for commercial transducers, and convert the elliptical integrals into quadratic type where closed form analytical solutions exist. The computation of ϕ integrals requires a new segmentation for ϕ_p points. To uniquely define the line integrals, the $x - y$ plane will be divided into five regions (Fig. (4.3)). As a result, the surface integral for the spatial transfer function will be converted into

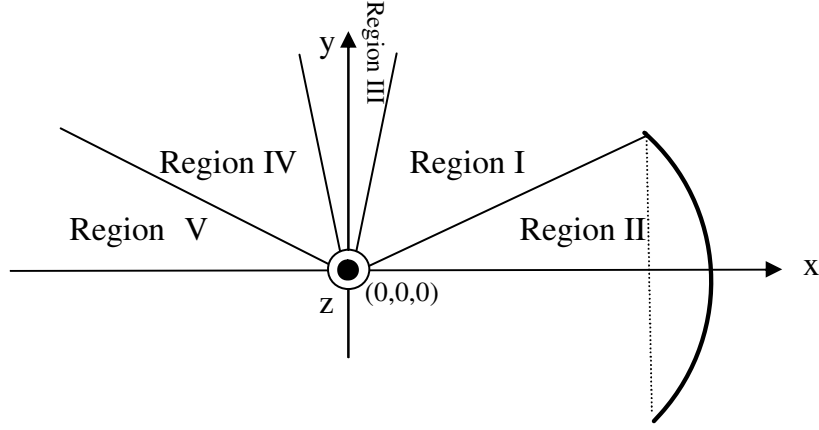


(a)



(b)

Figure 4.2: (a) The oscillations of the real part of the kernel in Eq.(4.5) at 5 MHz for P(0,10 mm,0)(b) The oscillations of the real part of the kernel in Eq.(4.5) at 5 MHz for P(59 mm,8 mm,0)

Figure 4.3: Schematic showing the segmentation for ϕ_p

line integrals. Having reduced the dimension of the integral, the line integral kernels will be expanded as truncated series of Legendre polynomials which can be integrated exactly term by term. The resulting spatial transfer function will be represented as summation of a few number of Bessel functions. In this section the initial steps of our algorithm is introduced. Mainly, Eq.(4.5) is presented in terms of the distance parameter and segmentation for z_p is discussed.

Using the cylindrical coordinates representation, the distance r in Eq.(4.5) can be expressed as:

$$\begin{aligned}
 r^2 &= (r_p \cos(\phi_p) - R \cos(\phi))^2 + (r_p \sin(\phi_p) - R \sin(\phi))^2 + (z_p - z)^2 \\
 &= M(\phi) + (z_p - z)^2
 \end{aligned} \tag{4.6}$$

where $M(\phi) = r_p^2 + R^2 - 2r_p R(\cos(\phi) \cos(\phi_p) + \sin(\phi) \sin(\phi_p))$ contains all the ϕ

dependent terms. Equation (4.5) can be written explicitly as:

$$H(\vec{r}_p, k) = \frac{1}{2\pi} \int_{\phi_{min}}^{\phi_{max}} \int_{-\frac{h}{2}}^{\frac{h}{2}} \frac{e^{-jk\sqrt{M(\phi)+(z_p-z)^2}}}{\sqrt{M(\phi)+(z_p-z)^2}} R dz d\phi \quad (4.7)$$

where $\phi_{max} = \arcsin(\frac{l}{2R})$ and $\phi_{min} = -\phi_{max}$.

First, to simplify the integral, the element $ds = R d\phi dz$ will be expressed as a function of r by eliminating the z dependence. Taking the derivative of the both sides of the Eq.(4.6):

$$dz = -\frac{r}{(z_p - z)} dr \quad (4.8)$$

The sign of the element dz depends on the value of $z_p - z$ at the observation point. The field point z_p can have values between $[-\infty, \infty]$ but the surface point z is limited to the width of the transducer, h . Mathematically speaking, $(z_p - z) = \sqrt{r^2 - M(\phi)}$ for $z_p > z$ and $-\sqrt{r^2 - M(\phi)}$ for $z_p < z$. Hence the new surface element ds will be given as:

$$ds = \pm \frac{r}{\sqrt{r^2 - M(\phi)}} R d\phi dr \quad (4.9)$$

and the correct sign will be determined from the observation point.

The surface S is now a function of r and ϕ , and the new integration limits must be calculated. To express the new integrals, it is convenient to divide the half space in front of the transducer into two regions. Due to the symmetry in $x - y$ and $x - z$ planes of the radiator, the spatial impulse response is symmetric with respect to z and y and the description of $H(\vec{r}_p, k)$ can be restricted to the one quadrant of the $y - z$ plane with $z_p \geq 0$ and $y \geq 0$. The two regions will be

defined as follows:

REGION A ($z_p \geq h/2$) If $z_p > h/2$ (the maximum value of z), then $(z_p - z)$ will always be positive and $ds < 0$. The integral limits for r can be found by substituting the limiting values of z , $(-h/2, h/2)$ in Eq.(4.6). Hence the integral in Eq.(4.7) can be written in terms of r as:

$$\frac{R}{2\pi} \int_{\phi_{min}}^{\phi_{max}} \int_{\sqrt{M(\phi)+(z_p-h/2)^2}}^{\sqrt{M(\phi)+(z_p+h/2)^2}} \frac{e^{-jkr}}{\sqrt{r^2 - M(\phi)}} dr d\phi \quad (4.10)$$

REGION B ($0 \leq z_p < h/2$) If z_p is smaller than the limiting value of z , the integral should be decomposed into two parts for proper calculation.

- If $-\frac{h}{2} \leq z \leq z_p$ then $(z_p - z) \geq 0$ and $ds < 0$. Substituting the limiting values of z , $(-h/2, z_p)$, in Eq.(4.6), the new integral is expressed as:

$$\frac{R}{2\pi} \int_{\phi_{min}}^{\phi_{max}} \int_{\sqrt{M(\phi)}}^{\sqrt{M(\phi)+(z_p+\frac{h}{2})^2}} \frac{e^{-jkr}}{\sqrt{r^2 - M(\phi)}} dr d\phi$$

- If $z_p \leq z \leq \frac{h}{2}$ then $(z_p - z) \leq 0$ and $ds > 0$. The limiting values for z is $(z_p, h/2)$ and the new integral is given by:

$$\frac{R}{2\pi} \int_{\phi_{min}}^{\phi_{max}} \int_{\sqrt{M(\phi)}}^{\sqrt{M(\phi)+(z_p-\frac{h}{2})^2}} \frac{e^{-jkr}}{\sqrt{r^2 - M(\phi)}} dr d\phi$$

As a result, for this region the integral in terms of r can be expressed as:

$$\frac{R}{2\pi} \int_{\phi_{min}}^{\phi_{max}} \left[\int_{\sqrt{M(\phi)}}^{\sqrt{M(\phi)+(z_p+\frac{h}{2})^2}} E(r, \phi) dr + \int_{\sqrt{M(\phi)}}^{\sqrt{M(\phi)+(z_p-\frac{h}{2})^2}} E(r, \phi) dr \right] d\phi \quad (4.11)$$

where for the simplicity of the notation:

$$\frac{e^{-jkr}}{\sqrt{r^2 - M(\phi)}} = E(r, \phi)$$

The type of the integrals that is introduced in this section can be summarized in a compact form such as:

$$\frac{R}{2\pi} \int_{\phi_{min}}^{\phi_{max}} \int_{F_1(\phi)}^{F_2(\phi)} E(r, \phi) dr d\phi \quad (4.12a)$$

where

$$F_1(\phi) = \sqrt{M(\phi) + A_{zp}} \quad (4.12b)$$

$$F_2(\phi) = \sqrt{M(\phi) + B_{zp}} \quad (4.12c)$$

here A_{zp} and B_{zp} represent the region specific constants defined by the z_p value of the observation point.

4.3 Integral Calculation

In the previous section the necessary integrals are derived to compute the spatial transfer function of a cylindrical radiator and a compact form is introduced which summarizes the formulae derived for two different regions. In this section, the mathematical approximations to convert the surface integral presented in Eq.(4.12a) into line integrals will be presented.

We were unable to find an analytical closed form solution for Eq.(4.12a). Specifically, due to the r^2 term in the denominator and the oscillatory expression

e^{-jkr} in the numerator, the exact integral with respect to r could not be obtained analytically. Moreover, the integral is of elliptical type in terms of the angle parameter. However, using the geometry information of the transducer, it is possible to obtain a simpler expression for Eq.(4.12a) which would lead to a closed form solution.

The geometry of the problem given in Fig. (4.1) -the placement of the transducer on the x axis- has a significant role in our method. Given the 2D side view of the transducer in Fig. (4.1) one observes that the maximum value of ϕ (or ϕ_{max}) is $\arcsin(\frac{l}{2R})$. For the most focusing type of transducers, like the one we use in our experiments, the ratio of $l/(2R)$ is small enough that $\cos(\phi)$ can be approximated with $(1 - \phi^2/2)$ and $\sin(\phi)$ can be replaced with ϕ . Specifically, the parameters that actually define the transducer used in this study are $R = 70$ mm and $l = 13$ mm, hence $\arcsin(\frac{13}{140}) \simeq 5^\circ$. By means of this smallness approximation, $M(\phi)$ will be described by:

$$M(\phi) \approx (r_p^2 + R^2 - 2r_p R \cos(\phi_p)) - (2r_p R \sin(\phi_p))\phi + (r_p R \cos(\phi_p))\phi^2 \quad (4.13)$$

The smallness approximation that is introduced on the way converts the elliptical integral in Eq.(4.12a) into a quadratic type which has a closed form solution. Since, the integral with respect to r cannot be obtained analytically, we should change the order of integral in Eq.(4.12a) and attempt to calculate the ϕ integral first. On the other hand, for the observation points on the z axis (when $r_p = 0$) the kernel will be independent of ϕ and this transformation

cannot be employed. Therefore, the points on the z axis should be handled separately.

In the next sections the mathematical details to reduce the type of integrals in Eq.(4.12a) into line integrals will be presented where fast analytical integration techniques can be applied to obtain a computationally efficient solution.

As discussed previously, the first step to obtain the line integrals will be to employ the change of order of integration for r and ϕ . The algebraic details of this alteration depend on the polar angle of the observation point. To uniquely express the transfer function in terms of the angle parameter, the $x - y$ plane is divided into five regions as shown in Fig. (4.3). Region II and V correspond to the points inside the cone subtended by the circular boundary of the transducer and its center of curvature. Region III corresponds to the cone around the y axis and Region I and IV are defined as the rest of the points in the first and second quadrant.

Among all the regions, Region III requires a detailed explanation. The equations that would be derived are originated from Eq.(4.13) where $(r_p R \cos(\phi_p))$ appears as a multiplication constant of ϕ^2 . For the points where $\cos(\phi_p) = 0$, such as the ones on the y axis, the coefficient of this quadratic term is zero. Moreover, for the observation points that are close to the y axis this term will be infinitesimally small. Hence, the expansion employed below fails. For these points, which are close to the y axis, $\cos(\phi)$ will be approximated as unity and the last term in Eq.(4.13) with the troublesome $\cos(\phi_p)$ term is dropped. To minimize the error coming from this approximation, a threshold value should be chosen for the polar angle which minimizes the effect of ϕ^2 on the solution. Specifically the ϕ_p value which satisfies the equation $[(2r_p R \sin(\phi_p) \phi_{max}) > 10^3(r_p R \cos(\phi_p) \phi_{max}^2)]$

was chosen as the boundary between Regions I and III. For the type of the transducer used in this experiment, this threshold value, ϕ_t , was $69\pi/140$ and Region III was defined between $69\pi/140$ and $(\pi - \phi_t) = 71\pi/140$ which was the symmetric interval with respect to the y axis.

The underlying principle to convert Eq.(4.12a) into line integrals is almost similar for all the regions. In this chapter, we will present the full mathematical details for all the regions. The introduced algebra covers all the mathematical tools needed to obtain the response in any observation point in front of the radiator. The reader is referred to the Appendix A section at the end of the thesis for the summary of the equations derived in this section.

4.3.1 Case 1: Regions I and II $0 \leq \phi_p \leq \phi_t$

In Regions I and II, the smallness approximation for ϕ will be employed and $\cos(\phi)$ will be represented with the second order terms in the Taylor series expansion [78]. $M(\phi)$, $F_1(\phi)$ and $F_2(\phi)$ are represented by:

$$M(\phi) \approx (r_p^2 + R^2 - 2r_p R \cos(\phi_p)) - (2r_p R \sin(\phi_p))\phi \quad (4.14a)$$

$$+ (r_p R \cos(\phi_p))\phi^2$$

$$= a + b\phi + c\phi^2 \quad (4.14b)$$

$$F_1(\phi) \approx \sqrt{a + b\phi + c\phi^2 + A_{zp}} \quad (4.14c)$$

$$F_2(\phi) \approx \sqrt{a + b\phi + c\phi^2 + B_{zp}} \quad (4.14d)$$

where to simplify the notation the equations will be represented in terms of a , b and c throughout this section and A_{zp} and B_{zp} represent the region specific constants defined by the z_p value of the observation point. We will first

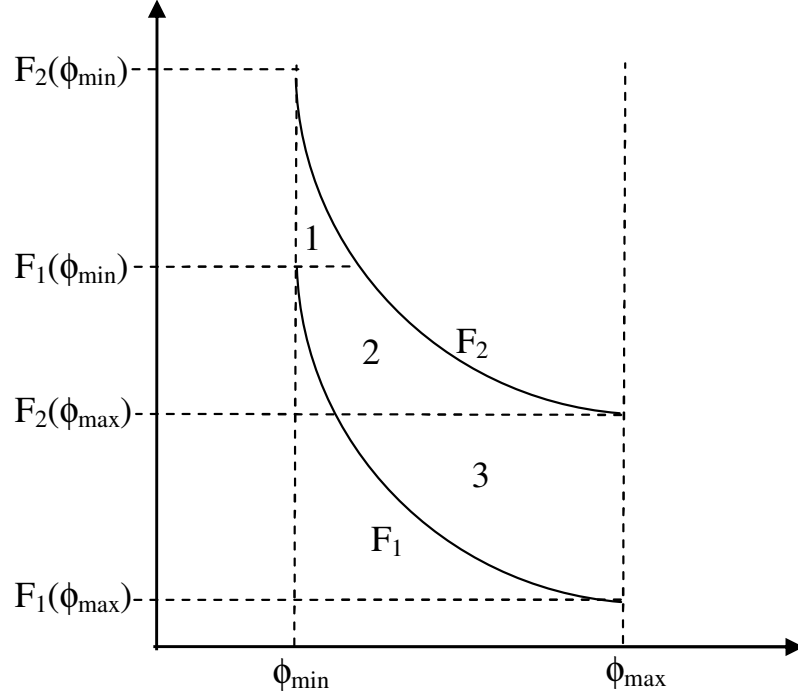


Figure 4.4: The limit functions with monotonic decreasing ϕ dependency.

introduce the solution for Region I, as it sets the basis for the other solutions. The boundaries between the regions are described in terms of $\tan \phi_p$ and the reasoning behind this parameter will be explained in the next section.

Region I: $\phi_{\max} < \tan \phi_p \leq \phi_t$

To reduce the order of the integral given in Eq.(4.12a) change of order of integration will be employed. The region of integration is shown in Fig. (4.4). To facilitate the change of order it was necessary to divide the integral into three pieces.

$$\int_{\phi_{min}}^{\phi_{max}} \int_{F_1(\phi)}^{F_2(\phi)} E(r, \phi) dr d\phi = \quad (4.15)$$

$$\int_{F_1(\phi_{min})}^{F_2(\phi_{min})} \int_{\phi_{min}}^{F_2^{-1}(r)} E(r, \phi) dr d\phi + \int_{F_2(\phi_{max})}^{F_1(\phi_{min})} \int_{F_1^{-1}(r)}^{F_2^{-1}(r)} E(r, \phi) dr d\phi +$$

$$\int_{F_1(\phi_{max})}^{F_2(\phi_{max})} \int_{F_1^{-1}(r)}^{\phi_{max}} E(r, \phi) dr d\phi$$

The mapping functions from r to ϕ which are denoted with $F_1^{-1}(r)$ and $F_2^{-1}(r)$ are not single valued, e.g. $F_1(\phi) = \sqrt{a + b\phi + c\phi^2 + A_{zp}}$ which is a quadratic with two roots. To solve the problem uniquely, the correct root must be picked and this motivates the separation into regions. The derivative of the quadratic term changes sign at $-b/2c = \tan(\phi_p)$. Hence, the boundaries between the regions are described in terms of $\tan(\phi_p)$. For Region I, $\tan(\phi_p) > \phi_{max}$ and the appropriate results are:

$$F_1^{-1}(r) = \phi = \frac{-b - \sqrt{\Delta_1}}{2c} \quad (4.16a)$$

$$\Delta_1 = b^2 - 4c(a + A_{zp} - r^2) \quad (4.16b)$$

$$F_2^{-1}(r) = \phi = \frac{-b - \sqrt{\Delta_2}}{2c} \quad (4.16c)$$

$$\Delta_2 = b^2 - 4c(a + B_{zp} - r^2) \quad (4.16d)$$

Moreover in this region $c > 0$ and the integral with respect to ϕ is given

as [89]:

$$\int \frac{1}{\sqrt{r^2 - (a + b\phi + c\phi^2)}} d\phi = -\frac{1}{\sqrt{c}} \arcsin \left(\frac{-2c\phi - b}{\sqrt{b^2 + 4c(r^2 - a)}} \right) = G(\phi) \quad (4.17)$$

We now proceed to calculate the actual line integrals in terms of r . If we calculate the integral in Eq.(4.15) with respect to ϕ and substitute $F_1^{-1}(r)$ and $F_2^{-1}(r)$ we obtain:

$$G(F_1^{-1}) = \Psi_1(r) = -\frac{1}{\sqrt{c}} \arcsin \left(\sqrt{1 - \frac{4cA_{zp}}{b^2 + 4r^2c - 4ac}} \right) \quad (4.18a)$$

$$G(F_2^{-1}) = \Psi_2(r) = -\frac{1}{\sqrt{c}} \arcsin \left(\sqrt{1 - \frac{4cB_{zp}}{b^2 + 4r^2c - 4ac}} \right) \quad (4.18b)$$

hence, Eq.(4.15) can be written as:

$$\begin{aligned} \int_{\phi_{min}}^{\phi_{max}} \int_{F_1(\phi)}^{F_2(\phi)} E(r, \phi) dr d\phi = & \quad (4.19) \\ & \int_{F_1(\phi_{min})}^{F_2(\phi_{min})} e^{-jkr} [\Psi_2(r) - G(\phi_{min})] dr \\ & + \int_{F_2(\phi_{max})}^{F_1(\phi_{min})} e^{-jkr} [\Psi_2(r) - \Psi_1(r)] dr \\ & + \int_{F_1(\phi_{max})}^{F_2(\phi_{max})} e^{-jkr} [G(\phi_{max}) - \Psi_1(r)] dr \end{aligned}$$

We also define

$$G(\phi_{min}) = \Psi_3(r) = -\frac{1}{\sqrt{c}} \arcsin \left(\frac{-2c\phi_{min} - b}{\sqrt{b^2 + 4r^2c - 4ac}} \right) \quad (4.20a)$$

$$G(\phi_{max}) = \Psi_4(r) = -\frac{1}{\sqrt{c}} \arcsin \left(\frac{-2c\phi_{max} - b}{\sqrt{b^2 + 4r^2c - 4ac}} \right) \quad (4.20b)$$

and present the transfer function in a compact form of four line integrals:

$$H = \frac{R}{2\pi} \left[\begin{array}{cc} \int_{F_1(\phi_{max})}^{F_1(\phi_{min})} e^{-jkr} [-\Psi_1(r)] dr & + \int_{F_2(\phi_{max})}^{F_2(\phi_{min})} e^{-jkr} [\Psi_2(r)] dr + \\ \int_{F_1(\phi_{min})}^{F_2(\phi_{min})} e^{-jkr} [-\Psi_3(r)] dr & + \int_{F_1(\phi_{max})}^{F_2(\phi_{max})} e^{-jkr} [\Psi_4(r)] dr \end{array} \right] \quad (4.21)$$

where

$$\phi_{min} = -\arcsin(l/2R) \quad (4.22)$$

$$\phi_{max} = \arcsin(l/2R)$$

Region II: $\tan\phi_p \leq \phi_{max}$

When $\tan(\phi_p)$ is smaller than the limiting value of ϕ the inverse mapping functions $F_1^{-1}(r)$ and $F_2^{-1}(r)$ change sign in the integral interval. Therefore the integral in Eq.(4.12a) should be decomposed into two parts for unique representation.

$$\int_{\phi_{min}}^{\phi_{max}} \int_{F_1(\phi)}^{F_2(\phi)} E(r, \phi) dr d\phi = H_1 + H_2 = \quad (4.23)$$

$$\int_{\phi_{min}}^{\tan(\phi_p)} \int_{F_1(\phi)}^{F_2(\phi)} E(r, \phi) dr d\phi + \int_{\tan(\phi_p)}^{\phi_{max}} \int_{F_1(\phi)}^{F_2(\phi)} E(r, \phi) dr d\phi$$

To obtain H_1 , the algorithm we used in Region I will be implemented. The limit functions $F_1(\phi)$ and $F_2(\phi)$ are decreasing functions of ϕ and the inverses of the functions are represented with the negative roots, hence the resulting integral

has the similar form with the previous case and can be expressed as:

$$H_1 = \frac{R}{2\pi} \left[\begin{aligned} & \int_{F_1(\phi_{max})}^{F_1(\phi_{min})} e^{-jkr} [-\Psi_1(r)] dr + \int_{F_2(\phi_{max})}^{F_2(\phi_{min})} e^{-jkr} [\Psi_2(r)] dr + \\ & \int_{F_1(\phi_{min})}^{F_2(\phi_{min})} e^{-jkr} [-\Psi_3(r)] dr \end{aligned} \right] \quad (4.24)$$

where

$$\phi_{min} = -\arcsin(l/2R) \quad (4.25)$$

$$\phi_{max} = \tan(\phi_p)$$

The $\Psi_4(r)$ integral vanishes in this interval.

To calculate H_2 the same path will be followed with minor modifications. For this case M and r are the increasing functions of ϕ . The behavior of the limiting functions with respect to ϕ is given in Fig. (4.5). As in Eq.(4.15), we have to divide the integral into three parts for proper calculation.

The integral in Eq.(4.12a) will have the form:

$$\begin{aligned} & \int_{F_1(\phi_{min})}^{F_2(\phi_{min})} \int_{\phi_{min}}^{F_1^{-1}(r)} E(r, \phi) dr d\phi + \int_{F_2(\phi_{min})}^{F_1(\phi_{max})} \int_{F_2^{-1}(r)}^{F_1^{-1}(r)} E(r, \phi) dr d\phi + \\ & \int_{F_1(\phi_{max})}^{F_2(\phi_{max})} \int_{F_2^{-1}(r)}^{\phi_{max}} E(r, \phi) dr d\phi \end{aligned}$$

After algebraic manipulations the resulting integral can be written as:

$$H_2 = \frac{R}{2\pi} \left[\begin{aligned} & \int_{F_1(\phi_{min})}^{F_1(\phi_{max})} e^{-jkr} [-\Psi_1(r)] dr + \int_{F_2(\phi_{min})}^{F_2(\phi_{max})} e^{-jkr} [\Psi_2(r)] dr + \\ & \int_{F_1(\phi_{max})}^{F_2(\phi_{max})} e^{-jkr} [\Psi_4(r)] dr \end{aligned} \right] \quad (4.26)$$

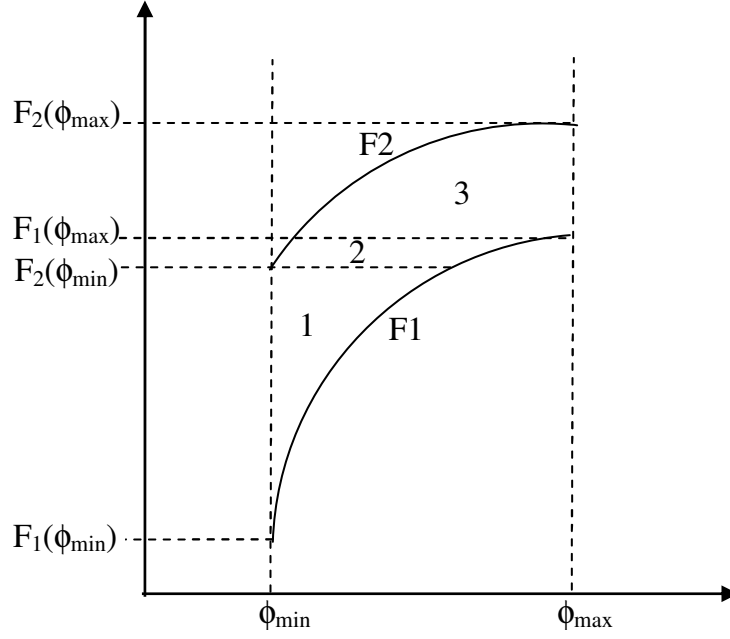


Figure 4.5: The limiting functions with monotonic increasing ϕ dependency.

where

$$\phi_{min} = \tan(\phi_p) \quad (4.27)$$

$$\phi_{max} = \arcsin(l/2R)$$

The $\Psi_3(r)$ integral vanishes in this interval.

4.3.2 Case 2: Region III, $\phi_t < \phi_p \leq \pi - \phi_t$

The equations we derived in the previous sections are originated from Eq.(4.17) where we have $1/\sqrt{c}$ or $1/\sqrt{r_p R \cos(\phi_p)}$ as a multiplication constant. Hence for a zero r_p or $\cos(\phi_p)$ value, the derived equations will no longer be valid. As discussed previously the first order approximation for $\cos(\phi)$ will be employed

in this region and the parameters that will be used for this case will be presented with:

$$M(\phi) \approx (r_p^2 + R^2 - 2r_p R \cos(\phi_p)) - (2r_p R \sin(\phi_p))\phi \quad (4.28a)$$

$$= a + b\phi$$

$$F_1(\phi) \approx \sqrt{a + b\phi + A_{zp}} \quad (4.28b)$$

$$F_2(\phi) \approx \sqrt{a + b\phi + B_{zp}} \quad (4.28c)$$

$$F_1^{-1}(r) = \frac{r^2 - a - A_{zp}}{b} \quad (4.28d)$$

$$F_2^{-1}(r) = \frac{r^2 - a - B_{zp}}{b} \quad (4.28e)$$

In this region, M and r are decreasing functions of ϕ . The algorithm introduced in the previous section can be applied to this case where we have:

$$\int_{\phi_{min}}^{\phi_{max}} \int_{F_1(\phi)}^{F_2(\phi)} E(r, \phi) dr d\phi = \quad (4.29)$$

$$\int_{F_1(\phi_{min})}^{F_2(\phi_{min})} \int_{\phi_{min}}^{F_2^{-1}(r)} E(r, \phi) dr d\phi + \int_{F_2(\phi_{max})}^{F_1(\phi_{min})} \int_{F_1^{-1}(r)}^{F_2^{-1}(r)} E(r, \phi) dr d\phi +$$

$$\int_{F_1(\phi_{max})}^{F_2(\phi_{max})} \int_{F_1^{-1}(r)}^{\phi_{max}} E(r, \phi) dr d\phi$$

Moreover for this region:

$$\int \frac{1}{\sqrt{r^2 - (a + b\phi)}} d\phi = \frac{2\sqrt{r^2 - (a + b\phi)}}{-b} \quad (4.30)$$

We calculate the integral in Eq.(4.29) with respect to ϕ and substitute the limits to obtain:

$$\begin{aligned}
 H = \frac{R}{\pi(-b)} \{ & \int_{F_1(\phi_{min})}^{F_2(\phi_{min})} e^{-jkr} [\sqrt{B_{zp}} - \sqrt{r^2 - (a + b\phi_{min})}] dr \\
 & + \int_{F_2(\phi_{max})}^{F_1(\phi_{min})} e^{-jkr} [\sqrt{B_{zp}} - \sqrt{A_{zp}}] dr \\
 & + \int_{F_1(\phi_{max})}^{F_2(\phi_{max})} e^{-jkr} [\sqrt{r^2 - (a + b\phi_{max})} - \sqrt{A_{zp}}] dr \}
 \end{aligned} \tag{4.31}$$

with the definition of:

$$\Psi_5(r) = \sqrt{r^2 - (a + b\phi_{min})} \tag{4.32a}$$

$$\Psi_6(r) = \sqrt{r^2 - (a + b\phi_{max})} \tag{4.32b}$$

the spatial transfer function can be expressed in a compact form as:

$$H = \frac{R}{\pi(-b)} \left[\begin{array}{cc} \int_{F_2(\phi_{max})}^{F_2(\phi_{min})} e^{-jkr} [\sqrt{B_{zp}}] dr & + \int_{F_1(\phi_{min})}^{F_2(\phi_{min})} e^{-jkr} [-\Psi_5(r)] dr \\ + \int_{F_1(\phi_{max})}^{F_2(\phi_{max})} e^{-jkr} [\Psi_6(r)] dr & + \int_{F_1(\phi_{max})}^{F_1(\phi_{min})} e^{-jkr} [-\sqrt{A_{zp}}] dr \end{array} \right] \tag{4.33}$$

where ϕ_{min} and ϕ_{max} are defined in Eq.(4.22).

4.3.3 Case 3: Regions IV and V ($\pi - \phi_t \leq \phi_p \leq \pi$)

The type of the integrals required to describe the transfer function of the points in Region IV and V can be calculated using the algorithm we introduced in Section 4.3.1. However, care must be taken since for these regions the integral of the quadratic form has a different expression than Eq.(4.17). For this part $\cos(\phi)$

will again be represented with the second order terms in series expansion [78] and $M(\phi)$, $F_1(\phi)$ and $F_2(\phi)$ have the same forms in Section 4.3.1 as:

$$M(\phi) \approx (r_p^2 + R^2 - 2r_p R \cos(\phi_p)) - (2r_p R \sin(\phi_p))\phi \quad (4.34a)$$

$$+ (r_p R \cos(\phi_p))\phi^2$$

$$= a + b\phi + c\phi^2 \quad (4.34b)$$

$$F_1(\phi) \approx \sqrt{a + b\phi + c\phi^2 + A_{zp}} \quad (4.34c)$$

$$F_2(\phi) \approx \sqrt{a + b\phi + c\phi^2 + B_{zp}} \quad (4.34d)$$

Region IV: $\tan\phi_p < \phi_{\min}$

In Region IV the limiting functions $F_1(\phi)$ and $F_2(\phi)$ are decreasing functions of ϕ and the inverses of the limits should be computed with Eq.(4.16a)-(4.16d).

For this case $\cos(\phi) < 0$ and the integral of Eq.(4.12a) is represented by [89]:

$$\int \frac{1}{\sqrt{r^2 - (a + b\phi + c\phi^2)}} d\phi = \frac{1}{\sqrt{-c}} \ln \left(2\sqrt{-c(r^2 - a - b\phi - c\phi^2)} - 2c\phi - b \right) = G(\phi) \quad (4.35)$$

To calculate the actual line integrals, we substitute $F_1^{-1}(r)$ and $F_2^{-1}(r)$ in Eq.(4.35) to obtain:

$$G(F_1^{-1}) = \Psi_7(r) = \frac{1}{\sqrt{-c}} \ln \left(2\sqrt{-cA_{zp}} + \sqrt{b^2 - 4c(a + A_{zp} - r^2)} \right) \quad (4.36a)$$

$$G(F_2^{-1}) = \Psi_8(r) = \frac{1}{\sqrt{-c}} \ln \left(2\sqrt{-cB_{zp}} + \sqrt{b^2 - 4c(a + B_{zp} - r^2)} \right) \quad (4.36b)$$

$$G(\phi_{\min}) = \Psi_9(r) = \frac{1}{\sqrt{-c}} \ln \left(2\sqrt{-c(r^2 - a - b\phi_{\min} - c\phi_{\min}^2)} - 2c\phi_{\min} - b \right) \quad (4.36c)$$

$$G(\phi_{max}) = \Psi_{10}(r) = \frac{1}{\sqrt{-c}} \ln \left(2\sqrt{-c(r^2 - a - b\phi_{max} - c\phi_{max}^2)} - 2c\phi_{max} - b \right) \quad (4.36d)$$

The resulting equation is given as:

$$H = \frac{R}{2\pi} \left[\begin{array}{cc} \int_{F_1(\phi_{max})}^{F_1(\phi_{min})} e^{-jkr} [-\Psi_7(r)] dr & + \int_{F_2(\phi_{max})}^{F_2(\phi_{min})} e^{-jkr} [\Psi_8(r)] dr + \\ \int_{F_1(\phi_{min})}^{F_2(\phi_{min})} e^{-jkr} [-\Psi_9(r)] dr & + \int_{F_1(\phi_{max})}^{F_2(\phi_{max})} e^{-jkr} [\Psi_{10}(r)] dr \end{array} \right] \quad (4.37)$$

where

$$\phi_{min} = -\arcsin(l/2R) \quad (4.38a)$$

$$\phi_{max} = \arcsin(l/2R) \quad (4.38b)$$

Region V: $\tan\phi_p \geq \phi_{min}$

When $\tan(\phi_p)$ is larger than the smallest value of ϕ the integral should be decomposed into two parts for proper calculation for the same reasons as in Section 4.3.1.

$$\int_{\phi_{min}}^{\phi_{max}} \int_{F_1(\phi)}^{F_2(\phi)} E(r, \phi) dr d\phi = H_1 + H_2 = \quad (4.39)$$

$$\int_{\phi_{min}}^{\tan(\phi_p)} \int_{F_1(\phi)}^{F_2(\phi)} E(r, \phi) dr d\phi + \int_{\tan(\phi_p)}^{\phi_{max}} \int_{F_1(\phi)}^{F_2(\phi)} E(r, \phi) dr d\phi$$

To find H_2 the same algorithm with the previous section will be used. The inverses of the functions are represented with the negative roots and the limits are decreasing functions of ϕ hence the resulting integral has the similar form

with the previous case and can be written as:

$$H_2 = \frac{R}{2\pi} \left[\begin{array}{cc} \int_{F_1(\phi_{max})}^{F_1(\phi_{min})} e^{-jkr} [-\Psi_7(r)] dr & + \int_{F_2(\phi_{max})}^{F_2(\phi_{min})} e^{-jkr} [\Psi_8(r)] dr + \\ \int_{F_1(\phi_{min})}^{F_2(\phi_{min})} e^{-jkr} [-\Psi_9(r)] dr & + \int_{F_1(\phi_{max})}^{F_2(\phi_{max})} e^{-jkr} [\Psi_{10}(r)] dr \end{array} \right] \quad (4.40)$$

where

$$\phi_{min} = -\tan(\phi_p) \quad (4.41a)$$

$$\phi_{max} = \arcsin(l/2R) \quad (4.41b)$$

To find H_1 we rewrite Eq.(4.12a) in terms of a , b , and c

$$H_1 = \int_{\phi_{min}}^{\tan(\phi_p)} \int_{F_1(\phi)}^{F_2(\phi)} \frac{e^{-jkr}}{\sqrt{r^2 - (a + b\phi + c\phi^2)}} dr d\phi \quad (4.42a)$$

and introduce a change of variable to write the integral in terms of the negative ϕ to ensure the non-negativity of the logarithm function:

$$\phi^* = -\phi \quad (4.42b)$$

$$H_1 = \int_{-\tan(\phi_p)}^{\phi_{max}} \int_{F_1(\phi^*)}^{F_2(\phi^*)} \frac{e^{-jkr}}{\sqrt{r^2 - (a - b\phi^* + c(\phi^*)^2)}} dr d\phi^* \quad (4.42c)$$

where

$$F_1^*(\phi^*) = \sqrt{(a - b\phi^* + c(\phi^*)^2) + A_{zp}} \quad (4.42d)$$

$$F_2^*(\phi^*) = \sqrt{(a - b\phi^* + c(\phi^*)^2) + B_{zp}} \quad (4.42e)$$

With this new variable definition $F_1^*(\phi)$ and $F_2^*(\phi)$ are decreasing functions of ϕ and Eq.(4.40) can be used to find the final expression. In this region $G(\phi^*)$ is

defined as:

$$G(\phi^*) = \frac{1}{\sqrt{-c}} \ln \left(2\sqrt{-c(r^2 - a + b\phi^* - c(\phi^*)^2)} - 2c\phi^* + b \right) \quad (4.43)$$

and $G(\phi_{min})$ and $G(\phi_{max})$ are expressed as:

$$G(\phi_{min}) = \Psi_{11}(r) = \frac{1}{\sqrt{-c}} \ln \left(2\sqrt{-c(r^2 - a + b\phi_{min} - c\phi_{min}^2)} - 2c\phi_{min} + b \right) \quad (4.44a)$$

$$G(\phi_{max}) = \Psi_{12}(r) = \frac{1}{\sqrt{-c}} \ln \left(2\sqrt{-c(r^2 - a + b\phi_{max} - c\phi_{max}^2)} - 2c\phi_{max} + b \right) \quad (4.44b)$$

The final form of H_1 is given as:

$$H_1 = \frac{R}{2\pi} \left[\begin{array}{cc} \int_{F_1^*(\phi_{max})}^{F_1^*(\phi_{min})} e^{-jkr} [-\Psi_7(r)] dr & + \int_{F_2^*(\phi_{max})}^{F_2^*(\phi_{min})} e^{-jkr} [\Psi_8(r)] dr + \\ \int_{F_1^*(\phi_{min})}^{F_2^*(\phi_{min})} e^{-jkr} [-\Psi_{11}(r)] dr & + \int_{F_1^*(\phi_{max})}^{F_2^*(\phi_{max})} e^{-jkr} [\Psi_{12}(r)] dr \end{array} \right] \quad (4.45)$$

where

$$\phi_{min} = -\tan(\phi_p) \quad (4.46a)$$

$$\phi_{max} = \arcsin(l/2R) \quad (4.46b)$$

The path that is followed to reduce the dimension of the integral in Eq.(4.12a) can be summarized as follows: First a region is chosen where r was a monotonic decreasing or increasing function of ϕ and change of order of integration was employed to obtain a solvable integral in terms of ϕ . The new integration limits are obtained and the integral is calculated with respect to ϕ which resulted with line integrals of non-linear functions of r . For the observation point on the z axis a different approach will be used as given below.

4.3.4 Case 4: On the z axis $r_p = 0$

For this case Eq.(4.12a) can be written as:

$$\frac{R}{2\pi} \int_{\phi_{min}}^{\phi_{max}} \int_{F_1}^{F_2} \frac{e^{-jkr}}{\sqrt{r^2 - M}} dr d\phi \quad (4.47)$$

where $M = R^2$ for $r_p = 0$. The integrand is independent of ϕ and Eq.(4.47) can be expressed as

$$\frac{R\phi_{max}}{\pi} \int_{F_1}^{F_2} \frac{e^{-jkr}}{\sqrt{r^2 - R^2}} dr \quad (4.48)$$

To remove the singularity caused by $F_1 = R$, we employ integration by parts and rewrite Eq.(4.48) as:

$$\frac{R\phi_{max}}{\pi} \left[e^{-jkr} \ln(r + \sqrt{r^2 - R^2}) \Big|_{F_1}^{F_2} - \int_{F_1}^{F_2} (-jk) e^{-jkr} \ln(r + \sqrt{r^2 - R^2}) dr \right] \quad (4.49)$$

4.3.5 Polynomial Approximation

The compact expressions for the spatial transfer function of the cylindrical radiator involve line integrals, some of which cannot be computed analytically. The integrals with the nonlinear functions of r can be evaluated using a numerical integration technique such as Gauss quadrature. The drawback of such a time consuming implementation is for each different frequency value a separate numerical integral routine must be used.

In this dissertation we introduced a faster approach. The above integrals are further simplified using Legendre polynomials. The kernels of the line integrals are expanded as truncated series of Legendre polynomials which could be integrated exactly term by term. The resulting spatial transfer function is

represented as summation of a few number of Bessel functions.

The normalized Legendre polynomials $\bar{P}_n(x)$ form a complete orthogonal system over the interval $[-1,1]$. Mathematically speaking:

$$\int_{-1}^1 \bar{P}_n(x) \bar{P}_m(x) dx = \delta_{mn} \quad (4.50)$$

where δ_{mn} is the Kronecker delta. Any function $f(x)$ defined in $[-1,1]$ interval may be expanded in terms of the normalized Legendre polynomials as:

$$f(x) = \sum_{n=0}^{n=\infty} a_n \bar{P}_n(x) \quad (4.51a)$$

and the coefficients a_n are obtained from:

$$a_n = \int_{-1}^1 \bar{P}_n(x) f(x) dx \quad (4.51b)$$

If the function is smooth and well behaved, it can be represented with a truncated series where the upper limit of Eq.(4.51a) is replaced with N .

Using the orthogonality of the Legendre polynomials, Bakhvalov and L .G. Vasil'eva [90] showed that if the zeros of the Legendre polynomials (i.e. nodes of the Gaussian-Legendre quadrature) are known, the coefficients of the truncated Legendre series can be found without the need of an integration routine. In other words Eq.(4.51b) can also be obtained from

$$a_n = \sum_{q=1}^{N+1} W_q \bar{P}_n(\lambda_q) f(\lambda_q) \quad (4.52)$$

where λ_q are the zeros of the Legendre polynomials and W_q are the weights of

the Legendre-Gaussian quadrature.

The application of this series expansion to our algorithm will be as follows. As a general representation, the integrals that we need to compute can be written as:

$$\int_a^b e^{-jkr} \Psi(r) dr = A e^{-jkB} \int_{-1}^1 e^{-jkAx} \Psi(Ax + B) dx \quad (4.53a)$$

with

$$r = Ax + B \quad (4.53b)$$

$$A = \frac{b - a}{2} \quad (4.53c)$$

$$B = \frac{b + a}{2} \quad (4.53d)$$

We expand $\Psi(Ax + B)$ in terms of the Legendre polynomials

$$\Psi(Ax + B) = \sum_{n=0}^{n=N} a_n \bar{P}_n(x) \quad (4.54a)$$

and use the identity [91],(Page 649):

$$\int_{-1}^1 e^{-jkx} \bar{P}_n(x) dx = \sqrt{4n+2} (j)^{-n} j_n(k) \quad (4.54b)$$

where $j_n(k)$ is the n^{th} order spherical Bessel function, to obtain:

$$\int_a^b e^{-jkr} \Psi(r) dr = A e^{-jkB} \sum_{n=0}^N a_n \sqrt{4n+2} (j)^{-n} j_n(Ak) \quad (4.54c)$$

The resulting summation, Eq.(4.54c), is valid for any wave number and can predict the acoustic fields in both attenuating and non-attenuating media.

4.4 Results

We carried out numerical and laboratory experiments to verify the method introduced in this chapter. Using the formulas given in Section 4.3, the spatial transfer function of the cylindrical transducer is calculated and compared with the results of a numerical integration routine which computes Eq.(4.7) without any approximations. The comparison results are validated with experimental measurements.

4.4.1 Numerical Integration

A number of direct numerical integration techniques were applied to compute Eq.(4.7). The Gauss-Legendre quadrature produced more accurate results in less time than the other standard integration techniques such as trapezoidal rule and Simpson's rule.

The 2D numerical routine can be summarized with the following equation:

$$H = \frac{R}{2\pi} \sum_{n=1}^N \sum_{u=1}^U w_n w_u \frac{e^{-jk\sqrt{M(\phi_n) + (z_p - z_u)^2}}}{\sqrt{M(\phi_n) + (z_p - z_u)^2}} \quad (4.55)$$

where ϕ_n and z_u denote the abscissas, and w_n w_u are the weights for ϕ and z respectively. The number of terms are determined according to the maximum frequency component of the signal. In this study 2π terms per minimum wavelength is found to be sufficient for an accurate integral result. The number of abscissas for z is computed by $U = \text{round}(\frac{2\pi f_{max} h}{c_o})$ and the number of abscissas for ϕ are: $N = \text{round}(\frac{2R\phi_{max} U}{h})$. The routine is implemented in Matlab R14 on a Pentium 4, 3GHz, 1GB RAM machine. The operating frequency of the transducer is 3.5MHz. To have a reasonable sized problem the maximum frequency

of the signals is limited to 10MHz. For the transducer used in this study $N=547$ and $U=21$.

4.4.2 Experimental Comparison

A wave propagation experiment was performed to validate the spatial transfer function formulation of the cylindrically concave transducer. For this experiment, a curved 1-D array transducer (Model 8665, BK Medical, Wilmigton, MA) consisting of 128 cylindrically curved elements was employed. The linear array operated at 3.5 MHz and each radiator element had 70.0 mm focal length with lateral dimensions $13 \text{ mm} \times 0.5 \text{ mm}$. The array was driven with the real time ultrasound scanner of Analogic Corporation (AN2300). In this study the wave propagation from a single element is measured. The array transducer was placed in a water tank ($0.8 \text{ m} \times 0.8 \text{ m} \times 1.5 \text{ m}$) that was filled with de-ionized de-gassed water at approximately 21°C . The single element radiator was operated in transmit mode using AN2300 where the system excited the transducer with a short excitation signal that approximated a delta function and the received echo was measured by a PVDF hydrophone with 0.1 mm radius. The data were recorded on a digital scope (LC 334a, LeCroy, Chestnut Ridge, NY) and transferred to a computer for later analysis. In this study, the wave propagation in a lossless medium -in water- was investigated.

A number of experiments were performed to evaluate the performance of our method. In this study, four comparison results are presented between measured and simulated data. Figures 4.6 to 4.9 compare three normalized waveforms: (a) the simulated response calculated with the method introduced in Section 4.3, SIM_1 , (b) the simulated response computed with the numerical approach in

Section 4.4.1 without any approximations, SIM₂, and, (c) real measured data in lossless medium. The error between the two simulated responses ((a) and (b)) and the speed improvement in computation time are the most important parameters to assess the performance of our method. The measures that will be used to compare these two results are defined as follows:

$$\text{Error}\% = 100 \frac{\|\text{SIM}_1 - \text{SIM}_2\|_2}{\|\text{SIM}_2\|_2} \quad (4.56a)$$

$$\text{Speed Improvement Ratio} = \frac{\text{Total time required to compute SIM}_1}{\text{Total time required to compute SIM}_2} \quad (4.56b)$$

To simulate the pressure fields, the density scaled electromechanical response of the transducer, $e_T(\omega)$, should be obtained. For this purpose, Eq.(4.4) is used with a simplified Wiener filter [59] and the Fourier transform of the measured data at the focal point ($p_f(\omega)$):

$$e_T(\omega) = \frac{p_f(\omega)H_f^*(\omega)}{|H_f(\omega)|^2 + q} \quad (4.57)$$

where $H_f(\omega)$ is the spatial transfer function at the focus, and q is the inverse of the signal to noise ratio, and it was chosen to be $0.01\max(|H_f(\omega)|^2)$ based on the data measured at the focus.

When calculating the frequency domain signals, it must be taken into account that H has an oscillatory behavior and has some abrupt changes in time domain. Equally sampled 512 frequency values between 0 to 10 MHz proved to be adequate to simulate the signals. The time domain signals were obtained by taking the inverse Fourier Transform of the signals acquired from Eq.(4.4). The real valued wave number used in these simulations was equal to ω/c_o , where

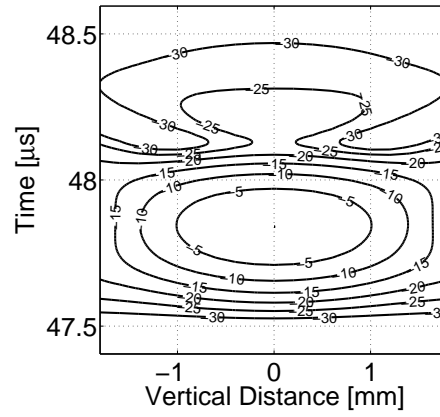
$c_o = 1500\text{m/s}$.

Figure 4.6 shows the acoustic field in Region III, on the y axis, for $z_p = -2$ mm. The measurements were obtained by scanning the PVDF hydrophone vertically and recording waveforms at 19 equally spaced locations between -1.8 mm to 1.8 mm. For this region, the error between two simulated responses ((a) and (b)) was found to be 0.07% and the speed improvement ratio 541. We have a very close agreement with the measured data (c) and the slight differences are attributable to the imperfections in the transducer as an ideal piston source, and the low SNR due to the use of a single isolated element.

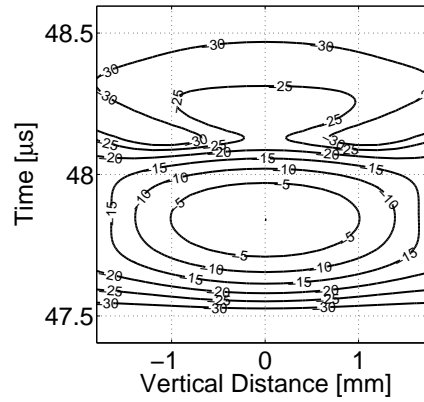
Figure 4.7 compares the propagation on the z axis. In this case, the PVDF hydrophone was scanned laterally and 14 equally spaced measurements recorded between -26 mm to 26 mm. The error between the two simulated responses was $7.5 \times 10^{-5}\%$ and the speed improvement ratio 1355. There was a very good agreement between the measured and the predicted data.

In Figure 4.8 we investigate the off-axis propagation in Region II where a similar scan with the previous case was performed. For this experiment the observation points were 6mm behind the focus and parallel to the z axis. 19 equally spaced measurements were observed between -36 mm to 36 mm. The error between two simulated responses and the speed improvement ratio were obtained as 0.02% and 145 respectively. The decrease in the speed ratio is due to the location of the observation points. This experiment shows the performance of the algorithm for the observation points where two separate line integrals should be calculated for ϕ dependency. There was again a very close agreement with the measured data.

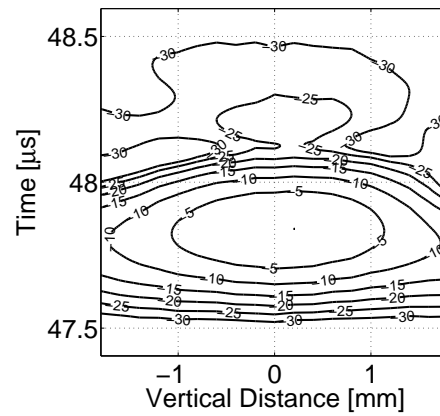
In Figure 4.9 the off-axis propagation in Regions I and II was investigated

Simulated Response $x=0\text{mm}$ $z=-2\text{mm}$ 5 dB lines

(a)

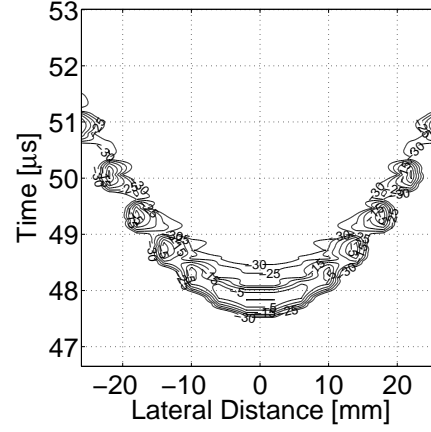
Simulated Response II $x=0\text{mm}$ $z=-2\text{mm}$ 5 dB lines

(b)

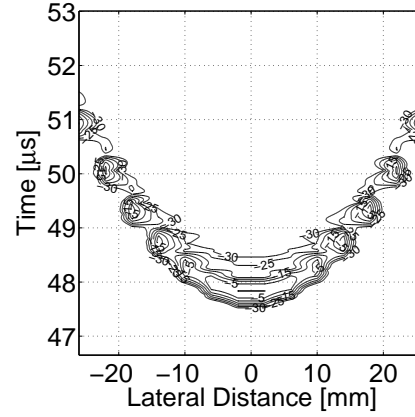
Measured Response $x=0\text{mm}$ $z=-2\text{mm}$ 5 dB lines

(c)

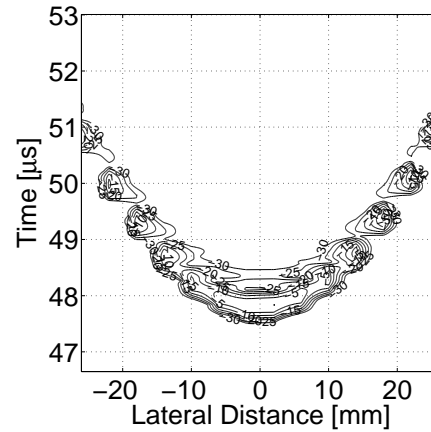
Figure 4.6: (a) Amplitude envelope of the simulated acoustic field on y axis using the equations derived in Section 4.3 (b) Amplitude envelope of the simulated acoustic field on y axis using Eq.(4.55) (c) Amplitude envelope of the measured ultrasound field of a 3.5 MHz transducer.

Simulated Response $x=0\text{mm}$ $y=0\text{mm}$ 5 dB lines

(a)

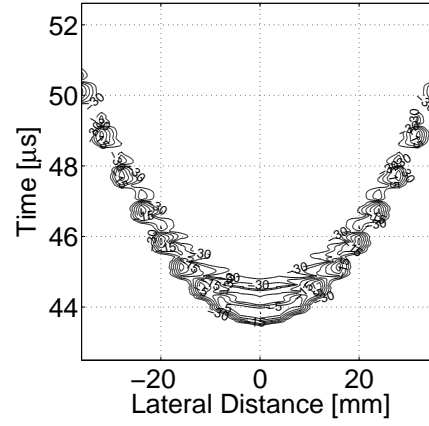
Simulated Response II $x=0\text{mm}$ $y=0\text{mm}$ 5 dB lines

(b)

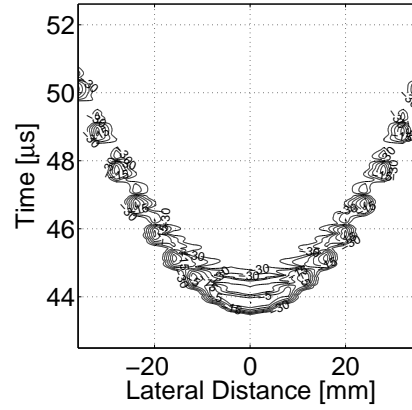
Measured Response $x=0\text{mm}$ $y=0\text{mm}$ 5 dB lines

(c)

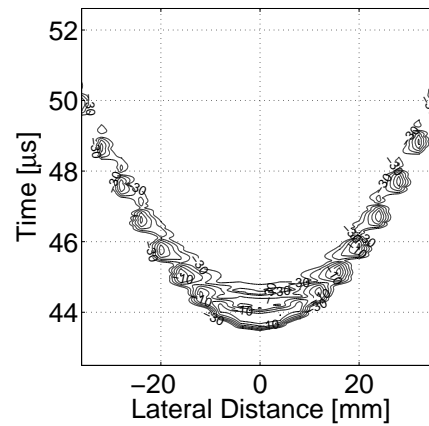
Figure 4.7: (a) Amplitude envelope of the simulated acoustic field on z axis using the equations derived in Section 4.3 (b) Amplitude envelope of the simulated acoustic field on z axis using Eq.(4.55) (c) Amplitude envelope of the measured ultrasound field of a 3.5 MHz transducer.

Simulated Response $x=6\text{mm}$ $y=0\text{mm}$ 5 dB lines

(a)

Simulated Response II $x=6\text{mm}$ $y=0\text{mm}$ 5 dB lines

(b)

Measured Response $x=6\text{mm}$ $y=0\text{mm}$ 5 dB lines

(c)

Figure 4.8: (a) Amplitude envelope of the simulated acoustic field on the $x - z$ plane using the equations derived in Section 4.3 (b) Amplitude envelope of the simulated acoustic field on the $x - z$ plane using Eq.(4.55) (c) Amplitude envelope of the measured ultrasound field of a 3.5 MHz transducer.

where the approximation for ϕ had the most significant effect on the results. For this experiment the observation points were 6 mm behind the focus and parallel to the y axis. 41 equally spaced measurements were observed between -4 mm to 4 mm. The error was found to be 0.12% and the speed improvement ratio 225 times. The effect of low SNR due to the use of single element can be visually observed from Fig. (4.9) (c). The measured data is expected to be symmetric around $y=0$.

4.4.3 Numerical Comparison

A numerical experiment was performed to assess the performance of our method in lossy media. The same experiment with Figure 4.9 was simulated with a complex wave number representing a power law attenuating medium. Specifically the parameters used in this simulation were (Section 3.5):

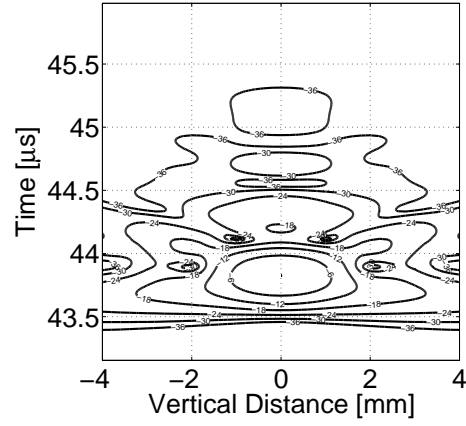
$$k^2(\omega) = \frac{\omega^2}{c_o^2} - j \frac{2\omega\alpha_b(\omega)}{c_o} \quad (4.58a)$$

where

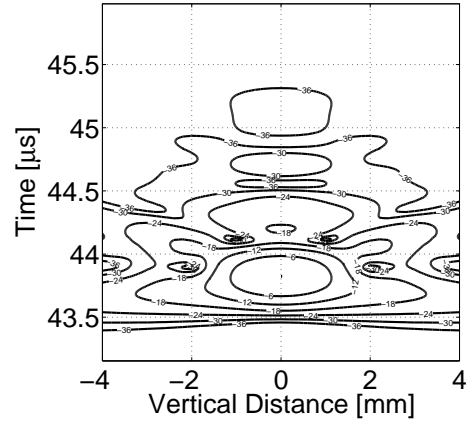
$$c_o = 1500\text{m/s} \quad (4.58b)$$

$$\alpha_b = 54\left(\frac{\omega}{\omega_o}\right)^{1.2}\text{Np/m} \quad (4.58c)$$

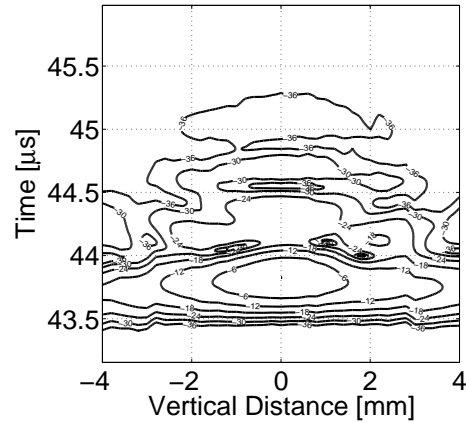
where ω_o is the mean frequency ($2\pi 3.5\text{MHz}$). The predicted responses obtained with two different methods are given in Fig. (4.10). We have an excellent agreement between two results. Quantitatively, the speed improvement ratio is obtained as 225 times and the error between two simulations is 0.08%. These comparisons confirm that the fast semi-analytical method we introduced in this

Simulated Response $x=6\text{mm}$ $z=0\text{mm}$ 6 dB lines

(a)

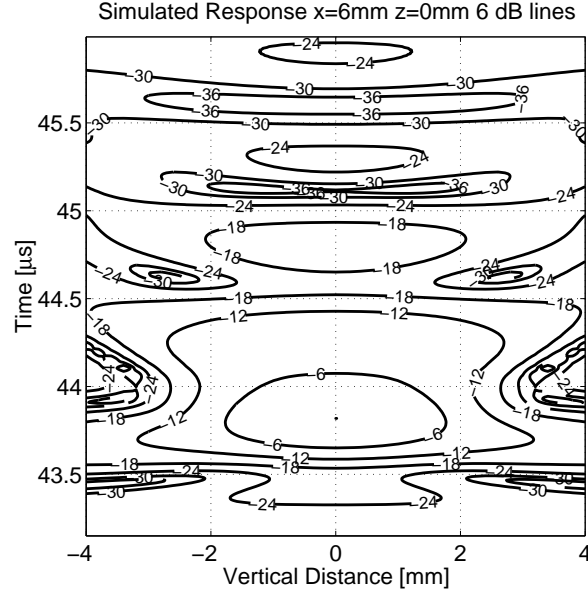
Simulated Response II $x=6\text{mm}$ $z=0\text{mm}$ 6 dB line

(b)

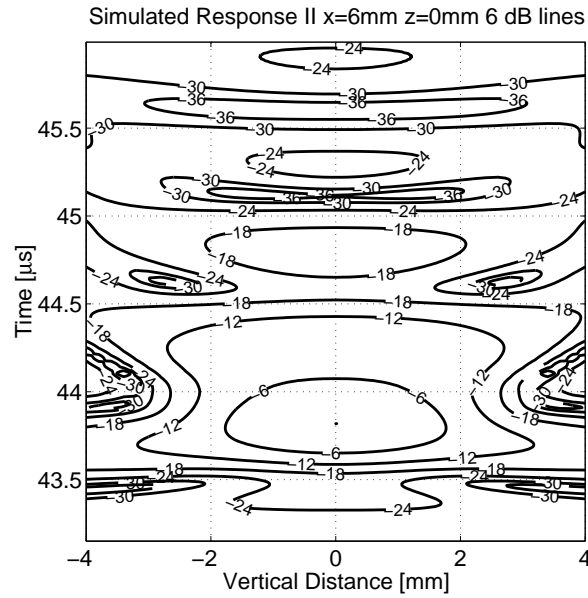
Measured Response $x=6\text{mm}$ $z=0\text{mm}$ 6 dB lines

(c)

Figure 4.9: (a) Amplitude envelope of the simulated acoustic field on the $x - y$ plane using the equations derived in Section 4.3 (b) Amplitude envelope of the simulated acoustic field on the $x - y$ plane using Eq.(4.55) (c) Amplitude envelope of the measured ultrasound field of a 3.5 MHz transducer.



(a)



(b)

Figure 4.10: (a) Amplitude envelope of the simulated acoustic field on the $x - y$ plane for lossy medium using the equations derived in Section 4.3 (b) Amplitude envelope of the simulated acoustic field for lossy medium on the $x - y$ plane using Eq.(4.55)

chapter can be used to predict the field of a cylindrically concave transducer for any physically realisable lossy homogenous medium.

4.5 Conclusion

In this study, we introduced a fast method to compute the spatial transfer function of cylindrically concave transducers in lossless and attenuating medium. For cylindrically focused transducers with low gain, we were able to use geometrical information to transform the 2D surface integral from an elliptic type to a parabolic type. The integrals could be evaluated by reducing the problem to a 1D line integral. The integrand was expressed as a truncated series of Legendre polynomials, from which it was possible to evaluate the line integral as a sum of spherical Bessel functions.

The form of the line integrals is such that the coefficients of the Legendre polynomials depend only on geometry and not on frequency. They only need to be calculated once and then the response at any frequency can be determined by a summation where the number of terms does not depend on frequency. This contrasts to direct integration approaches which need to employ finer discretization for higher frequency components.

The method was compared to an optimized numerical method which evaluated the surface integral directly. The speed of our algorithm depends on the number of the line integrals that need to be evaluated for an observation point. For the specific transducer that we used in our study, the speed improvement is between 40 and 1400 and the maximum error between two simulations was found to be 0.4%. Speed of evaluation is important because linear arrays employ 32 to 128 elements, each usually with a different phase and amplitude and potentially

individual waveforms. Hence, the advantage of the method will be revealed for array applications that requires the repeated computation of the time consuming numerical routines. Moreover, our semi-analytical frequency domain method can predict the spatial response of a cylindrical radiator in lossy medium simply by adding an imaginary component to the wave number.

In summary, we present a powerful semi-analytical method which complements the numerical approaches in the current literature. The approach can predict the acoustic field for a cylindrical concave transducer in attenuating homogeneous media. The approach can be applied to determine the fields in classical beam forming and also for applications such as tomography, that do not employ delay and sum beamforming. The application of this model to predict the acoustic properties of the HIFU lesions will be explained in the next chapter.

Shape Based Inversion

In the previous chapters, the forward problem of finding the field measurements from a given acoustic inhomogeneity of density, attenuation and sound speed is formulated. In this chapter, the inverse problem of reconstructing the perturbation parameters from field measurements will be analyzed and solved.

The motive behind the inversion problem -as explained previously in the introduction- is to develop and validate quantitative, fully three dimensional ultrasonic imaging methods to determine the spatial structure of the HIFU lesion. It has been reported that the treatment results in an ellipsoidal lesion in which the acoustic properties of the tissue, sound speed and attenuation, are significantly altered from their nominal values. An inversion method giving the quantitative information about the tissue properties can, in principle, be used to image the HIFU lesions. Complicating this approach is the fact that the computational size of the most of the relevant 3D problems makes traditional pixel based inversion methods impractical.

In this study we developed and implemented a shaped based inversion method to image the HIFU lesions. Rather than trying to reconstruct the thousands of

voxels defining the lesion, we concentrated on specifying the parameters describing the shape of the perturbation. We demonstrated that the shape based inversion method can be employed for ultrasound data. The proposed method is validated using simulated and measured broadband ultrasound backscatter data.

This chapter is organized as follows: The first section introduces the shape based inversion problem and describe the model and the formulae describing the boundary of the ellipsoidal perturbations. In Section 5.2, we give the mathematical details of the optimization routine and discuss the Jacobian calculation. In Section 5.3 we present the inversion results with simulated and measured backscattered data. The chapter is concluded in Section 5.4.

5.1 Mathematical Description and Background

5.1.1 Forward Model

To present the forward model, Eq.(3.24) from Chapter 3 is recalled in Eq.(5.1). By replacing k_s^2 with its mathematical equivalent, the scattered field can be described by:

$$\begin{aligned}
 p_s(r, \omega) = & - \int_{V'} c_p(r') G(r, r', \omega) \left[\frac{2\omega^2}{c_b^3} \right] p_b(r', \omega) d^3 r' \\
 & - \int_{V'} \alpha_p(r, \omega) G(r, r', \omega) \left[j \frac{2\omega}{c_b} \right] p_b(r', \omega) d^3 r' \\
 & + \int_{V'} \sigma_p(r') \nabla p_b(r', \omega) \cdot \nabla G(r, r', \omega) d^3 r'
 \end{aligned} \tag{5.1}$$

This equation can be written in a more compact form

$$p_s(r, \omega) = \int_{V'} K_1(r, r', \omega) c_p(r') d^3 r' + \int_{V'} K_2(r, r', \omega) \alpha_p(r') d^3 r' + \int_{V'} K_3(r, r', \omega) \sigma_p(r') d^3 r' \quad (5.2)$$

where K_i , $i = 1, 2, 3$ depend only on the background properties. To represent the forward model in terms of the experimental measurements Eq.(3.32) from Chapter 3 will be used to obtain K_i .

For the imaging system of interest in this work we assume we have multiple transmitters and receivers. For the case of N_T transmitters and N_R receivers with N_S frequency samples the measured data (\mathbf{y}) can be written as a column vector of size $N_T \times N_S \times N_R$. Discretizing Eq.(5.2) at any position r' , the scattered field can be written in a matrix-vector model of the form:

$$\mathbf{y} = \begin{bmatrix} \mathbf{K}_1 & \mathbf{K}_2 & \mathbf{K}_3 \end{bmatrix} \begin{bmatrix} \mathbf{f}_1 \\ \mathbf{f}_2 \\ \mathbf{f}_3 \end{bmatrix} + \mathbf{n} = \mathbf{K}\mathbf{f} + \mathbf{n} \quad (5.3)$$

where

- \mathbf{K} is the matrix representation of the integral
- \mathbf{f}_1 is the column vector containing the voxel values of sound speed perturbation, c_p
- \mathbf{f}_2 is the column vector containing the voxel values of attenuation perturbation, α_p

- \mathbf{f}_3 is the column vector containing the voxel values of density perturbation, σ_p
- \mathbf{n} is the additive sensor noise.

The ultimate goal is to restore the unknown medium parameters from measured backscatter data. The traditional approach to this problem is to use linear inversion methods, and try to reconstruct the voxelated versions of the sound speed, density and absorption images. As discussed previously in the introduction chapter, the nominal wavelength of the acoustic field in tissue is about 0.3mm and the physical size of the region that we want to image is about 30mm which implies an accurate discretization of the problem, 0.1 wavelengths, requires a billion of voxels. The linear inversion problem is very ill-posed for this case due to the enormous number of voxels defining each of the three unknown vectors \mathbf{f}_1 , \mathbf{f}_2 , \mathbf{f}_3 .

Our approach to the problem is based on the specification of the parameters describing the shape of the perturbations. We assume the shape of the perturbations are known to be ellipsoids but the locations, sizes and orientations are unknown. Specifically, the perturbations in Eq.(5.2), c_p , α_p , and σ_p , are represented by ellipsoidal shapes.

To completely characterize the perturbation in one variable, we only need the location of the center (x_o , y_o , z_o), the lengths of the three axes of the ellipsoid (l_1 , l_2 , l_3), three angles (θ_1 , θ_2 , θ_3) that orient the ellipsoid in space and (M) contrast of the perturbation. Thus rather than the billion of voxels defining each of the three unknown vectors, we have only $3 \times 10=30$ quantities to estimate from the measured data. This approach is nonlinear but better posed.

5.1.2 Ellipsoid Modeling

Exact Model of the Ellipsoid

In mathematical notation a perturbation ellipsoid can be defined with four elements:

- A length-3 vector, c , denoting the center of the ellipsoid, (x_o, y_o, z_o) .
- A diagonal matrix $D = \text{Diag}(d)$ whose diagonal entries are the one over the lengths of the semi-axes, (l_1, l_2, l_3) .
- An orthonormal matrix U whose three columns are the coordinates of the semi-axes defined in term of the Euler angles, $(\theta_1, \theta_2, \theta_3)$.
- A constant M , defining the contrast of the object.

We begin by defining c , D , U :

$$c = \begin{bmatrix} x_o \\ y_o \\ z_o \end{bmatrix} \quad (5.4)$$

$$D = \begin{bmatrix} 1/l_1 & 0 & 0 \\ 0 & 1/l_2 & 0 \\ 0 & 0 & 1/l_3 \end{bmatrix} \quad (5.5)$$

$$U = U_1(\theta_1)U_2(\theta_2)U_3(\theta_3) \quad (5.6a)$$

$$U = \begin{bmatrix} \cos(\theta_1) & \sin(\theta_1) & 0 \\ -\sin(\theta_1) & \cos(\theta_1) & 0 \\ 0 & 0 & 1 \end{bmatrix} \begin{bmatrix} \cos(\theta_2) & 0 & \sin(\theta_2) \\ 0 & 1 & 0 \\ -\sin(\theta_2) & 0 & \cos(\theta_2) \end{bmatrix} \begin{bmatrix} \cos(\theta_3) & \sin(\theta_3) & 0 \\ -\sin(\theta_3) & \cos(\theta_3) & 0 \\ 0 & 0 & 1 \end{bmatrix} \quad (5.6b)$$

A point $r' = [x', y', z']^T$ is determined to be on or in the ellipsoid if

$$\|DU^T(r' - c)\|_2^2 \leq 1 \quad (5.7)$$

There are multiple ways to define the rotation matrix from Euler angles [92]. However, it has been reported that the representation of the U makes little difference on the performance of the algorithm [56]. The representation type we used here is referred as the "x-convention" [56].

Having described the boundary of the anomaly, we define a support function $S(r')$ which has value (1) on the ellipsoid and (0) outside. Mathematically $S(r')$ will be represented as

$$S(r') = \begin{cases} 1 & r' \in \text{ellipsoid} \\ 0 & \text{otherwise} \end{cases} \quad (5.8)$$

Using the ellipsoid representation given above, we can use Eq.(5.7) to determine if the centers of the voxels in the region of interest lies in or on the ellipsoid. If the observation point is within the ellipsoid, $S(r')$ will be assigned to 1. By means of this support function the perturbations will be defined as:

$$\gamma(r') = MS(r') \quad (5.9)$$

The support function that we chose to represent the anomalies, $S(r')$, is a step function which gives discontinuity at the boundary of the ellipsoid. For the performance of the optimization routine we should have a smooth approximation for the boundary. Specifically, the key to any non-linear minimization technique is to specify the Jacobian of the objective function with respect to the unknown parameters. With such a representation, the Jacobian of the function should be computed numerically which would increase the overall computation time of the optimization routine. To obtain an analytical representation of the Jacobian we should have a differentiable expression that maps the parameters describing the shape to any point r' in the region of interest.

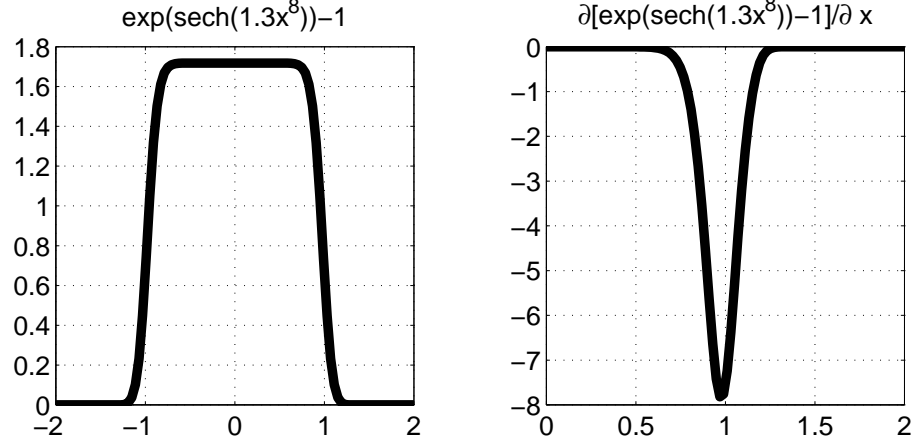
To improve the performance of the optimization routine that will be used in this study, we introduced a filter like decision function which approximates a step function. Specifically, the decision function takes $\|DU^T(r' - c)\|_2^2$ as the argument, produces zero output for the input values slightly larger than one and provides a smooth transition from 1 to 0 at the boundary. The type of the function used in this study will be introduced in the next section.

Approximate Model of the Ellipsoid: Sech

In this section we will introduce a differentiable expression to describe the boundary of the ellipsoid. Specifically such an expression, which will be named as decision function from now on, should satisfy these three properties:

The decision function

1. should be a function of r' and ellipsoid parameters,
2. should have value 1 on and inside of the ellipsoid and 0 outside,

Figure 5.1: Decision function $A(x)$ and its derivative

3. should provide smooth transition from 1 to 0 at the boundary for differentiability.

There are a number of functions which satisfies these properties. In this study a function of **sech** is chosen as the decision function for the reasons that will be explained below. We define the decision function, $A(x)$, and the perturbations as:

$$A(x) = \exp(\text{sech}(1.3x^8)) - 1 \quad (5.10a)$$

$$\gamma(r') = \exp(\tilde{M}\text{sech}(1.3\|DU^T(r' - c)\|_2^{16})) - 1 \quad (5.10b)$$

The decision function $A(x)$, Eq.(5.10a), and its derivative are given in Fig. (5.1). The function $A(x)$, approximates a box and its derivative estimates an impulse function. **sech**(**1.3x⁸**) is the main component of the decision function that characterizes the shape of the box in Fig. (5.1). The coefficient 1.3 is chosen so that without the scaling from the exponential function, the boundary value of

the shape is set to 0.5 (the mean value of the change in the boundary). The exponent of x defines the slope of the change in the boundary. Ideally, any even number larger than 4 gives a good approximation of a box but on the other hand the sharp change in the derivative limits the exponent value to 8.

Equation (5.10b) is the function that will be used to represent the perturbations in Eq.(5.2). As explained above, the $\text{sech}(1.3\|DU^T(r' - c)\|_2^{16})$ term characterizes the shape of the lesion and \tilde{M} defines the change in the magnitude of the acoustic parameter with respect to the background. Here we should explain Eq.(5.10b) in detail. We will first explain the decision behavior and then the contrast value, \tilde{M} .

As it is given in Eq.(5.7), if a point r_1 is within the ellipsoid, $\|DU^T(r_1 - c)\|_2^2$ is smaller than 1 and the value of $\gamma(r_1)$ is equal to a constant value ($\exp(\tilde{M}) - 1$). On the other hand, if r_1 is not within the ellipsoid, the value of Eq.(5.7) is larger than 1 and $\gamma(r_1) = 0$. Around the boundary, the function provides a transition from 1 to 0. Therefore the expression behaves like a decision function, and classifies the points in the region of interest.

For our inversion problems we assume a uniform contrast for the acoustic parameters. Therefore the value of γ on the ellipsoid should be equal to the physical value of the acoustic parameter it represents. Due to the exponential term in the definition of γ , \tilde{M} is not equal to the actual value of the perturbation but to the natural logarithm of the contrast value. Mathematically,

$$\tilde{M} = \ln(M + 1) \quad (5.11)$$

where M is the actual contrast. e.g. for a sound speed perturbation of $M = 20$ m/s, the value that will be used in γ is $\tilde{M} = \ln(20 + 1)$ and equals to 3.05.

Equation 5.10b is also visualized in 3D in Fig. (5.2). The real and the approximated ellipsoids are plotted in Fig. (5.2) where the expected shapes are drawn with the black lines. As predicted from Fig. (5.1), the contrasts of the estimated ellipsoids gradually decay to zero and the decision function successfully models the ellipsoids.

5.1.3 Final Problem Statement

The parameters that will be used to characterize the ellipsoids of the three acoustic properties will be

$$\beta_i = [x_{oi}, y_{oi}, z_{oi}, l_{1i}, l_{2i}, l_{3i}, \theta_{1i}, \theta_{2i}, \theta_{3i}, M_i]$$

where the subscripts $i = c, a, d$ will be used to represent the perturbations in sound speed, attenuation and density respectively. The representation of the perturbations given in Eq.(5.10b), $\gamma(r')$, will be replaced by $\gamma_i(r', \beta_i)$ to account for the parameters of each individual ellipsoid. Mathematically speaking,

$$\gamma_i(r', \beta_i) = \exp(\tilde{M}_i \text{sech}(1.3 \|D_i U_i^T(r' - c_i)\|_2^{16})) - 1 \quad (5.12a)$$

e.g. the perturbation for the attenuation to be used in Eq.(5.2)

$$\alpha_p(r') = \gamma_a(r', \beta_a) = \exp(\tilde{M}_a \text{sech}(1.3 \|D_a U_a^T(r' - c_a)\|_2^{16})) - 1 \quad (5.12b)$$

The problem we should be solving given data \mathbf{y} is the non-linear least squares problem:

$$\min_{\beta_c, \beta_a, \beta_d} \|\mathbf{y} - \mathbf{Kf}(\beta)\|_2^2 \quad (5.13a)$$

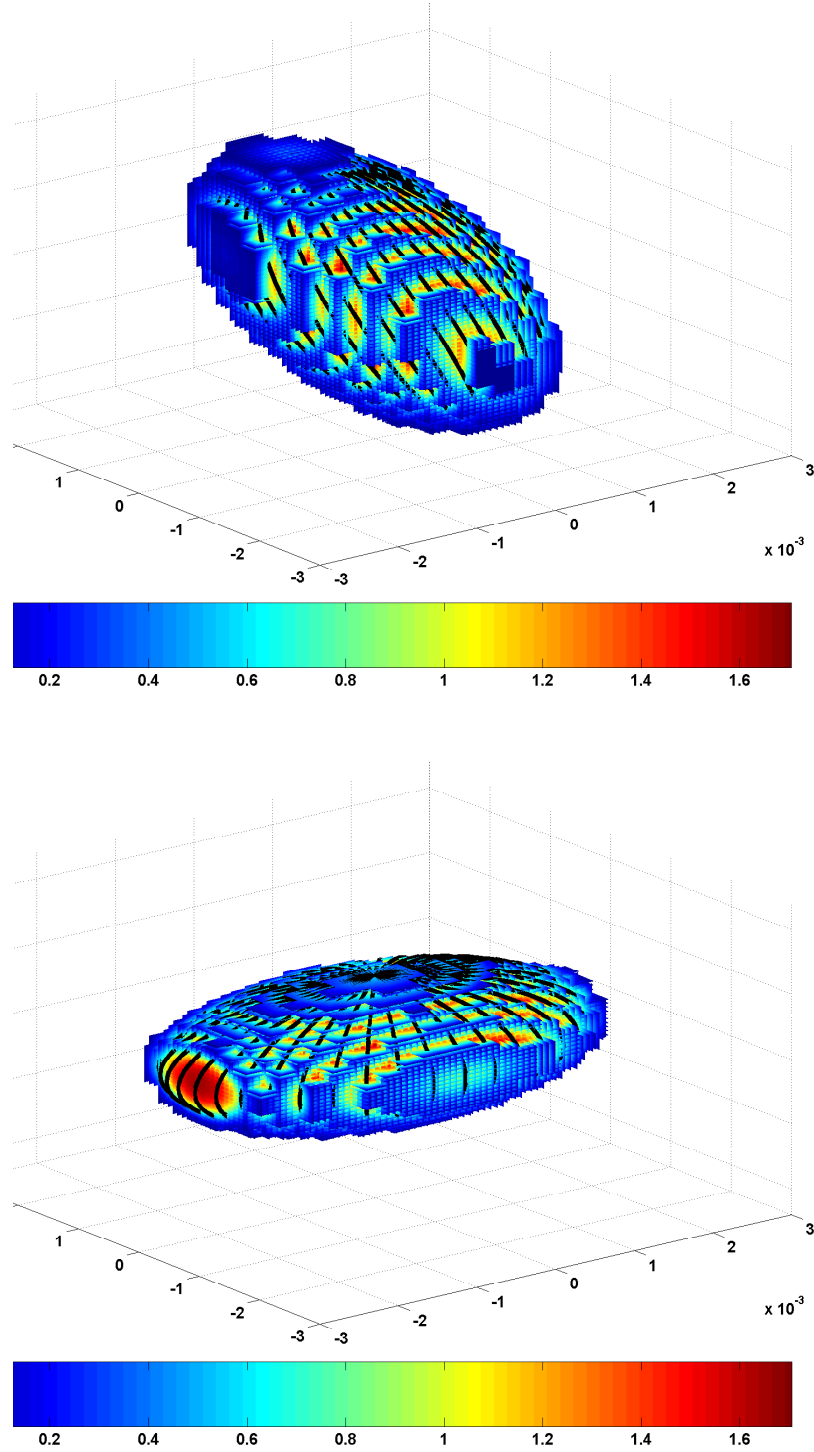


Figure 5.2: The expected shapes are drawn with black lines on top of the approximated ellipsoids. The contrasts of the ellipsoids are shown with the color scales. As predicted from Fig. (5.1) the contrast values gradually decay to zero.

$$\beta = \begin{bmatrix} \beta_c \\ \beta_a \\ \beta_d \end{bmatrix} \quad (5.13b)$$

5.2 Inversion Approach

We propose to solve the minimization problem in Eq.(5.13a) using Gauss-Newton method [93]. For this purpose, we first provide an initial guess for the ellipsoid parameters (β^0). Subsequent guesses (β^k) for the parameter vectors are then produced by the recurrence relation:

$$\beta^{k+1} = \beta^k + \alpha^k t^k, \quad 0 \leq k \leq k_{max} \quad (5.14)$$

where α^k is the sense optimal, k_{max} is the maximum number of iterations and t^k is the search direction and obtained from the solution of:

$$(J^T J)t^k = -J^T \|\mathbf{y} - \mathbf{K}\mathbf{f}(\beta^k)\|_2 \quad (5.15)$$

Here J is the Jacobian and T is the transpose operator.

Jacobian Calculation

The Jacobian matrix will be obtained from the matrix multiplication defined in Eq.(5.3).

$$\frac{\partial y}{\partial \mu} = - \begin{bmatrix} \mathbf{K}_1 & \mathbf{K}_2 & \mathbf{K}_3 \end{bmatrix} \begin{bmatrix} \frac{\partial \mathbf{f}_1}{\partial \mu} \\ \frac{\partial \mathbf{f}_2}{\partial \mu} \\ \frac{\partial \mathbf{f}_3}{\partial \mu} \end{bmatrix} \quad (5.16)$$

where μ is the unknown geometric parameter of the ellipsoid and as discussed before, \mathbf{f}_i s are the column vectors containing the voxel values of the perturbations. To obtain Jacobian matrix, the derivatives of Eq.(5.12a) with respect to the unknown ellipsoid parameters should be obtained. The mathematical details are explained below.

Using the chain rule:

$$\frac{\partial \gamma_i(r', \beta_i)}{\partial \mu} = -10.4 \tilde{M}_i \text{sech}(1.3x^8) \tanh(1.3x^8) x^7 \exp(\tilde{M}_i \text{sech}(1.3x^8)) \frac{\partial x}{\partial \mu} \quad (5.17a)$$

$$\frac{\partial \gamma_i(r', \beta_i)}{\partial M_i} = \text{sech}(1.3x^8) \exp(\tilde{M}_i \text{sech}(1.3x^8)) \quad (5.17b)$$

where $x = ||D_i U_i^T (r - c_i)||_2^2$. Using matrix algebra x can be written as:

$$x = (r' - c_i)^T U_i D_i^T D_i U_i^T (r' - c_i)$$

The derivative of x with respect to the ellipsoid parameters can be obtained with matrix calculus.

$$\frac{\partial x}{\partial x_{oi}, y_{oi}, z_{oi}} = 2 \frac{\partial (r' - c_i)^T}{\partial x_{oi}, y_{oi}, z_{oi}} U_i D_i^T D_i U_i^T (r' - c_i) \quad (5.18a)$$

where

$$\frac{\partial (r' - c_i)}{\partial x_{oi}} = \begin{bmatrix} -1 \\ 0 \\ 0 \end{bmatrix} \quad \frac{\partial (r' - c_i)}{\partial y_{oi}} = \begin{bmatrix} 0 \\ -1 \\ 0 \end{bmatrix} \quad \frac{\partial (r' - c_i)}{\partial z_{oi}} = \begin{bmatrix} 0 \\ 0 \\ -1 \end{bmatrix} \quad (5.18b)$$

$$\frac{\partial x}{\partial l_{1i}, l_{2i}, l_{3i}} = 2 (r' - c_i)^T U_i D_i^T \frac{\partial D_i}{\partial l_{1i}, l_{2i}, l_{3i}} U_i^T (r' - c_i) \quad (5.19a)$$

where

$$\frac{\partial D_i}{\partial l_{1i}} = \begin{bmatrix} -1/l_{1i}^2 & 0 & 0 \\ 0 & 0 & 0 \\ 0 & 0 & 0 \end{bmatrix} \quad \frac{\partial D_i}{\partial l_{2i}} = \begin{bmatrix} 0 & 0 & 0 \\ 0 & -1/l_{2i}^2 & 0 \\ 0 & 0 & 0 \end{bmatrix} \quad \frac{\partial D_i}{\partial l_{3i}} = \begin{bmatrix} 0 & 0 & 0 \\ 0 & 0 & 0 \\ 0 & 0 & -1/l_{3i}^2 \end{bmatrix} \quad (5.19b)$$

$$\frac{\partial x}{\partial \theta_{1i}, \theta_{2i}, \theta_{3i}} = 2(r' - c_i)^T \frac{\partial U_i}{\partial \theta_{1i}, \theta_{2i}, \theta_{3i}} D_i^T D_i U_i^T (r' - c_i) \quad (5.20a)$$

where

$$\frac{\partial U_i}{\partial \theta_{1i}} = \begin{bmatrix} -\sin(\theta_{1i}) & \cos(\theta_{1i}) & 0 \\ -\cos(\theta_{1i}) & -\sin(\theta_{1i}) & 0 \\ 0 & 0 & 0 \end{bmatrix} U_{2i} U_{3i} \quad (5.20b)$$

$$\frac{\partial U_i}{\partial \theta_{2i}} = U_{1i} \begin{bmatrix} -\sin(\theta_{2i}) & 0 & \cos(\theta_{2i}) \\ 0 & 0 & 0 \\ -\cos(\theta_{2i}) & 0 & -\sin(\theta_{2i}) \end{bmatrix} U_{3i} \quad (5.20c)$$

$$\frac{\partial U_i}{\partial \theta_{3i}} = U_{1i} U_{2i} \begin{bmatrix} -\sin(\theta_{3i}) & \cos(\theta_{3i}) & 0 \\ -\cos(\theta_{3i}) & -\sin(\theta_{3i}) & 0 \\ 0 & 0 & 0 \end{bmatrix} \quad (5.20d)$$

5.3 Inversion Examples and Results

In this section we will present the 3D shape based inversion results for HIFU lesion imaging. Using the model given in Eq.(5.1) and Eq.(5.12a) we estimate the structure and the contrast of the ellipsoidal shaped perturbations in sound speed, attenuation and density. The proposed method will be validated using simulated and measured ultrasound backscatter data.

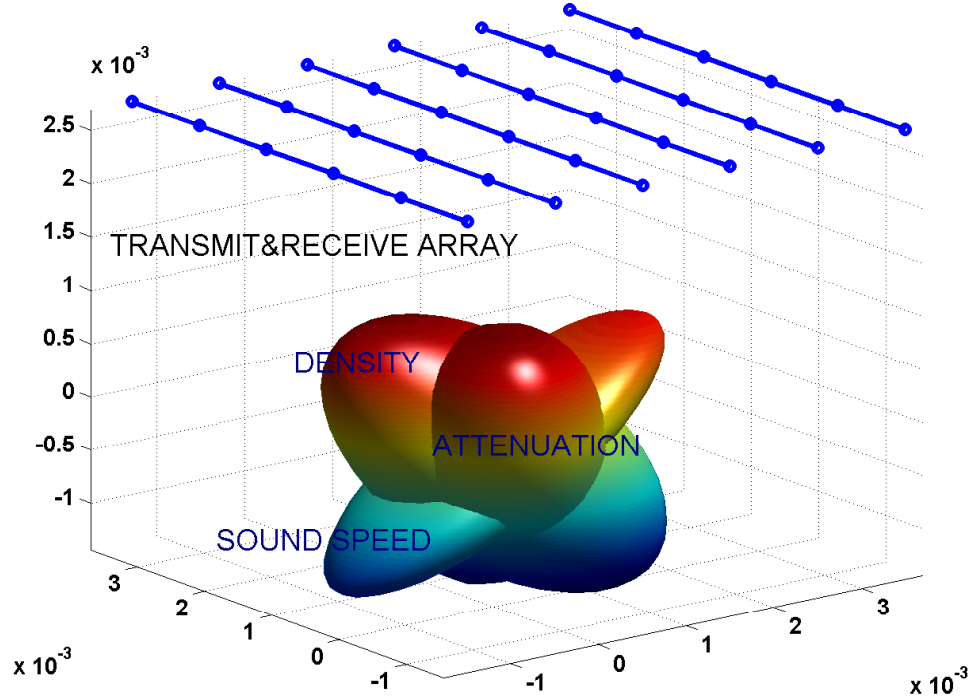


Figure 5.3: Experimental Setup

5.3.1 Numerical Experiments and Results

The numerical experiment conditions are given in Fig. (5.3). A linear array of six point sources are scanned across the anomaly at six different measurement points. At each stop, a single transmitter emits data into the medium where the interaction, backscatter data, is measured by the six elements of the array. Six frequencies equally sampled between 300kHz-425kHz are used in the experiment. A Gaussian noise was added to the data to set the signal to noise ratio to 25dB. To reduce the computation size, we used frequency values lower than those that are used in the medical imaging applications and the overall size of the problem is reduced to $(5 \text{ mm} \times 5 \text{ mm} \times 5 \text{ mm})$ which is smaller than what we would have in practice. On the other hand, to have a realistic approach to

the problem, we used the tissue mimicking dispersive model from Chapter 3 to represent the background. The parameters used in the simulations are: $c_b = 1551\text{m/s}$, $\rho_b = 1045\text{kg/m}^3$, $\alpha_b = 3.6(\omega/\omega_o)^{1.2}$ where $\omega_o = 2\pi 350\text{kHz}$. The values of the contrasts for a realistic problem are chosen as explained below. Total number of voxels in the region of interest is 4096 ($16 \times 16 \times 16$).

It has been confirmed with many publications that, the heating of tissue affects both sound speed and attenuation [38–43]. The change in sound speed is less than 20m/s about (1%) and in most cases reported to be reversible. The attenuation coefficient has been measured to increase dramatically with values ranging from 80%-700% which is still in the Born approximation range. More precisely, for the Born approximation to be valid, the constraint on the attenuation is defined as the smallness of α_p/k_b . Mathematically, as previously discussed in Chapter 3, the nominal attenuation in human tissue is 35.6 Np/m at 3.5 MHz. For the nominal sound speed of 1551 m/s and 700% perturbation in attenuation, the ratio of α_p/k_b is 17×10^{-3} . The change in the density is limited to 1% to validate the Born model of Chapter 3. Thus the bounds for the contrasts, M_i , are chosen as:

- $0 \text{ m/s} < M_c < 20 \text{ m/s}$
- $0 \text{ Np/m} < M_a < 20 \text{ Np/m}$
- $0 \text{ kg/m}^3 < \sigma_p < 10 \text{ kg/m}^3$, hence $0 < M_d < 9.5 \times 10^{-3}$

The inversion method described in Section 5.2 is implemented in Matlab where the "lsqnonlin" function with Gauss-Newton option is used. The geometric parameters and the contrasts of the ellipsoids, β_i , are scaled to the same order

Table 5.1: Lower and upper limits for the geometric parameters of the ellipsoid

	Lower Limit	Upper Limit
x_o	-2.5 mm	2.5 mm
y_o	-2.5 mm	2.5 mm
z_o	-2.5 mm	2.5 mm
l_1	5×10^{-4}	2.5 mm
l_2	5×10^{-4}	2.5 mm
l_3	5×10^{-4}	2.5 mm
θ_1	0	2π
θ_2	0	π
θ_3	0	2π

(between 1 and 2) prior to the optimization routine to maximize the performance. The bounds for the geometric parameters are given in Table 5.1. The lower limits for the lengths of the semi axes is set to small number (different than 0) for proper solution. We set the lower and the upper bounds for the "lsqnonlin" function to 1 and 2 respectively to ensure that the boundary of the ellipsoid is in the region of interest and the contrasts are within the above defined limits. Physically, in case of HIFU experiments we have prior knowledge of the rough location and the approximate contrasts of the HIFU lesion. We basically use this prior information and limit our search around the HIFU region.

A number of experiments are performed to assess the performance of the inversion algorithm and to explore its ability to reconstruct the HIFU lesions. In Fig. (5.4)-Fig. (5.6) we display the true ellipsoid distributions, the initial guesses provided to our estimation method and the final result. For comparison purposes, the true shapes are plotted with blue lines on the estimated ellipsoids. Two measures are introduced to describe the error between real and simulated

Table 5.2: Contrast and error values for the sound speed, attenuation and density

		Real	Initial	Estimate	Err _c	Err _v
Case 1	Sound (m/s)	3.58	20.00	3.71	3.59	3.00
	Density (kg/m ³)	4.99	10.00	4.87	2.32	2.05
	Attenuation (Np/m)	3.58	20.00	3.63	1.20	2.69
Case 2	Sound (m/s)	7.42	20.00	7.50	0.95	3.19
	Density (kg/m ³)	9.01	10.00	8.93	0.87	5.73
	Attenuation (Np/m)	7.42	20.00	8.16	9.88	2.26
Case 3	Sound (m/s)	13.57	20.00	10.52	22.01	32.94
	Density (kg/m ³)	10.00	10.00	10.00	0	1.41
	Attenuation (Np/m)	12.30	19.00	5.92	51.01	1.89

ellipsoids. The estimation error in contrast is defined as:

$$\text{Percentage error in contrast} = \text{Err}_c = 100 \left| \frac{M_i - \overline{M}_i}{M_i} \right| \quad (5.21)$$

where M_i and \overline{M}_i represent the actual and estimated contrasts respectively. The volumetric estimation error is defined as:

$$\text{Percentage volumetric error} = \text{Err}_v = 100 \left(1 - \frac{\text{Volume}(E_a \cap E_e)}{\text{Volume}(E_a \cup E_e)} \right) \quad (5.22)$$

where E_a and E_e represent the actual and estimated ellipsoids respectively.

For comparison purposes, the real, initial and estimated contrast values for all the experiments are given in Table 5.2 with the error values.

In Figure 5.4 we have similarly sized and shaped ellipsoids with different orientations. Given little prior information about the shape and the contrasts we were able to recover the geometry and the contrasts quite accurately. The results presented in in this section is is implemented with on a 1GHz Linux workstation. The number of iterations required is 99 and the total computation

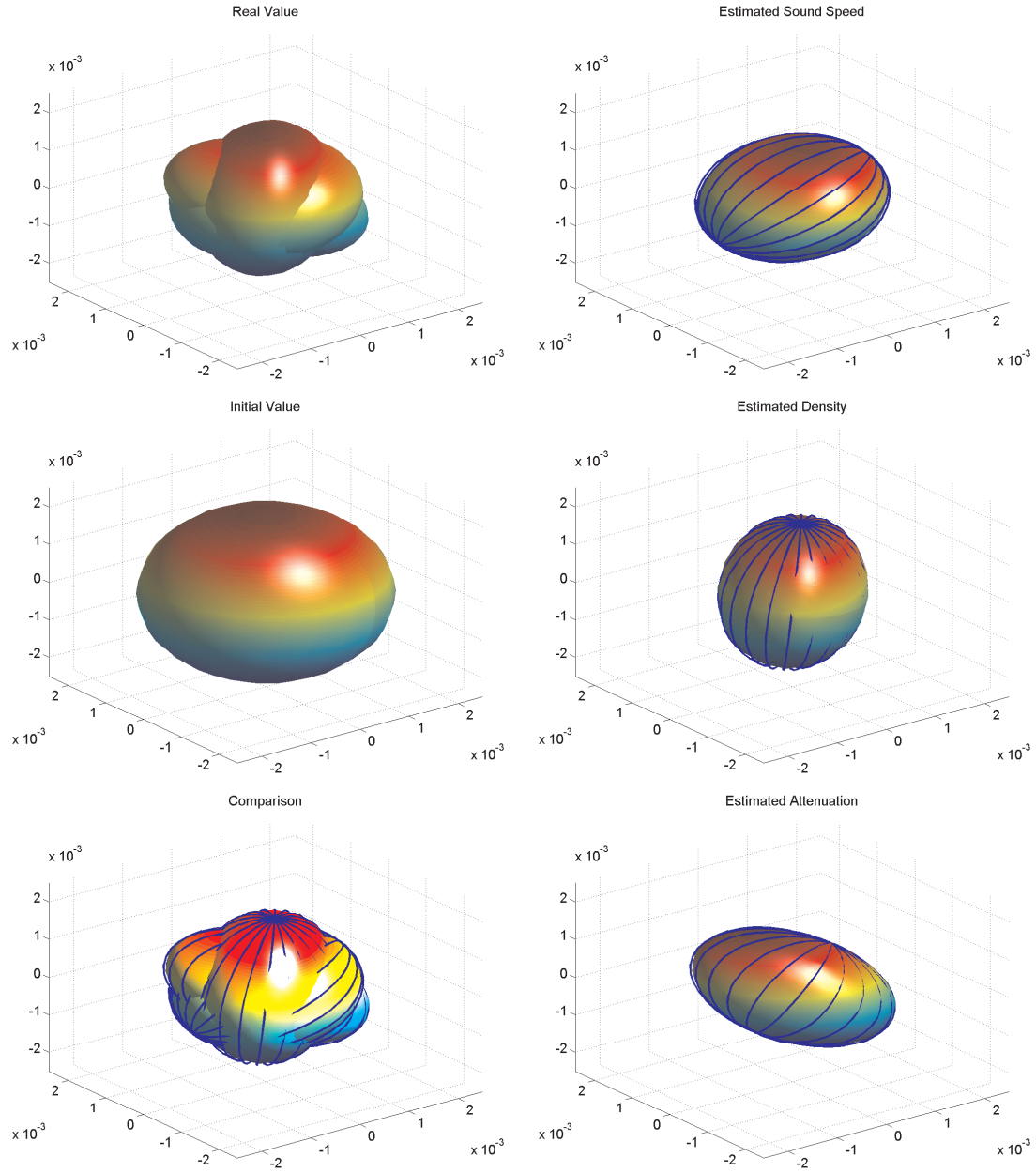


Figure 5.4: Case 1: Inversion for similarly sized and shaped ellipsoids.

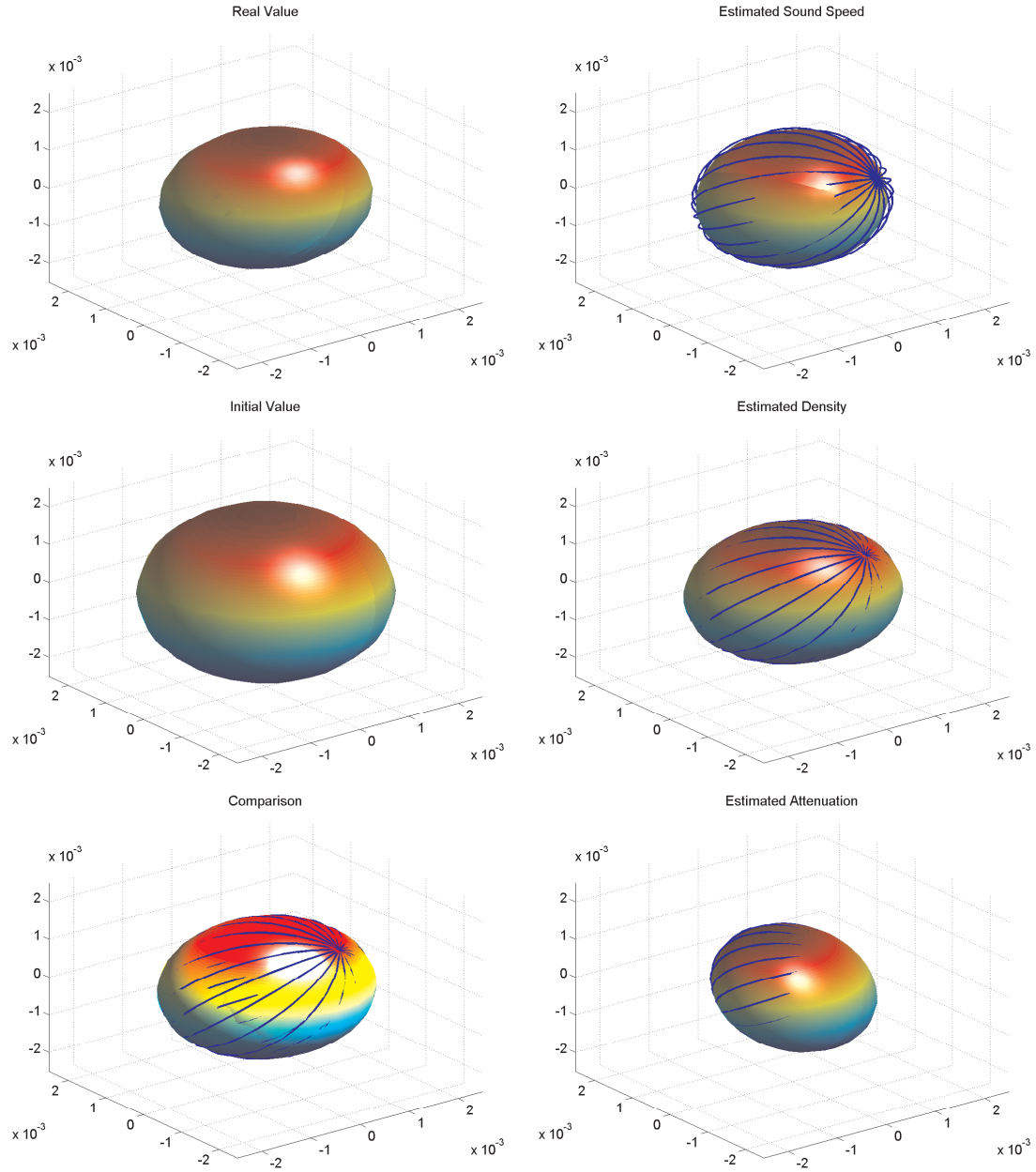


Figure 5.5: Case 2: Inversion for concentric and overlapping ellipsoids.

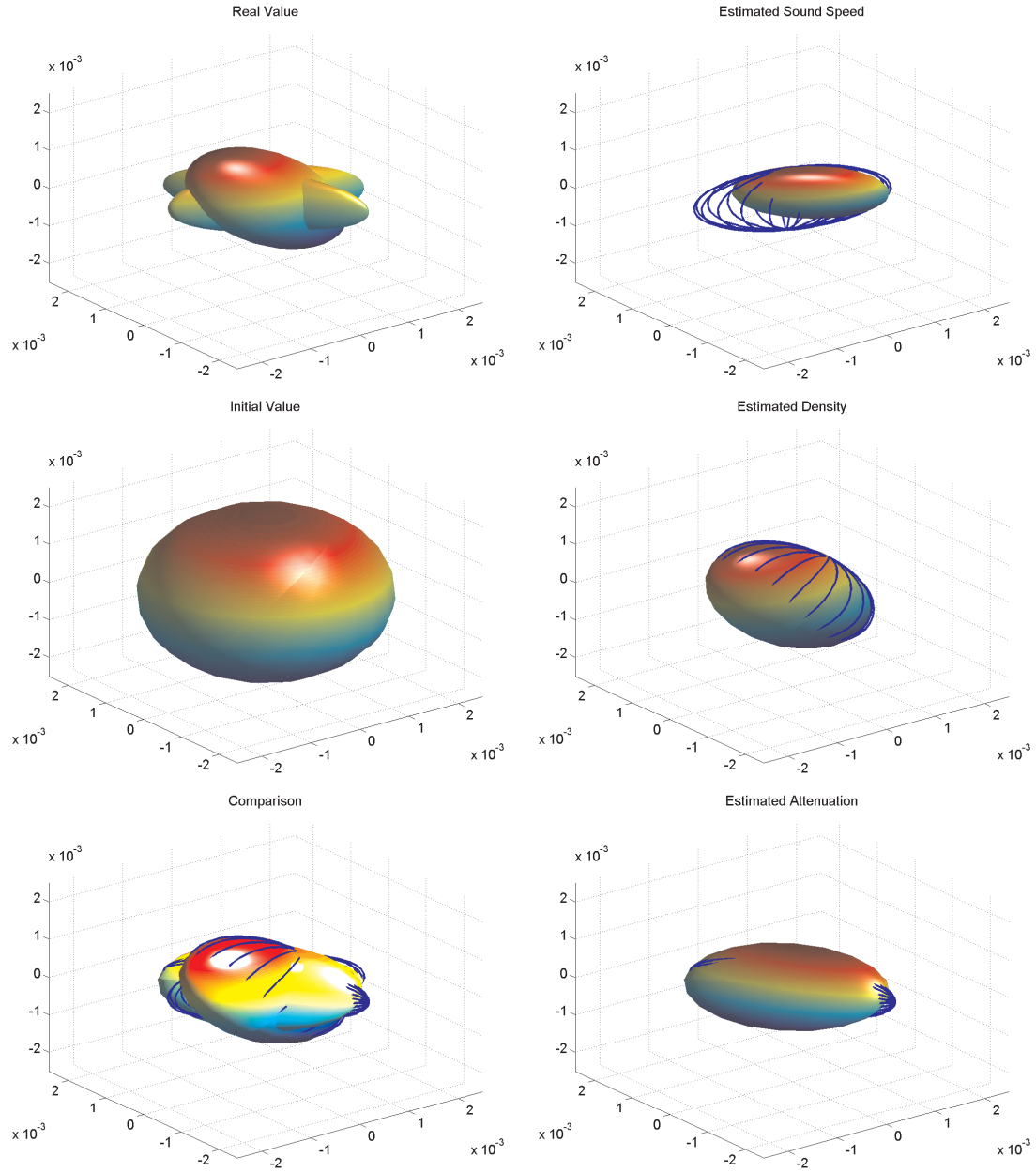


Figure 5.6: Case 3: Inversion for significantly different ellipsoids.

time is about 14 minutes.

In Figure 5.5 we examine a case in which we have three concentric, overlapping ellipsoids. This represents a lesion where the changes of the acoustic properties confined into a single region of space. At first glance it appears as if there is a single ellipsoid anomaly. However, we were able to classify three distinct ellipsoids with our method. Although the initial estimates for the contrasts are considerably different than the real values, we obtained a very good estimate for the contrasts and the geometries. The method we proposed to define the contrast of the object as a nonlinear parameter of the problem, greatly improved the contrast detection. The number of iterations required is 98 and the total computation time is about 14 minutes.

In the third case, Fig. (5.6), we study a scenario where we have three significantly different ellipsoids. We again have a quite successful localization of the perturbations. The slight differences are attributable to the dissimilar orientation angles and the noise in the data. Our observations revealed that, the rotation angles are the most difficult parameters to estimate for this type of shape based inversion problems. The number of iterations required is 299 and the total computation time is about 24 minutes. The same experiment is repeated with a noise level that sets the signal-to-noise to 40dB and a better localization is obtained for the sound anomaly.

5.3.2 Error Analysis

A statistical error analysis was done to assess more thoroughly the performance of the inversion method presented in this chapter. For this purpose, a Monte Carlo simulation was performed in which we considered 140 estimation problems

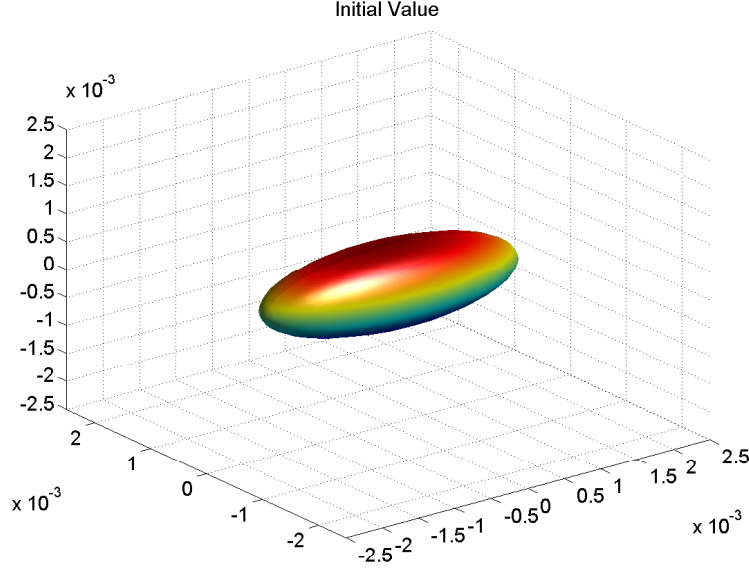


Figure 5.7: Common initial value for the simulations

where a common initial estimate shown in Fig. (5.7) was used to determine the structure of a randomly generated, HIFU-type ellipsoid. For each case, a randomly oriented real ellipsoid was selected so that it had up to 15% deviation in contrast, volume and direction from common initial ellipsoid. The errors in estimation for volume and contrast are computed using Eq.(5.21) and Eq.(5.22). The error distributions in volume and contrast are given in Fig. (5.8). For this test, Gaussian noise was added to the data to set the signal to noise ratio to 25dB.

Our observations revealed that for all the cases where the error was high the rotation parameters were significantly different than the actual values. Hence, rotation parameters are the most difficult parameters to estimate.

We had a very successful localization of the ellipsoidal shapes whereas the performance of the algorithm was slightly poorer for contrast estimation. However, for the visualization purposes the localization is more important and even

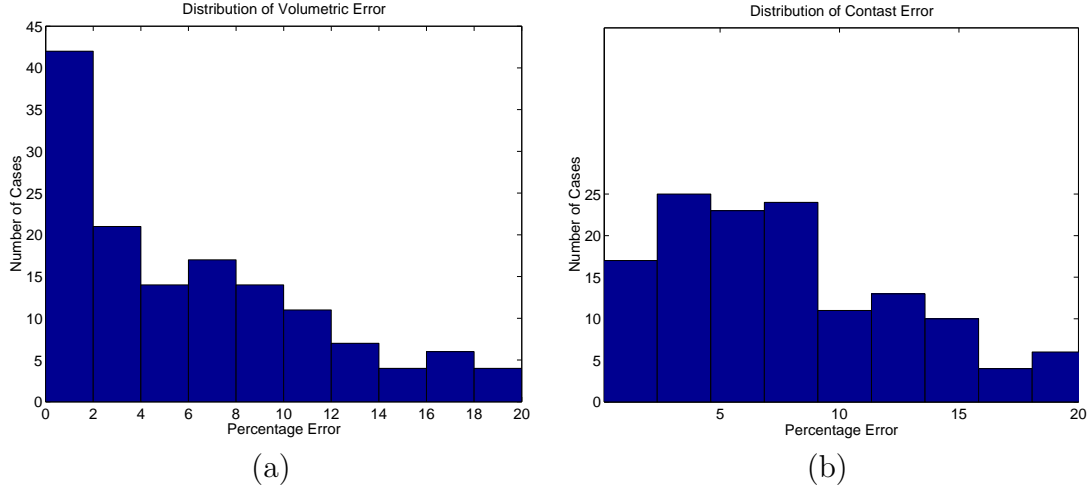


Figure 5.8: Distribution of volumetric and contrast errors

the contrast errors were higher, in 75% of the studied cases the error was less than or equal to 10%.

The results showed that, the method given in this chapter was largely successful to estimate the randomly oriented ellipsoids.

5.3.3 Laboratory Experiment and Results

A laboratory experiment was performed to validate the inversion method developed in this chapter. The ideas presented in Section 5.1 were used with data obtained from a single agar ellipsoid anomaly, which was volumetrically homogenous, immersed into a homogenous lossy medium. The backscattering measurements were obtained by a linear array transducer. The experiment and the simulation details are presented in the following sections.

Linear Array Transducer

The linear array transducer that is introduced in Chapter 4 is used for a backscattering experiment. The array (Model 8665, BK Medical, Wilmington,

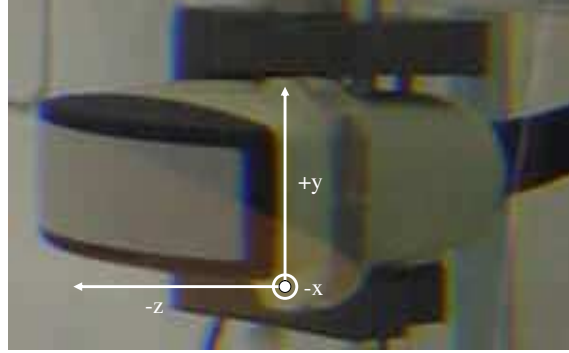


Figure 5.9: Linear array transducer

MA) consisted of 128 cylindrically curved elements, each of which could be controlled individually with the real time ultrasound scanner of Analogic Corporation (AN2300). The array operated at 3.5 MHz and each radiator element had 70.0 mm focal length with lateral dimensions $13 \text{ mm} \times 0.5 \text{ mm}$. The cylindrically concave elements were located on a curved transducer with 60 mm radius. The pitch between each element was 0.525 mm and the radial angle was 0.00875 radians. For this experiment the elements [54 59 64 69 74], first transducer was numbered as 1, were used to take measurements. The angle between each element used in this study was 0.0438 radians. The real transducer and the schematic showing the location of the cylindrically concave transducers on the linear array are given in Figures 5.9 and 5.10.

Experimental Conditions

The laboratory experiment settings are given in Fig. (5.11). The x-y-z coordinates of the ROI were defined in according to the coordinate axis of the transducer given in Fig. (4.1) and the origin was defined as the focal point of the 64th element. The linear array was scanned across the ellipsoid anomaly at five different measurement points. At each measurement point, single transducer

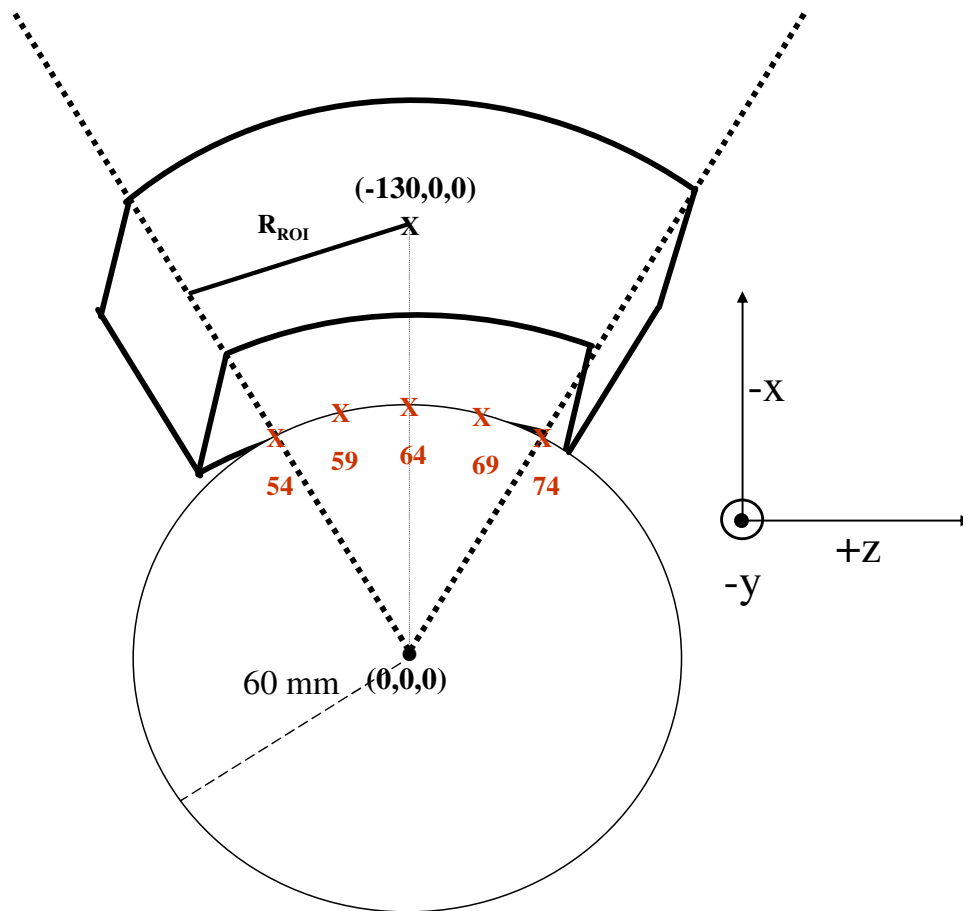


Figure 5.10: Schematic of the locations of the transducers on the transducer array

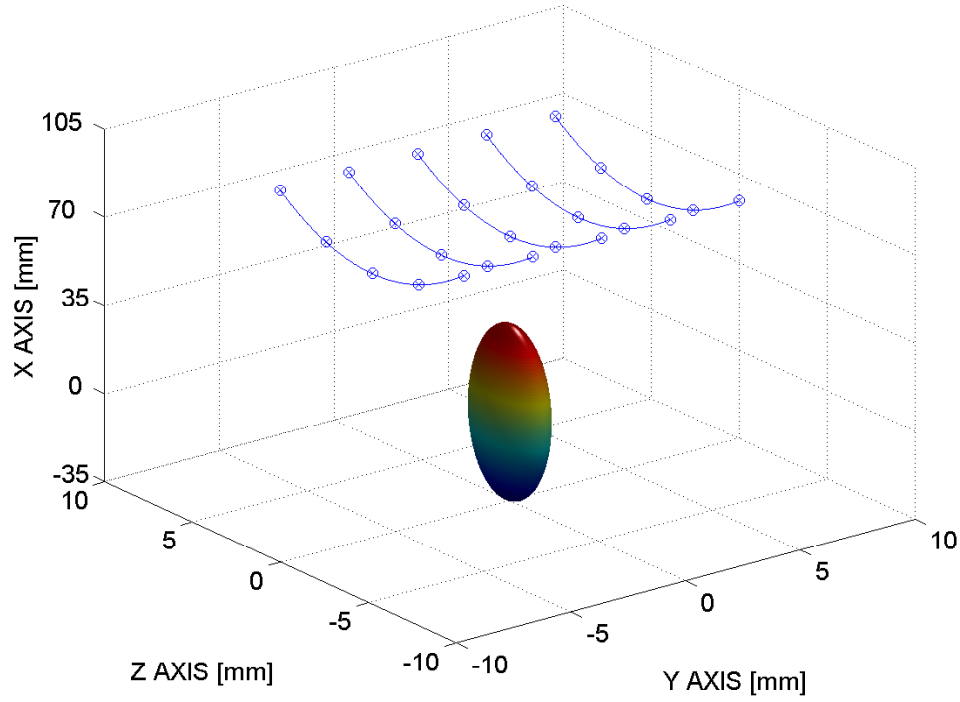


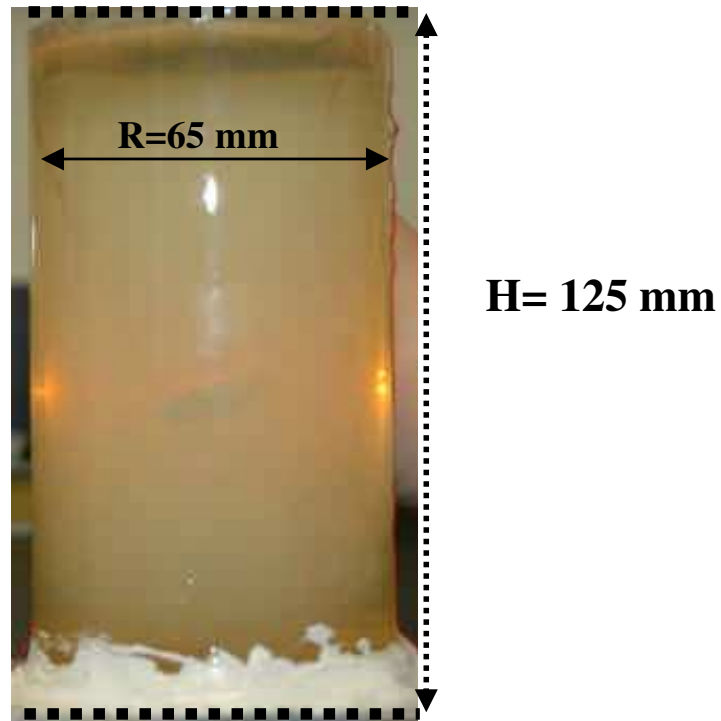
Figure 5.11: Laboratory Experiment Settings

insonified the medium and the interaction was measured by the five elements of the linear array. The array was scanned across the anomaly between $y=-6$ mm to $y=6$ mm with 3 mm step size.

The array transducer and the phantom was placed in a water tank ($35 \text{ cm} \times 53 \text{ cm} \times 35 \text{ cm}$) that was filled with de-ionized de-gassed water at approximately 21°C . Each cylindrically concave element was operated in transmit mode using AN2300 where the system excited the transducer with a short excitation signal that approximated a delta function. The data were transferred to a computer for later analysis.

Phantom

An ellipsoidal shaped phantom ($20 \text{ mm} \times 5 \text{ mm} \times 6 \text{ mm}$) is carved from an Agar sample which had the nominal acoustic properties of $c_p = 1551 \text{ m/s}$, $\rho_p = 1045 \text{ kg/m}^3$, $\alpha_p = 10.17 \text{ Np/m/MHz}$. Our previous experience with this material showed that, the actual parameters that should be used in the simulations are: $c_p = 1545 \text{ m/s}$, $\rho_p = 1045 \text{ kg/m}^3$, $\alpha_p = 54(\frac{\omega}{\omega_o})^{1.2} \text{ Np/m}$ where ω_o is the mean angular frequency ($2\pi 3.5 \text{ MHz}$) [94]. The ellipsoid was immersed into an optically transparent, cylindrically shaped (radius: 32.5 mm , height: 125 mm), polyacrylamide hydrogel with 7% Bovine Serum Albumin (BSA) protein concentration. The acoustic properties of the background phantom were: $c_b = 1540 \text{ m/s}$, $\rho_b = 1045 \text{ kg/m}^3$, $\alpha_b = 1.5 \text{ Np/m/MHz}$ [95]. The polyacrylamide hydrogel was used because it was optically transparent, and allowed visualizing of the ellipsoidal anomaly. Moreover, the BSA phantom had the same density with the Agar phantom which resulted in an experiment environment of which there was a single ellipsoidal anomaly and altered sound speed and attenuation values compared to the background. Therefore, this phantom configuration was a very good approximation to what one would have in real HIFU practice. We tried to place the ellipsoid so that it only had rotation with respect to the center axis of the cylinder. The real and the enhanced images of the BSA phantom are given in Fig. (5.12). A sample image (beamformed pre-scan converted) is obtained with the Analogic engine when the transducer is aligned with the ellipsoid ($y=0 \text{ mm}$) is given in Fig. (5.13). The data corresponding to the envelope of the signal from the 64th line of the image is given in Fig. (5.14).



(a)



(b)

Figure 5.12: The real and the enhanced images of the BSA phantom.

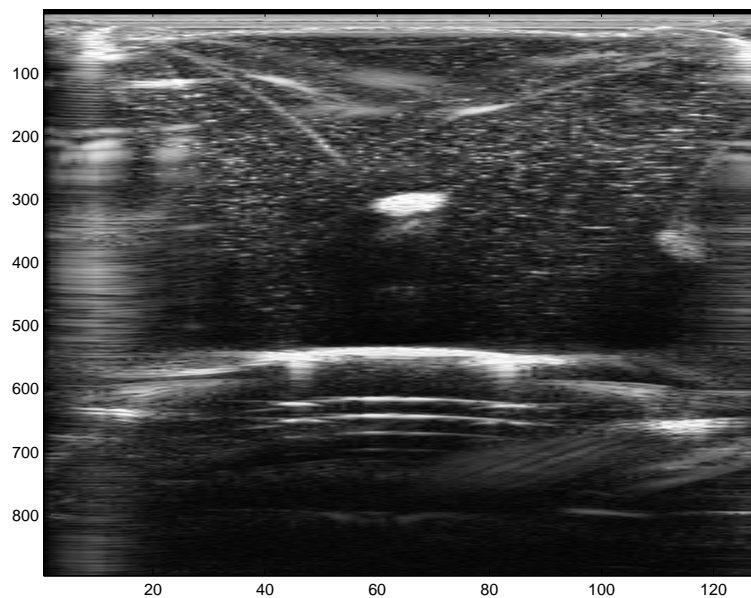


Figure 5.13: A sample image of the BSA phantom with Analogic Engine ultrasound scanner (B-mode pre-scan converted).

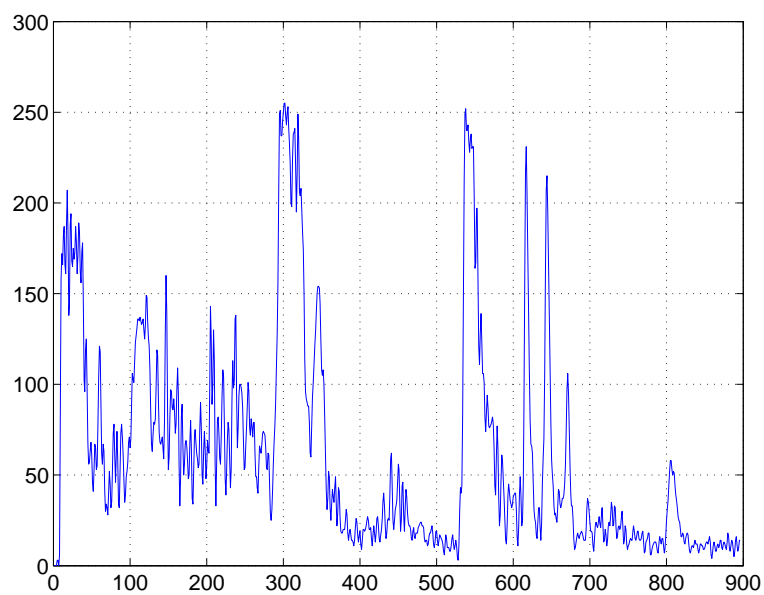


Figure 5.14: The data corresponding to the envelope of the signal from the 64th line of the image.

5.3.4 Simulation Grid and the Choice of Region of Interest

In Section 5.3.1, where we presented the inversion results with point receivers and transmitters, we had a cube shaped region of interest and we discretized Eq.(5.1) in similarly shaped sub-voxels. We will follow a different approach in this section. To make use of the symmetry properties of the cylindrically concave elements of the linear array, we will define an irregularly shaped ROI which will coincide with the shape of the transducer.

To present the forward model Eq.(3.32) is recalled in Eq.(5.23). The form of the equation that will be used in this case will be:

$$\begin{aligned} v_o(r_{to}, \omega) = & e_{pe} \int_{V'} c_p(r') \left[-\frac{2\omega^2}{c_b^3} \right] H(r_{to}, r', \omega) H(r', r_{so}, \omega) d^3 r' \\ & e_{pe} \int_{V'} \alpha_p(r', \omega) \left[-j \frac{2\omega}{c_b} \right] H(r_{to}, r', \omega) H(r', r_{so}, \omega) d^3 r' \quad (5.23) \end{aligned}$$

This equation can be written in a compact form as in Eq.(5.2) where K_3 is zero.

We shall discretize Eq.(5.23) and write it in the form of Eq.(5.3). For this purpose we first assume that, we have a rectangular shaped ROI (12 mmx20 mmx20 mm) where we choose to discretize the equation at 3.5 MHz, which is the nominal frequency, and use 0.5 wavelengths as the grid size (for 1550 m/s 0.2 mm). The number of voxels that we would have in this case is 600000.

The size of the \mathbf{K} matrix would depend on the number of transmitter and receiver combinations and the frequency values that one wants to use to solve the inverse problem. We choose to have 5 frequency values and 25×5 transducer receiver combinations. Using the method described in the previous chapter, to

compute the spatial transfer function for single frequency, location and transmitter receiver combination takes approximately 0.01 seconds in Matlab R14. Therefore, the total computation time for \mathbf{K} matrix would be approximately 1042 hours. This direct approach is computationally very expensive and not feasible. We have to use the symmetry properties of the transducer and reduce the size of the computation domain. For this purpose we will first introduce the sub-voxel approach.

To reduce the computation domain, the region of interest will be divided into subcells ($12 \times 20 \times 20$ with 1mm side length) where the perturbation values will be assumed constant in each sub-voxel. Mathematically speaking:

$$\begin{aligned} v_o(r_{to}, \omega) &= e_{pe} c_p \left[-\frac{2\omega^2}{c_b^3} \right] \int_{V_s} H(r_{to}, r', \omega) H(r', r_{so}, \omega) d^3 r' \\ &\quad e_{pe} \alpha_p(\omega) \left[-j \frac{2\omega}{c_b} \right] \int_{V_s} H(r_{to}, r', \omega) H(r', r_{so}, \omega) d^3 r' \quad (5.24) \end{aligned}$$

where V_s represents the sub-voxel. This approach would reduce the number of voxels needed to represent the anomaly but the spatial transfer function should be computed individually for each transducer for the complete ROI.

A fast method is introduced to compute the following integral:

$$\int_{V_s} H(r_{to}, r', \omega) H(r', r_{so}, \omega) d^3 r' \quad (5.25)$$

where the transfer function for single transducer is calculated and the reciprocity of the cylindrically concave elements is used to find the response for the other radiators. Specifically, for a homogeneous medium, the spatial transfer function takes the absolute value of the distance between the transducer and the observation point as input. Therefore, the response computed for a transducer at a

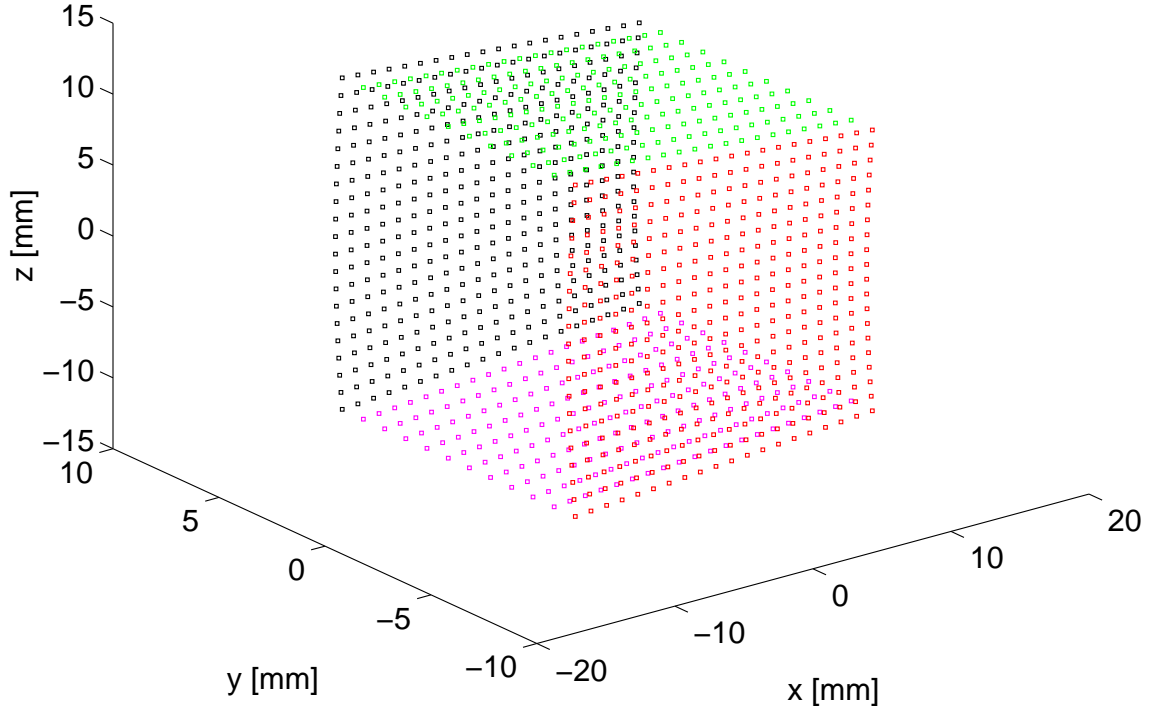


Figure 5.15: Region of Interest in 3D

certain observation point will have the same expression for another transducer, which has the same relative position with respect to that observation point. e.g. The response computed at the focus of the 64th transducer can be used to obtain the response at the focus of the 54th transducer, although the two transducers are located at different positions in the ROI.

To implement this idea, a new ROI is defined. The ideas presented before (Eq.(5.23) and Eq.(5.24)) shall stay the same but applied to an irregularly shaped grid. The shape of the ROI where discretization will be applied is given in Figures (5.10) and (5.15). The location of the transducers with respect to the ROI is given in Fig. (5.10).

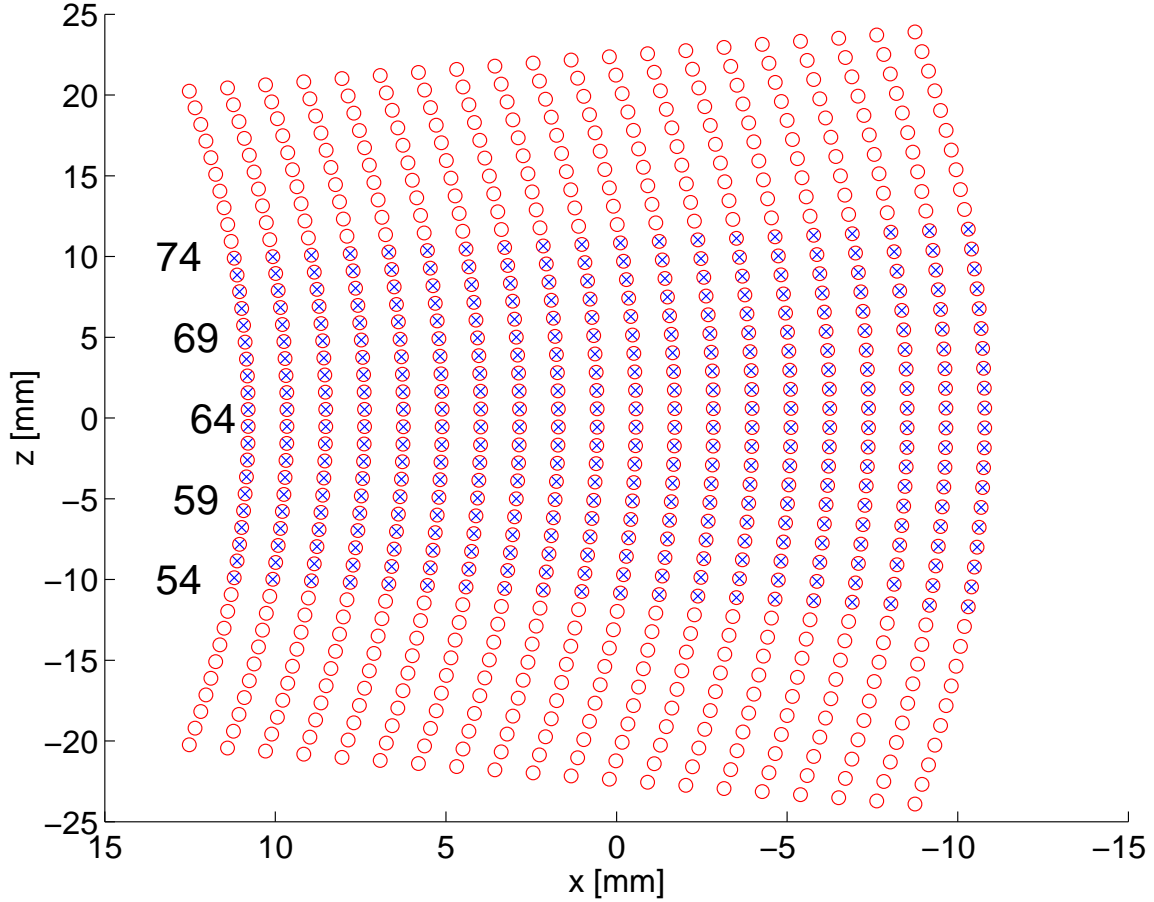


Figure 5.16: Region of Interest in 2D

The symmetry properties of the transducer and the reasons behind this shape of ROI can be better understood from a 2D picture. A 2D slice of the ROI which is defined in polar coordinates with the parameters ($r_a < r < r_b$, and, $-\theta_a < \theta < \theta_a$) is plotted in blue in Fig. (5.16). Now for the center transducer (64) one computes the spatial transfer function at each pixel of a computation grid which is twice the size of the original ROI ($-2\theta_a < \theta < 2\theta_a$). This region is shown in red in Fig. (5.16). For the center transducer one would use the spatial transfer function values computed in the pixels corresponding to values between $(-\theta_a < \theta < \theta_a)$ and for the transducer on the side (54) one would use the values

computed at $(0 < \theta < 2\theta_a)$. To make sure that the pixels overlap during this process, the increment in the angle parameter is chosen as the angular pitch size of the linear array. Moreover, due to the symmetry properties of the cylindrically concave transducers one will only need to compute the values at the half of the ROI, between $(0 < \theta < 2\theta_a)$.

In each sub-voxel, the Gaussian quadrature approach is used to compute Eq.(5.25). For this purpose the spatial transfer function of the center transducer (64) is computed at the Gaussian nodes and stored with the Gaussian weights and the volume of each sub-voxel. The stored values are recalled to create the forward matrix that will be used in this study.

The parameters that is used in our simulation will be given here: 5 frequency values equally sampled between 2.5MHz and 3MHz are used. The computation grid was described with the parameters $0 \leq y \leq 12$ mm, $118.6 \leq r \leq 141.36$ and $0 \leq \theta \leq 10$ (degrees). Total number of voxels was 4800 ($12 \times 20 \times 20$). Total time to compute the spatial transfer response of the center transducer was 27.8 hours at 667MHz Unix workstation with 4 processors and 1GB Ram per processor. Total computation time required to obtain the forward matrix for all the transducers was 28.1 hours.

The calibration signal for this transducer is previously calculated in Chapter 4 in Eq.(4.57) and, the e_{pe} signal is obtained with: $e_{pe} = e_T(\omega)^2$.

5.3.5 Results

The first task to be done is to find the exact location of the ellipsoid with respect to the transducer. Although maximum effort is used to place the ellipsoid

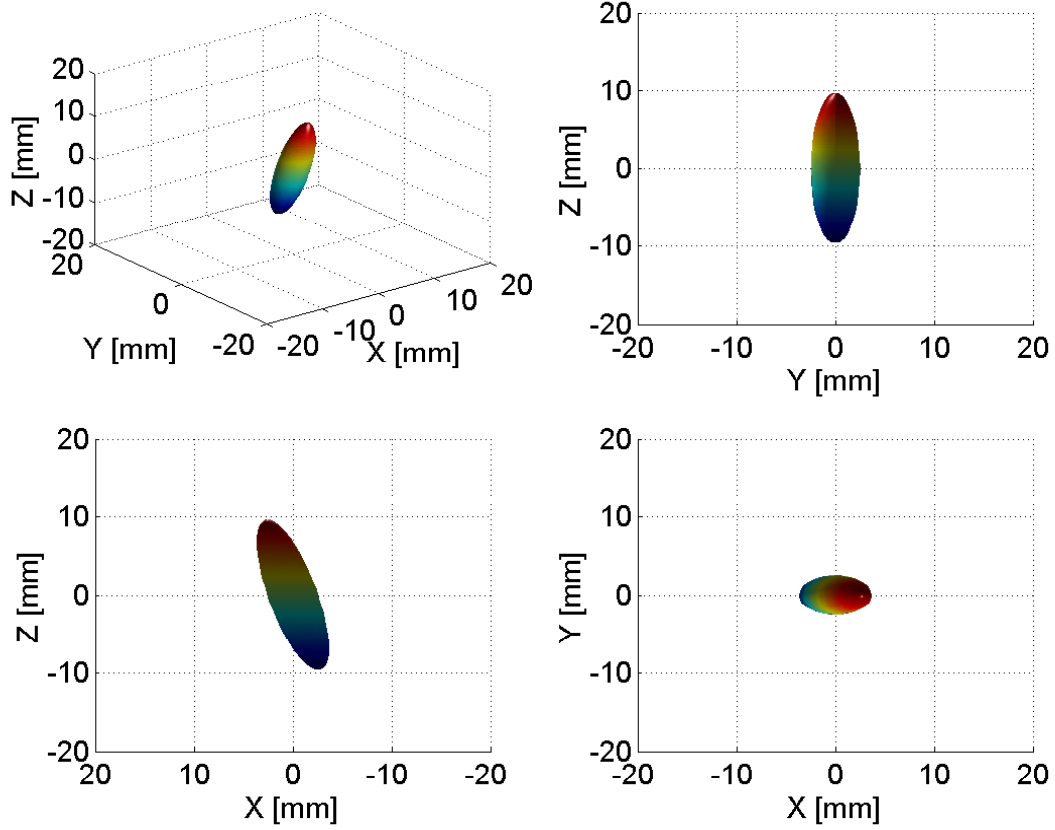


Figure 5.17: Initial true ellipsoid distribution from different view angles

to align with the transducer, the location of the exact radiators in the transducer and the positioning errors (on the order of mm) cannot be controlled. In Fig. (5.17) the ellipsoid, which is provided to the optimization routine as initial guess to find the true ellipsoid, is displayed from different view angles.

In Fig. (5.18) the true ellipsoid, which is obtained from the optimization routine is provided. The number of iterations required was 157. The minor differences are attributable to the experimental errors as discussed before.

Next, the inversion method described in Section 5.2 is used to recover the ellipsoid from a significantly different initial value. The bounds for the contrasts, M_i , were chosen as:

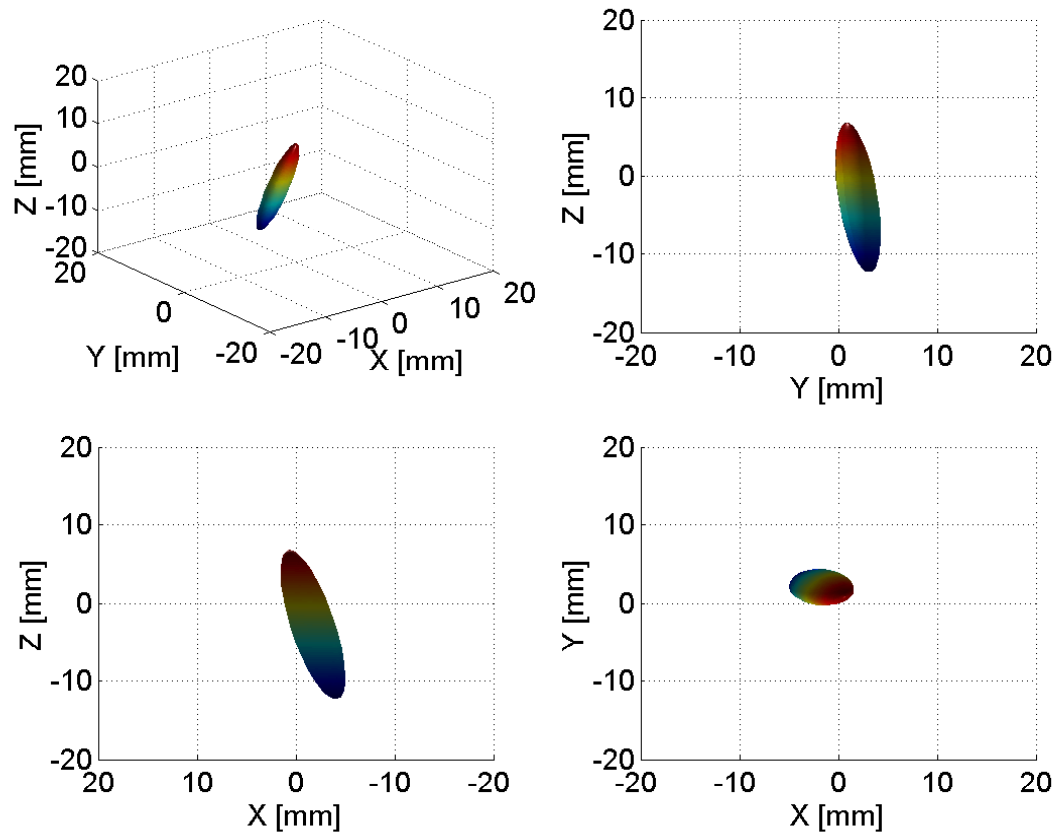


Figure 5.18: True ellipsoid distribution from different view angles

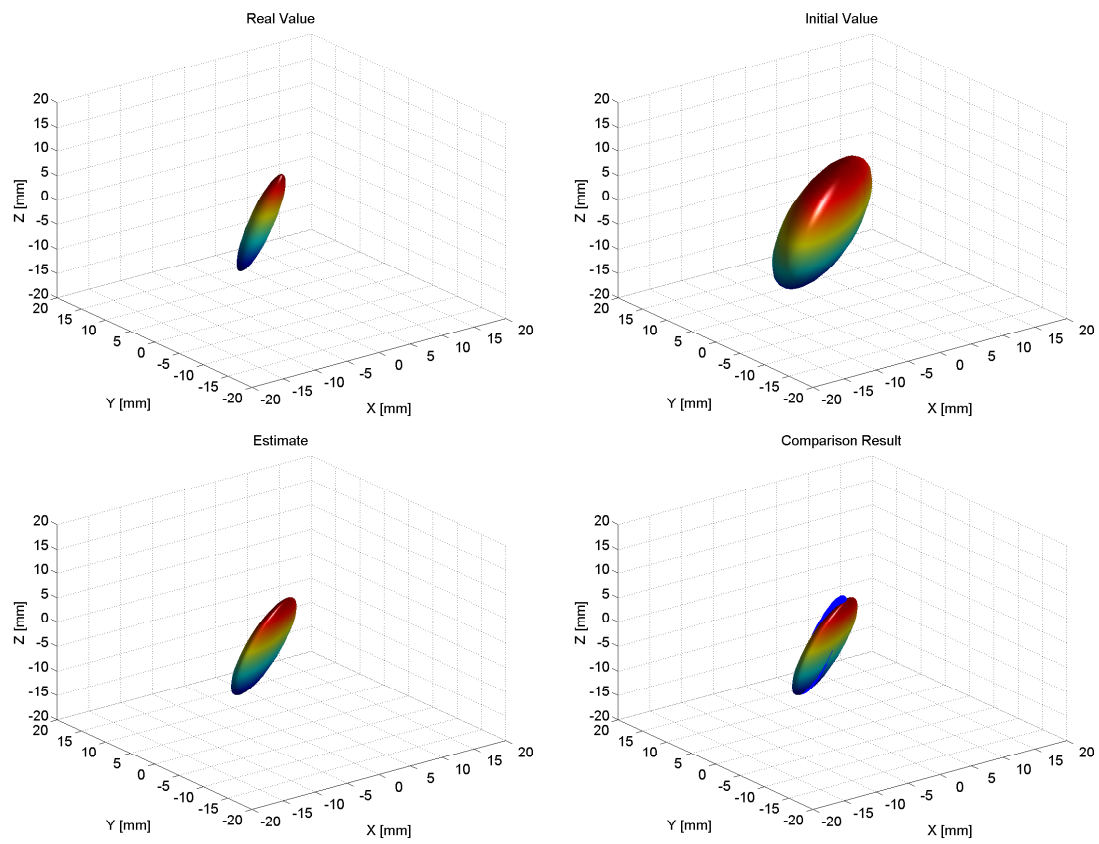


Figure 5.19: Experimental inversion result

Table 5.3: Lower and upper limits for the geometric parameters of the ellipsoid

	Lower Limit	Upper Limit
x_o	-20 mm	20 mm
y_o	-20 mm	20 mm
z_o	-20 mm	20 mm
l_1	5×10^{-4}	20 mm
l_2	5×10^{-4}	20 mm
l_3	5×10^{-4}	20 mm
θ_1	0	2π
θ_2	0	π
θ_3	0	2π

- $0 \text{ m/s} < M_c < 20 \text{ m/s}$
- $0 \text{ Np/m} < M_a < 440 \text{ Np/m}$

The bounds for the geometric parameters are given in Table 5.3.

In Fig. (5.19) we display the true ellipsoid, initial guess provided to our estimation method and the final result. For comparison purposes, the expected shape is plotted with blue lines on the estimated ellipsoid. The number of iterations required was 116 and the total computation time was about 26 minutes. We were able to recover the geometry information quite accurately.

The inversion algorithm is based on a local minimum optimization routine (Gauss-Newton) and is sensitive to the initial value selection. To select the geometric parameters of the initial value, a physics based approach is used. In HIFU problems, there is a significant prior information about the lesion and the initial estimates of its location and orientation can be determined by the HIFU transducer. The long axis of the lesion would be parallel to the ultrasound beam. Therefore, for this problem, it is assumed that the location and the orientation of the ellipsoid were roughly known but the dimensions were unknown. The initial estimate obtained with this logic is given in Fig. (5.19).

Table 5.4: Contrast and error values for the sound speed and attenuation

	Real	Initial	Estimate	Err _c	Err _v
Sound (m/s)	5	20	5.80	16.15	5.72
Attenuation (Np/m)	48.7	440	46.34	6.89	5.72

The quantitative acoustic parameters of the ellipsoid is of interest here. The initial contrast values provided to the optimization routine and the expected values are given in Table 5.4. Although, the initial values were considerably different than the real values, an accurate estimate is obtained for the contrast parameters.

5.4 Conclusion

The use of wave based inversion methods for medical ultrasound imaging is not common. Primarily, the size of the region of interest makes the traditional inversion methods rather impractical. However, wave based inversion is well suited to the application of HIFU lesion detection. There is a significant prior information about the lesion and the initial estimates of its size, location and orientation can be determined by the HIFU transducer. Moreover, HIFU lesions are in well defined geometric shapes and the changes in the acoustic parameters are well documented.

In this chapter a shape based parametrization method is demonstrated to determine the acoustic properties and the spatial structure of the HIFU lesion. This preliminary work indicates that, a linearized physics based model, coupled with a shape based inversion routine, provides a feasible method to monitor the progress of image guided therapy.

We exploited the fact that, the treatment results in an ellipsoidal shaped region and proposed a differentiable function to describe the boundary and the contrast of the ellipsoid. The physical size of the region, in which the lesion resides, results in the need to build and manipulate large matrices. We introduced a reduced order method for synthesizing and manipulating these matrices.

Three numerical experiments were performed with point sources. Two cases were presented where the ellipsoids describing the shapes were not identical, and another case in which the spatial changes in the acoustic properties were enclosed within a single ellipsoid. In all of the cases we were able to reconstruct the geometry and the contrasts quite accurately. The results presented here were obtained under 200 iterations using a Matlab implementation on a 1GHz Linux workstation. The computation time was less than 25 minutes for all results.

A laboratory experiment was performed with a clinically used linear array transducer. An ellipsoidal phantom was used which had perturbation in sound speed and attenuation only and the spatial changes in the acoustic properties were enclosed within a single ellipsoid. We were able to reconstruct the geometry of the ellipsoid and the contrasts accurately. The results were obtained with 116 iterations using a Matlab implementation on a 667MHz workstation. The computation time was 26 minutes.

The algorithms and the models presented in this chapter built a foundation to expand these ideas to in-vitro and ex-vivo applications.

The method can be expanded to the specialization of the models to the inhomogeneous ellipsoids and the characterization methods beyond ellipsoidal shapes.

The method assumes volumetrically homogenous shapes which can be extended to inhomogeneous ellipsoids [56]. The change in the contrast parameter can be defined as a smooth function which is approximated with a low order polynomial. In this case one will only need to determine a few number of additional parameters per ellipsoid depending on the order of the polynomial.

A more flexible shape based method to parameterize the structure of the HIFU lesions might also be examined. Moving beyond the ellipsoidal structures might be required if the shape of the lesions cannot be adequately described with the ellipsoids. It has been reported in the literature that, "tadpole" shaped lesions are observed for the cases where significant cavitation activity is present.

Conclusion and Future Work

6.1 Objectives and Specific Aims

The objective of this dissertation is the development and validation of quantitative, fully three dimensional ultrasonic imaging methods to characterize the location and the spatial structure of the High Intensity Focused Ultrasound (HIFU) lesions.

Specific Aim #1 To develop a well calibrated physical forward model that describes the propagation of ultrasound in human tissue. The forward model should be sensitive to the changes in the acoustic properties, sound speed, attenuation and density.

Specific Aim #2 To develop a geometry based inversion method for lesion identification.

Specific Aim #3 To validate the inversion algorithm using tissue-mimicking phantoms with known perturbations in acoustic properties and determine the accuracy of image reconstruction method.

6.2 Overview and Significance

In this study we focused on developing a geometry based characterization method to monitor the HIFU lesions. A shape based inversion method which uses ultrasound backscatter data was proposed to determine the spatial distribution of sound speed, attenuation and density of the lesions. Processing the data in this manner, reconstructing the acoustic parameters from ultrasound measurements, is known as inverse problem and the method we propose can be used for a wide range of reconstruction problems. In this dissertation, we focused on cancer treatment applications.

HIFU is a cancer treatment technique where high frequency sound waves (ultrasound) are used to necrose the cancerous tissue without damaging the surrounding healthy tissue. An important open issue in developing HIFU methods for clinical use is monitoring the progress of the treatment by non-invasive imaging techniques. In this work, we exploit the fact that the treatment results in ellipsoidal (1-20 mm length) lesions in which the acoustic properties of the tissue sound speed and attenuation - are altered from their nominal values.

Even under the assumption of a linearized scattering model such as that provided by the Born approximation, the computational size of the most relevant 3D problems makes traditional pixel based inversion methods impractical. Hence in this work, we introduce a shape-based method under which we need to estimate a small number of parameters to describe the 3D shape of the lesion. More specifically, we consider a number of options for shape estimation depending on whether one is interested in a single physical unknown or multiple quantities (sound speed, attenuation, and density) each of which may be altered by the HIFU treatment.

The physical size of the region in which the lesion resides results in the need to build and manipulate large matrices which define the underlying linearized model. Thus, the second issue we propose to solve is the development of new, reduced order methods for synthesizing and manipulating these matrices.

Significance: The use of wave based inversion methods for medical ultrasound imaging is not common. Primarily, the size of the region of interest makes the traditional inversion methods rather impractical. However, wave based inversion is well suited to the application of HIFU lesion detection. There is a significant prior information about the lesion and the initial estimates of its size, location and orientation can be determined by the HIFU transducer. Moreover, HIFU lesions are in well defined geometric shapes and the changes in the acoustic parameters are well documented.

6.3 Preliminary Studies: A shape-based approach to the tomographic Ultrasonic imaging problem

Our initial efforts were focused on developing a time domain propagation model that describes the scattering of ultrasound in homogenous medium. We presented a model which computes the acoustic field scattered by localized inhomogeneities embedded into homogenous lossless background. Our efforts to validate the forward method with laboratory measurements taken from a spherically focused transducer, presented a need to develop a calibration method for such transducers. We have shown, both theoretically and experimentally, that

the calibration signal for these type of radiators can be measured using either a flat-plate or a point scatterer. The reflected waveforms in each case are not identical but rather related by an operation of double differentiation.

Next, the ideas that have been developed for time domain propagation of ultrasound are applied to the frequency domain where we concentrated on the development and validation of the frequency domain Born model for lossy medium. We linearized our problem and defined the inhomogeneities in the acoustic properties as perturbations to a homogenous, lossy background model. The scattered acoustic wave for such a medium is expressed linearly in terms of the perturbations in sound speed, attenuation and density. The frequency dependency of attenuation is characterized by a power-law relation. Moreover, we demonstrated a fast method to solve the pressure field of spherically curved radiators for frequency domain applications.

Our final aim should be to implement these ideas in medical imaging area and the conventional ultrasound transducers used for medical imaging purposes are generally of phased array type. Therefore, to apply our methods to more realistic scenarios, we developed a method to simulate the forward field from phased array transducers which have cylindrically concave elements.

We introduced a semi-analytic fast method which computes the forward field from cylindrically concave transducers for any type of attenuating medium. We compared our method to an optimized numerical integration routine which computes this response numerically. The speed improvement is obtained as 40 to 1400. With our method, for the frequency domain applications where we need to find the background field for a few frequency values, the response can be obtained almost immediately.

Finally, we introduced a shape based inversion method which integrates the methods that we developed so far. We demonstrated a shape based parametrization model to determine the acoustic properties and the spatial structure of the HIFU lesion. We used the fact that, the treatment results in ellipsoidal shaped lesions. We proposed a differentiable function to describe the boundary and the contrast of the ellipsoid.

We performed three numerical experiments with point sources and one laboratory experiment with the linear array transducer. In all of the cases we were able to reconstruct the geometry and the contrasts quite accurately.

6.4 Future work: Design and Methods

The algorithms and the models presented in this dissertation built a foundation to expand these ideas to in-vitro and ex-vivo applications. The work that remains to be done in this area are the specialization of the models to the inhomogeneous background and expansion of the characterization methods beyond ellipsoids.

Forward Problem:

Rytov-Model: In HIFU imaging experiments we are able to collect ultrasound data before the HIFU is used to create lesions in the tissue. Hence, the problem we need to solve can be defined as a differential change estimation in acoustic parameters. For this type of problems the Rytov model is known to be more appropriate than the Born approximation. Therefore, a new model can be introduced for the inverse problem in which the

change from Born approximation to Rytov model would require only the use of different normalization for the data [96].

Inhomogeneous Background: The method that we developed in this dissertation is valid for homogenous, lossy, power-law attenuating medium. More complicated methods which are not using Born approximation can be developed to handle tissue like inhomogeneous media. For many medical applications, we are often interested in determining the propagation of ultrasound waves due to tissue layers of fat and muscle. A closed form expression for such media in terms of spherical harmonics is previously presented in [97]. This idea can be explored for our specific HIFU monitoring problem.

Inverse Problem:

Inhomogeneous ellipsoids: The method we developed assumes volumetrically homogenous shapes which can be easily extended to inhomogeneous ellipsoids [56]. The change in the contrast parameter can be defined as a smooth function which is approximated with a low order polynomial. In this case one will only need to determine a few number of additional parameters per ellipsoid depending on the order of the polynomial.

Non-ellipsoidal shapes: A more flexible shape based method to parameterize the structure of the HIFU lesions might also be examined. Moving beyond the ellipsoidal structures might be required if the shape of the lesions cannot be adequately described with the ellipsoids. It has been reported in the literature that, "tadpole" shaped lesions are observed for

the cases where significant cavitation activity is present.

Background Estimation: The application of the homogenous model to invert anomalies embedded into inhomogeneous medium can be explored. However, one should have a good estimate of the background parameters. In ultrasound images we have speckles. Randomly positioned point scatterers can be used to model these speckles and the measurements obtained before creating the lesions can be used to estimate the optimal background parameter values.

Laboratory Experiments:

The experiments that we presented in this dissertation may be followed by ex vivo studies. The imaging data can be collected on AN2300 ultrasound engine (Analogic Corporation, Peabody MA) which gives an access to unbeamformed RF data for inversion algorithms. Ex vivo studies can be carried out using excised tissue samples. The background field can be measured with backscattering experiments and compared to the predicted waveforms obtained from our forward models. Next, individual HIFU lesions can be created in the tissue to validate the reconstruction algorithm that we presented in this study.

Acoustic Field of the Cylindrically Concave Transducers

The type of the integral that we need to solve to obtain the spatial transfer function of a cylindrical radiator can be represented in a compact form such as:

$$\frac{R}{2\pi} \int_{\phi_{min}}^{\phi_{max}} \int_{F_1(\phi)}^{F_2(\phi)} \frac{e^{-jkr}}{\sqrt{r^2 - M(\phi)}} dr d\phi \quad (\text{A-1a})$$

where

$$F_1(\phi) = \sqrt{M(\phi) + A_{zp}} \quad (\text{A-1b})$$

$$F_2(\phi) = \sqrt{M(\phi) + B_{zp}} \quad (\text{A-1c})$$

$$M(\phi) = r_p^2 + R^2 - 2r_p R \cos(\phi - \phi_p) \quad (\text{A-1d})$$

where A_{zp} and B_{zp} represent the region specific constants defined by the z_p value of the observation point.

A.1 Case 1: Regions I and II $0 \leq \phi_p \leq \phi_t$

In this region $M(\phi)$, $F_1(\phi)$ and $F_2(\phi)$ are represented by:

$$M(\phi) \approx (r_p^2 + R^2 - 2r_p R \cos(\phi_p)) - (2r_p R \sin(\phi_p))\phi \quad (\text{A-2a})$$

$$+ (r_p R \cos(\phi_p))\phi^2 \quad (\text{A-2b})$$

$$= a + b\phi + c\phi^2 \quad (\text{A-2c})$$

$$F_1(\phi) \approx \sqrt{a + b\phi + c\phi^2 + A_{zp}} \quad (\text{A-2d})$$

$$F_2(\phi) \approx \sqrt{a + b\phi + c\phi^2 + B_{zp}} \quad (\text{A-2e})$$

A.1.1 Region I: $\phi_{\max} < \tan\phi_p \leq \phi_t$

The expression for the spatial transfer function is given by:

$$H = \frac{R}{2\pi} \left[\begin{array}{cc} \int_{F_1(\phi_{\max})}^{F_1(\phi_{\min})} e^{-jkr} [-\Psi_1(r)] dr & + \int_{F_2(\phi_{\max})}^{F_2(\phi_{\min})} e^{-jkr} [\Psi_2(r)] dr + \\ \int_{F_1(\phi_{\min})}^{F_2(\phi_{\min})} e^{-jkr} [-\Psi_3(r)] dr & + \int_{F_1(\phi_{\max})}^{F_2(\phi_{\max})} e^{-jkr} [\Psi_4(r)] dr \end{array} \right] \quad (\text{A-3})$$

where

$$\Psi_1(r) = -\frac{1}{\sqrt{c}} \arcsin \left(\sqrt{1 - \frac{4cA_{zp}}{b^2 + 4r^2c - 4ac}} \right) \quad (\text{A-4a})$$

$$\Psi_2(r) = -\frac{1}{\sqrt{c}} \arcsin \left(\sqrt{1 - \frac{4cB_{zp}}{b^2 + 4r^2c - 4ac}} \right) \quad (\text{A-4b})$$

$$\Psi_3(r) = -\frac{1}{\sqrt{c}} \arcsin \left(\frac{-2c\phi_{\min} - b}{\sqrt{b^2 + 4r^2c - 4ac}} \right) \quad (\text{A-4c})$$

$$\Psi_4(r) = -\frac{1}{\sqrt{c}} \arcsin \left(\frac{-2c\phi_{\max} - b}{\sqrt{b^2 + 4r^2c - 4ac}} \right) \quad (\text{A-4d})$$

$$\phi_{\min} = -\arcsin(l/R) \quad (\text{A-4e})$$

$$\phi_{\max} = \arcsin(l/R) \quad (\text{A-4f})$$

A.1.2 Region II: $\tan\phi_p \leq \phi_{\max}$

The expression is given as the summation of the two responses:

$$\int_{\phi_{\min}}^{\phi_{\max}} \int_{F_1(\phi)}^{F_2(\phi)} dr d\phi = H_1 + H_2 \quad (\text{A-5})$$

H_1 :

$$H_1 = \frac{R}{2\pi} \left[\begin{aligned} &\int_{F_1(\phi_{\max})}^{F_1(\phi_{\min})} e^{-jkr} [-\Psi_1(r)] dr + \int_{F_2(\phi_{\max})}^{F_2(\phi_{\min})} e^{-jkr} [\Psi_2(r)] dr + \\ &\int_{F_1(\phi_{\min})}^{F_2(\phi_{\min})} e^{-jkr} [-\Psi_3(r)] dr \end{aligned} \right] \quad (\text{A-6})$$

where

$$\phi_{\min} = -\arcsin(l/R) \quad (\text{A-7a})$$

$$\phi_{\max} = \tan(\phi_p) \quad (\text{A-7b})$$

The $\Psi_4(r)$ integral vanishes in this interval.

H_2 :

$$H_2 = \frac{R}{2\pi} \left[\begin{aligned} &\int_{F_1(\phi_{\min})}^{F_1(\phi_{\max})} e^{-jkr} [-\Psi_1(r)] dr + \int_{F_2(\phi_{\min})}^{F_2(\phi_{\max})} e^{-jkr} [\Psi_2(r)] dr + \\ &\int_{F_1(\phi_{\max})}^{F_2(\phi_{\max})} e^{-jkr} [\Psi_4(r)] dr \end{aligned} \right] \quad (\text{A-8})$$

where

$$\phi_{\min} = \tan(\phi_p) \quad (\text{A-9a})$$

$$\phi_{\max} = \arcsin(l/R) \quad (\text{A-9b})$$

The $\Psi_3(r)$ integral vanishes in this interval.

A.2 Case 2: Region III, $\phi_t < \phi_p \leq \pi - \phi_t$

$$H = \frac{R}{\pi(-b)} \left[\begin{array}{cc} \int_{F_2(\phi_{max})}^{F_2(\phi_{min})} e^{-jkr} [\sqrt{B_{zp}}] dr & + \int_{F_1(\phi_{min})}^{F_2(\phi_{min})} e^{-jkr} [-\Psi_5(r)] dr \\ + \int_{F_1(\phi_{max})}^{F_2(\phi_{max})} e^{-jkr} [\Psi_6(r)] dr & + \int_{F_1(\phi_{max})}^{F_1(\phi_{min})} e^{-jkr} [-\sqrt{A_{zp}}] \end{array} \right] \quad (\text{A-10})$$

$$\Psi_5(r) = \sqrt{r^2 - (a + b\phi_{min})} \quad (\text{A-11a})$$

$$\Psi_6(r) = \sqrt{r^2 - (a + b\phi_{max})} \quad (\text{A-11b})$$

$$F_1(\phi) = \sqrt{a + b\phi + A_{zp}} \quad (\text{A-11c})$$

$$F_2(\phi) = \sqrt{a + b\phi + B_{zp}} \quad (\text{A-11d})$$

$$\phi_{min} = -\arcsin(l/R) \quad (\text{A-11e})$$

$$\phi_{max} = \arcsin(l/R) \quad (\text{A-11f})$$

A.3 Case 3: Regions IV and V $\pi - \phi_t \leq \phi_p \leq \pi$

$M(\phi)$, $F_1(\phi)$ and $F_2(\phi)$ have the same forms in Section 4.3.1 as:

$$M(\phi) \approx (r_p^2 + R^2 - 2r_p R \cos(\phi_p)) - (2r_p R \sin(\phi_p))\phi \quad (\text{A-12a})$$

$$+ (r_p R \cos(\phi_p))\phi^2 \quad (\text{A-12b})$$

$$= a + b\phi + c\phi^2 \quad (\text{A-12c})$$

$$F_1(\phi) \approx \sqrt{a + b\phi + c\phi^2 + A_{zp}} \quad (\text{A-12d})$$

$$F_2(\phi) \approx \sqrt{a + b\phi + c\phi^2 + B_{zp}} \quad (\text{A-12e})$$

A.3.1 Region IV: $\tan\phi_p < \phi_{\min}$

$$H = \frac{R}{2\pi} \left[\begin{aligned} & \int_{F_1(\phi_{\max})}^{F_1(\phi_{\min})} e^{-jkr} [-\Psi_7(r)] dr + \int_{F_2(\phi_{\max})}^{F_2(\phi_{\min})} e^{-jkr} [\Psi_8(r)] dr + \\ & \int_{F_1(\phi_{\min})}^{F_2(\phi_{\min})} e^{-jkr} [-\Psi_9(r)] dr + \int_{F_1(\phi_{\max})}^{F_2(\phi_{\max})} e^{-jkr} [\Psi_{10}(r)] dr \end{aligned} \right] \quad (\text{A-13})$$

where

$$\phi_{\min} = -\arcsin(l/R) \quad (\text{A-14a})$$

$$\phi_{\max} = \arcsin(l/R) \quad (\text{A-14b})$$

$$\Psi_7(r) = \frac{1}{\sqrt{-c}} \ln \left(2\sqrt{-cA_{zp}} + \sqrt{b^2 - 4c(a + A_{zp} - r^2)} \right) \quad (\text{A-14c})$$

$$\Psi_8(r) = \frac{1}{\sqrt{-c}} \ln \left(2\sqrt{-cB_{zp}} + \sqrt{b^2 - 4c(a + B_{zp} - r^2)} \right) \quad (\text{A-14d})$$

$$\Psi_9(r) = \frac{1}{\sqrt{-c}} \ln \left(2\sqrt{-c(r^2 - a - b\phi_{\min} - c\phi_{\min}^2)} - 2c\phi_{\min} - b \right) \quad (\text{A-14e})$$

$$\Psi_{10}(r) = \frac{1}{\sqrt{-c}} \ln \left(2\sqrt{-c(r^2 - a - b\phi_{\max} - c\phi_{\max}^2)} - 2c\phi_{\max} - b \right) \quad (\text{A-14f})$$

A.3.2 Region V: $\tan\phi_p \geq \phi_{\min}$

$$\int_{\phi_{\min}}^{\phi_{\max}} \int_{F_1(\phi)}^{F_2(\phi)} dr d\phi = H_1 + H_2 \quad (\text{A-15})$$

$H_1 :$

$$H_1 = \frac{R}{2\pi} \left[\begin{array}{cc} \int_{F_1^*(\phi_{\min})}^{F_1^*(\phi_{\max})} e^{-jkr} [-\Psi_7(r)] dr & + \int_{F_2^*(\phi_{\min})}^{F_2^*(\phi_{\max})} e^{-jkr} [\Psi_8(r)] dr + \\ \int_{F_1^*(\phi_{\min})}^{F_2^*(\phi_{\min})} e^{-jkr} [-\Psi_{11}(r)] dr & + \int_{F_1^*(\phi_{\max})}^{F_2^*(\phi_{\max})} e^{-jkr} [\Psi_{12}(r)] dr \end{array} \right] \quad (\text{A-16})$$

$$F_1^*(\phi^*) = \sqrt{(a - b\phi^* + c(\phi^*)^2 + A_{zp})} \quad (\text{A-17a})$$

$$F_2^*(\phi^*) = \sqrt{(a - b\phi^* + c(\phi^*)^2 + B_{zp})} \quad (\text{A-17b})$$

$$\Psi_{11}(r) = \frac{1}{\sqrt{-c}} \ln \left(2\sqrt{-c(r^2 - a + b\phi_{\min} - c\phi_{\min}^2)} - 2c\phi_{\min} + b \right) \quad (\text{A-17c})$$

$$\Psi_{12}(r) = \frac{1}{\sqrt{-c}} \ln \left(2\sqrt{-c(r^2 - a + b\phi_{\max} - c\phi_{\max}^2)} - 2c\phi_{\max} + b \right) \quad (\text{A-17d})$$

$$\phi_{\min} = -\tan(\phi_p) \quad (\text{A-17e})$$

$$\phi_{\max} = \phi_{\max} \quad (\text{A-17f})$$

H_2 :

$$H_2 = \frac{R}{2\pi} \left[\begin{array}{cc} \int_{F_1(\phi_{max})}^{F_1(\phi_{min})} e^{-jkr} [-\Psi_7(r)] dr & + \int_{F_2(\phi_{max})}^{F_2(\phi_{min})} e^{-jkr} [\Psi_8(r)] dr + \\ \int_{F_1(\phi_{min})}^{F_2(\phi_{min})} e^{-jkr} [-\Psi_9(r)] dr & + \int_{F_1(\phi_{max})}^{F_2(\phi_{max})} e^{-jkr} [\Psi_{10}(r)] dr \end{array} \right] \quad (\text{A-18})$$

where

$$\phi_{min} = -\tan(\phi_p) \quad (\text{A-19a})$$

$$\phi_{max} = \arcsin(l/R) \quad (\text{A-19b})$$

Bibliography

- [1] Z. Cho, J. Jones, and M. Singh, Foundations of Medical Imaging. New York: Wiley-Interscience, 1993.
- [2] T. Taxt, A. Lundervold, J. Strand, and S. Holm, “Advances in medical imaging,” 14th Intl Conference on Pattern Recognition (ICPR98), Brisbane, Australia, August 1998.
- [3] T. Misaridis and J. Jensen, “Use of modulated excitation signals in medical ultrasound. part iii: high frame rate imaging,” IEEE Transactions on Ultrasonics, Ferroelectrics and Frequency Control, vol. 52, pp. 208–219, 2005.
- [4] J. Kirkhorn, S. Bjaerum, B. Olstad, K. Kristoffersen, and H. Torp, “A new technique for improved spatial resolution in high frame rate color doppler imaging,” IEEE Symposium on Ultrasonics, vol. 2, pp. 1947–1950, 2003.
- [5] R. Carotenuto, G. Sabbi, and M. Pappalardo, “Spatial resolution enhancement of ultrasound images using neural networks,” IEEE Transactions on Ultrasonics, Ferroelectrics and Frequency Control, vol. 49, pp. 1039–1049, 2002.

- [6] D. Vray, T. Rastello, F. Schoofs, and P. Delachartre, “Improving the spatial resolution of intravascular ultrasound imaging with synthetic aperture fourier-based methods,” IEEE Symposium on Ultrasonics, vol. 2, pp. 1531–1534, 1997.
- [7] J. I. DiStasio, Ultrasonics as a Medical Diagnostic Tool. Noyes Data Corporation, 1980.
- [8] L. W. Goldman and J. B. Fowlkes, Medical CT and Ultrasound: Current technology and Applications, Proceedings of the 1995 summer school on CT and US technology and Applications of the American Association of Physicists in Medicine. Connecticut Collage New London, Connecticut, 1995.
- [9] Users’ Guide for Analogic AN2300 Ultrasound Engine. Analogic Corporation, Peabody, MA, Sept. 2003.
- [10] P. M. Morse and K. U. Ingard, Theoretical Acoustics. Princeton, N. J: Princeton University Press, 1986.
- [11] M. M. Hutter and D. W. Rattner, “Novel tissue destruction methods,” Problems in General Surgery. Advances in Minimally Invasive Surgery, vol. 18(1), pp. 26–32, 2001.
- [12] G. T. Clement, “Perspectives in clinical uses of high-intensity focused ultrasound,” Ultrasonics, vol. 42, pp. 1087–1093, 2004.
- [13] K. F. Graff, A History of Ultrasonics, in Physical Acoustics. Academic Press, New York, 1982.

- [14] Z. Wang, J. Bai, L. Faqi, and *et al.*, "Study of a "biological focal region" of high-intensity focused ultrasound," Ultrasound in Medicine and Biology, vol. 29, pp. 749–754, 2003.
- [15] G. ter Haar, D. Sinnett, and I. Rivens, "High intensity focused ultrasound-a surgical technique for the treatment of discrete liver tumors," Phys. Med. Biol., vol. 34, pp. 1743–1750, 1989.
- [16] W. Chen, C. Lafon, T. J. Matula, S. Vaezy, and L. A. Crum, "Mechanisms of lesion formation in high intensity focused ultrasound therapy," Acoustic Research Letters Online, vol. 4, pp. 41–46, 2003.
- [17] L. Poissonnier, A. Gelet, J. Chapelon, and *et al.*, "Results of transrectal focused ultrasound for the treatment of localized prostate cancer (120 patients with psa < or + 10ng/ml)," Prog Urol., vol. 13, pp. 60–72, 2003.
- [18] T. A. Gardner, A. Thomas, M. O. Koch, and *et al.*, "Minimally invasive treatment of benign prostatic hyperplasia with high intensity focused ultrasound using the sonablate [trademark] system: An updated report of phase iii clinical studies conducted in the usa," Proceedings of SPIE - The International Society for Optical Engineering, vol. v 4609, pp. 107–114, 2002.
- [19] N. T. Sanghvi, J. Syrus, R. S. Foster, R. Bihrlé, R. Casey, and T. Uchida, "Noninvasive surgery of prostate tissue by high intensity focused ultrasound: An updated report," Proceedings of SPIE, vol. 3907, pp. 194–200, 2000.
- [20] S. Madersbacher, C. Kratzik, and M. Marberger, "Prostatic tissue ablation

- by transrectal high intensity focused ultrasound: histological impact and clinical application,” Ultrasonics Sonochemistry, vol. 4, pp. 175–179, 1997.
- [21] K. Nakamura, S. Baba, S. Saito, M. Tachibana, and M. Murai, “High-intensity focused ultrasound energy for benign prostatic hyperplasia: clinical response at 6 months to treatment using sonablate 200,” J. Endourol., vol. 11, pp. 197–201, 1997.
- [22] E. D. Mulligan, T. H. Lynch, D. Mulvin, D. Greene, J. M. Smith, and J. M. Fitzpatrick, “High-intensity focused ultrasound in the treatment of benign prostatic hyperplasia,” Br. J. Urol., vol. 79, pp. 177–180, 1997.
- [23] C. Chaussy, S. Thuroff, F. Lacoste, and A. Gelet, “Hifu and prostate cancer: The european experience,” In proceedings of the 2nd International Symposium on Therapeutic Ultrasound, 2002.
- [24] J. Kennedy, G. T. Haar, and D. Cranstron, “High intensity focused ultrasound: Surgery of the future?,” The British Journal of Radilology, vol. 76, pp. 590–599, 2003.
- [25] F. Wu, W. Chen, J. Bai, Z. Zou, Z. Wang, H. Zhu, and Z. Wang, “Pathological changes in human malignant carcinoma treated with high-intensity focused ultrasound,” Ultrasound Med. Biol., vol. 27, pp. 1099–1106, 2001.
- [26] F. Wu, Z. Wang, W. Chen, and W. W. *et al.*, “Extracorporeal high intensity focused ultrasound ablation in the treatment of 1038 patients with solid carcinomas in china: An overview,” Ultrasonics Sonochemistry, vol. 11, pp. 149–154, 2004.

- [27] H. Cline, K. Hynynen, C. Hardy, R. Watkins, F. Schenck, and F. Jolesz, “Mr temperature mapping of focused ultrasound surgery,,” Magn. Reson. Med., vol. 31, pp. 628–636, 1994.
- [28] N. McDannold, L. King, F. Jolesz, and K. Hynynen, “Usefulness of mr imaging-derived thermometry and dosimetry in determining the threshold for tissue damage induced by thermal surgery in rabbits,” Radiology, vol. 216, pp. 517–523, 2000.
- [29] K. Hynynen, O. Pomeroy, D. Smith, P. Huber, N. McDannold, and J. K. et al., “Mr imaging-guided focused ultrasound surgery of fibroadenomas in the breast: A feasibility study,” Radiology, vol. 219, pp. 176–185, 2001.
- [30] S. Vaezy, X. Shi, R. Martin, and *et al.*, “Real-time visualization of high-intensity focused ultrasound treatment using ultrasound imaging,” Ultrasound Med. Biol., vol. 27, pp. 33–42, 2001.
- [31] R. Seip, J. Tavakkoli, R. Carlson, and *et al.*, “High-intensity focused ultrasound (hifu) multiple lesion imaging: Comparison of detection algorithms for real-time treatment control,” Proceedings of the IEEE Ultrasonics Symposium, vol. 2, pp. 1427–1430, 2002.
- [32] H. Yao, P. Phukpattaranont, and E. S. Ebbini, “Nonlinear imaging methods for characterization of hifu-induced lesions,” Proc. of SPIE – Thermal Treatment of Tissue: Energy Delivery and Assessment II, vol. 4954, pp. 183–191, 2003.
- [33] H. Yao, P. Phukpattaranont, and E. Ebbini, “Enhanced lesion visualization in image-guided noninvasive surgery with ultrasound phased arrays,”

- Proceedings of the 23rd Annual International Conference of the IEEE Engineering in Medicine and Biology Society, vol. 3, pp. 2492–2495, 2001.
- [34] F. Kallel, R. Stafford, R. Price, R. Righetti, J. Ophir, and J. D. Hazle, “The feasibility of elastographic visualization of hifu-induced thermal lesions in soft tissues. image-guided high-intensity focused ultrasound,” Ultrasound Med. Biol., vol. 25, pp. 641–647, 1999.
- [35] N. R. Miller, J. C. Bamber, and P. M. Meaney, “Fundamental limitations of noninvasive temperature imaging by means of ultrasound echo strain estimation,” Ultrasound Med. Biol., vol. 28, pp. 1319–1333, 2002.
- [36] K. Nightingale, M. S. Soo, and G. Grahey, “Acoustic radiation force impulse imaging: In vivo demonstration of clinical feasibility,” Ultrasound Med. Biol., vol. 28, pp. 227–235, 2002.
- [37] P. E. Barbone and J. C. Bamber, “Quantitative elasticity imaging: What can and what cannot be inferred from strain images,” Phys. Med. Biol., vol. 47, pp. 2147–2164, 2002.
- [38] J. C. Bamber and C. R. Hill, “Ultrasonic attenuation and propagation speed in mammalian tissues as a function of temperature,” Ultrasound Med. Biol., vol. 5, pp. 149–157, 1979.
- [39] N. L. Bush, I. Rivens, G. R. ter Haar, and J. C. Bamber, “Acoustic properties of lesions generated with an ultrasound therapy system,” Ultrasound Med. Biol., vol. 19, pp. 789–801, 1993.
- [40] C. A. Damianou, N. T. Sanghvi, F. J. Fry, , and R. Maass-Moreno, “Dependence of ultrasonic attenuation and absorption in dog soft tissues on

- temperature and thermal dose,” J. Acoust. Soc. Am., vol. 102, pp. 628–634, 1997.
- [41] S. H. Bloch, M. R. Bailey, L. Crum, P. Kaczkowski, G. Keilman, and P. Mourad, “Measurements of sound speed in excised tissue over temperature expected under high-intensity focused ultrasound conditions,” Proceedings of the joint meeting of the 16th ICA and the 135th Meeting of the ASA, vol. 2, pp. 1065–1066, 1998.
- [42] A. E. Worthington and M. D. Sherar, “Changes in ultrasound properties of porcine kidney tissue during heating,” Ultrasound Med. Biol., vol. 27, pp. 673–682, 2001.
- [43] U. Techavipoo, T. Varghese, Q. Chen, T. A. Stiles, J. A. Zagzebski, and G. R. Frank, “Temperature dependence of ultrasonic propagation speed and attenuation in excised canine liver tissue measured using transmitted and reflected pulses,” J. Acoust. Soc. Am., vol. 116, pp. 2859–2865, 2004.
- [44] P. D. Tyr  us and C. Diederich, “Two-dimensional acoustic attenuation mapping of high-temperature interstitial ultrasound lesions,” Phys. Med. Biol., vol. 49, pp. 533–546, 2004.
- [45] M. Pernot, M. Tanter, J. Bercoff, K. Waters, and M. Fink, “Temperature estimation using ultrasonic spatial compound imaging,” IEEE UFFC, vol. 51, pp. 606–615, 2004.
- [46] L. A. S. Baker and J. C. Bamber, “Effect of dynamic receive focusing on reflex transmission imaging (rti),” Proc. IEEE Ultrason. Symp., 2002.

- [47] A. Anand and P. J. Kaczkowski, “Monitoring formation of high intensity focused ultrasound (hifu) induced lesions using backscattered ultrasound,” Acoust. Res. Lett. Onlin, vol. 5, pp. 88–94, 2004.
- [48] C. R. Vogel, “Computational methods for inverse problems,” Society of Industrial and Applied Mathematics, 2002.
- [49] F. Natterer and F. Wubbeling, “Mathematical methods in image reconstruction,” SIAM, 2001.
- [50] F. Aubry, M. Tanter, J. L. Thomas, and M. Fink, “Comparison between time reversal and inverse filter focusing,” Acoustical Imaging, vol. 25, pp. 01–108, 2000.
- [51] G. Montaldo, M. Tanter, and M. Fink, “Real time inverse filter focusing through iterative time reversal,” J. Acoust. Soc. Am., vol. 115, 2004.
- [52] S. D. L. O. S. Haddadin and E. S. Ebbini, “Solution to the inverse scattering problem using a modified distorted born iterative algorithm,” Proc. IEEE Ultrason. Symp., 1995.
- [53] O. S. Haddadin and E. Ebbini, “Imaging strongly scattering media using a multiple frequency distorted born iterative method,” IEEE UFFC, vol. 45, pp. 1485–1496, 1998.
- [54] G. Boverman, M. K. Miled, and E. L. Miller, “Recent work in shape-based methods for diffusive inverse problems,” Review of Scientific Instruments, vol. 74, p. 2003, 2580-2582.

- [55] E. L. Miller, M. Cheney, M. K. Kilmer, G. Boverman, L. Ang, and D. Boas, “Feature-enhancing methods for limited view tomographic imaging problems,” Subsurface Sensing Technologies and Applications, vol. 4, pp. 327–353, 2003.
- [56] M. Kilmer, E. L. Miller, A. Barbaro, and D. A. Boas, “3d shape-based imaging for diffuse optical tomography,” Applied Optics Special Issue on Topics in Biomedical Optics, vol. 42, pp. 3129–3144, 2003.
- [57] P. C. Pedersen and L. Wan, “Optimization of pulse-echo array transducer system for identification of specified targets,” Acoustical Imaging, vol. 26, pp. 373–380, 2002.
- [58] P. Pedersen and A. Nadkarni, “Optimization of an array based pulse-echo system for identification of reflector geometry,” IEEE Symposium on Ultrasonics, vol. 2, pp. 1050–1053, Aug 2004.
- [59] P. Wu and T. Stepinski, “Spatial impulse response method for predicting pulse-echo fields from a linear array with cylindrically concave surface,” IEEE Transactions on Ultrasonics, Ferroelectrics, and Frequency Control, vol. 46, pp. 1283–1299, 1999.
- [60] M. Arditi, F. Foster, and J. Hunt, “Transient fields of concave annular arrays,” Ultrasonic Imaging, vol. 3, pp. 37–61, 1981.
- [61] P. Stepanishen, “The time-dependent force and radiation impedance on a piston in a rigid infinite planar baffle,” J.Acoust.Soc.Am., vol. 49, pp. 841–849, 1971A.

- [62] P. R. Stepanishen, "Transient radiation from pistons in a infinite planar baffle," J.Acoust.Soc.Am, vol. 49, pp. 1627–1638, 1971B.
- [63] B. Piwakowski and K. Sbai, "A new approach to calculate the field radiated from arbitrarily structured transducer arrays," IEEE Transactions on Ultrasonics, Ferroelectrics and Frequency Control, vol. 46, pp. 422–440, March 1999.
- [64] J. F.Theumann, M.Arditi, J. J.Meister, and E.Jaques, "Acoustic fields of concave cylindrical transducers," J. Acoust. Soc. Amer., vol. 88, pp. 1160–1169, 1990.
- [65] T. L. Szabo, B. U. Karbeyaz, R. O. Cleveland, and E. L. Miller, "Determining the pulse-echo electromechanical characteristic of a transducer using flat plates and point targets," J. Acoust. Soc. Am., vol. 116, pp. 90–96, 2004.
- [66] J. A. Jensen, "A model for the propagation and scattering of ultrasound in tissue," J. Acoust. Soc. Am., vol. 89, pp. 182–190, 1991.
- [67] L. A. Chernov, Wave Propagation In Random Medium. Mcgraw-Hill, 1960.
- [68] W. Chew, Waves and Fields in Inhomogenous Media. IEEE Press.
- [69] M. Slaney and A. C. Kak, Principles of Computerized Imaging. IEEE Press, 1988.
- [70] R. N. Carpenter and P. Stepanishen, "An improvement in the range resolution of ultrasonic pulse echo systems by deconvolution," J. Acoust. Soc. Am, vol. 75, pp. 1084–1091, 1984.

- [71] X. Chen, D. Phillips, K. Schwarz, J. Mottley, and K. Parker, "The measurement of backscatter coefficient from a broadband pulse-echo system: a new formulation," IEEE Trans. Ultrason. Ferroelectr. Freq. Control, vol. 44, pp. 515–525, 1997.
- [72] J. C. Machado and F. S. Foster, "Experimental validation of a diffraction correction model for high frequency measurement of ultrasound backscatter coefficients," IEEE Ultrasonics Symp. Proc., pp. 1869–1872, 1998.
- [73] J. M. Thijssen, "Spectroscopy and image texture analysis," Ultrasound in Medicine and Biology, vol. 26, pp. S41–S44, 2000.
- [74] J. W. Hunt, M. Ardit, and F. Foster, "Ultrasound transducers for pulse-echo medical imaging," IEEE Trans Biomedical Engr, vol. BME-30, pp. 453–481, 1983.
- [75] H. Seki, A. Granato, and R. Truell, "Diffraction effects in the ultrasonic field of a piston source and their importance in the accurate measurement of attenuation," J.Acoust. Soc. Am., vol. 28, pp. 230–238, 1956.
- [76] P. H. Rogers and A. L. Buren, "An exact expression for the lommel diffraction correction integral," J.Acoust. Soc. Am, vol. 55, pp. 724–728, 1974.
- [77] X. Chen, K. Schwarz, and K. J.Parker, "Acoustic coupling from a focused transducer to a flat plate and back to the transducer," J. Acoust. Soc. Am., vol. 95, pp. 3049–3054, 1994.
- [78] M. Abramowitz and I. A. Stegun, Handbook of Mathematical Functions with Formulas, Graphs, and Mathematical Tables. New York: Dover, 9 ed., 1964.

- [79] J. A. Jensen and P. Munk, eds., Computer phantoms for simulating ultrasound B-mode and cfm images, (Boston, Massachusetts, USA), 23rd Acoustical Imaging Symposium, 13-16 April 1997.
- [80] J. W. S. Rayleigh, "Investigation of the disturbance produced by a spherical obstacle on the waves of sound," Proc. London Math. Soc., vol. 4, pp. 253–283, 1872.
- [81] A. D. Pierce, Acoustics. Woodbury, NY: Acoustical Society of America, 1989.
- [82] D. K. Nassiri and C. R. Hill, "The use of angular acoustic scattering measurements to estimate structural parameters of human and animal tissues," J. Acoust. Soc. Am, vol. 79, p. 2048:2054, 1986.
- [83] E. Madsen, M. Insana, and J. A. Zagzebski, "Method of data reduction for accurate determination of acoustic backscatter coefficients," J. Acoust. Soc. Am, vol. 76, pp. 913–923, 1984.
- [84] S. L. Bridal, K. D. Wallace, R.L.Trousil, S. Wickline, and J. Miller, "Frequency dependence of acoustic backscatter from 5 to 65 mhz ($0.06 < ka < 4.0$) of polystyrene beads in agarose," J. Acoust. Soc. Am, vol. 100, pp. 1841–1848, 1996.
- [85] R. A. Sigelmann. and J. Reid, "Analysis and measurement of ultrasonic backscattering from an ensemble of scatterers excited by sine-wave bursts," J. Acoust. Soc. Am., vol. 53, pp. 1351–1355, 1973.
- [86] J. M. Reid, "Self-reciprocity calibration of echo-ranging transducers," J. Acoust. Soc. Am., vol. 55, pp. 862–868, 1974.

- [87] E. L. Madsen, M. M. Goodsit, and J. A. Zagzebski, "Continuous waves generated by focused transducers," J. Acoust. Soc. Am., vol. 70, pp. 1508–1517, Nov. 1981.
- [88] G. Tupholme, "Generation of acoustic pulses by baffled plane pistons," Mathematika, vol. 16, pp. 209–224, 1969.
- [89] I. Gradshteyn and I. Ryzhik, Table of Integrals, Series, and Products. Academic Press, 2000.
- [90] N. S. Bakhvalov and L. G. Vasil'eva, "Evaluation of the integrals of oscillating functions by interpolation at nodes of gaussian quadratures," U.S.S.R. Comput. Math. and Math. Phys., vol. 8, pp. 241–249, 1968.
- [91] C. A. Balanis, Advanced Engineering Electromagnetics. John Wiley & Sons, 1989.
- [92] J. B. Kuipers, Quaternions and rotation sequences : a primer with applications to orbits, aerospace, and virtual reality. Princeton, N.J. : Princeton University Press, 1999.
- [93] M. H. W. Philip E. Gill, Walter Murray, Practical optimization. New York : Academic Press, 1981.
- [94] B. U. Karbeyaz, E. L. Miller, R. O. Cleveland, and R. A. Roy, "Adaptive linearized modeling and inversion for 3d tissue characterization," J. Acoust. Soc. Am., vol. 114, p. 2379, 2003.

- [95] C. Lafon, P. J. Kaczkowski, S. Vaezy, M. Noble, and O. A. Sapozhnikov, “Development and characterization of an innovative synthetic tissue-mimicking material for high intensity focused ultrasound (hifu) exposures,” IEEE Ultrasonics Symposium Proceedings, pp. 1295–1298, 2001.
- [96] A. C. Kak and M. Slaney, Principles of Computerized Tomographic Imaging. IEEE Press, 1988.
- [97] J. Dey, Modeling and Analysis of Ultrasound Propagation in Layered Medium. PhD thesis, Robotics Institute, Carnegie Mellon University, Pittsburgh, PA, August 1999.